Modeling and Control of the Fuel Supply System in a Polymer Electrolyte Membrane Fuel Cell

by

Alireza Ebadi Ghajari

M.Sc., Chalmers University, Sweden 2011
B.Sc., University of Tehran, Iran, 2007

Thesis Submitted in Partial Fulfillment of the
Requirements for the Degree of
Doctor of Philosophy

in the
Department of Mechatronics Systems Engineering
Faculty of Applied Sciences

SIMON FRASER UNIVERSITY
Summer 2017

Approval

Name:	**Alireza Ebadi Ghajari**
Degree:	**Doctor of Philosophy (Systems and Control)**
Title:	***Modeling and Control of the Fuel Supply System in a Polymer Electrolyte Membrane Fuel Cell***
Examining Committee:	**Chair:** Jiacheng Wang Assistant Professor

Farid Golnaraghi
Senior Supervisor
Director/Professor _____

Jake DeVaal
Supervisor
Product Safety Manager
Ballard Power Systems _____

Mehrdad Moallem
Supervisor
Professor _____

Gary Wang
Internal Examiner
Professor _____

Nedjib Djilali
External Examiner
Professor
Mechanical Engineering
University of Victoria _____

Date Defended: May 30, 2017

Abstract

Prolonging membrane longevity as well as improving fuel economy are essential steps toward utilization of fuel cells in industrial applications. Focusing on polymer electrolyte membrane (PEM) fuel cells, the present work elucidates a systematic approach to deal with cell durability issues, inflicted by membrane pinholes. This includes the model-based control of fuel overpressure, which is defined as the pressure difference between the anode and cathode compartments, at the inlet side of the fuel cell stack. Moreover, to enhance fuel savings, this work proposes a novel model-based technique for estimation of hydrogen concentration, which is used as the basis of fuel purging control. Employing a Ballard 3kW test station equipped with a 9-cell Mk1100 PEM fuel cell, the entire system is modeled using pneumatic variables. The developed model is experimentally validated. Depending on the underlying objective, a relevant system configuration for the PEM fuel cell anode is adopted. These include a flow-through anode, dead-ended anode, and anode with recirculation structures.

A model predictive controller (MPC) is deployed to achieve the controller objectives, which include the improvement in control of the system transient response during the load change, reduction of hydrogen emission, and retaining the cell voltage level of a defective cell, by maintaining the fuel overpressure in the desired region. Furthermore, the controller performance is verified experimentally.

Using the pressure drop across the fuel cell stack anode, the hydrogen concentration on the anode side is estimated in a hydrogen-nitrogen gas mixture. This pressure drop is correlated to the dynamic viscosity of a gas mixture. The estimation model which is verified experimentally for various scenarios provides a reliable and cost-effective method that can eliminate the use of the hydrogen sensor. This model is then utilized as the basis for controlling the fuel purging. Deploying an MPC based multivariable control strategy, both fuel overpressure and hydrogen concentration are controlled.

Keywords: Fuel cells; Fuel overpressure; Fuel purge control; Hydrogen concentration; Model predictive control; Hydrogen transfer leak

Dedication

Dear Mom & Dad,

This achievement could have never been accomplished without your faith, devotion, and unconditional support.

I love you,

Masoumeh & Mahmood

May 2017

Acknowledgements

We would like to thank Ballard Power Systems for assisting us with the hardware as well as testing and their valuable technical support. The support of NSERC project CRDPJ 467686-14 for improving the control, safety, and diagnostics of heavy duty fuel cells is also gratefully acknowledged. Also, we would like to thank the SFU School of Mechatronic Systems Engineering and MITACS Project IT08640 for supporting this work.

Finally, I would like to send my sincere gratitude to Professor Farid Golnaraghi, my senior supervisor at Simon Fraser University, and Dr. Jake DeVaal, my supervisor at Ballard Power Systems, for their full support during my Ph.D. studies. Also, I would like to thank our co-op students, Mavin Bautista, and Niloufar Moallem who helped us with testing during this project.

Table of Contents

Approval ii

Abstract iii

Dedication iv

Acknowledgements v

Table of Contents vi

List of Tables ix

List of Figures x

Nomenclature xiii

1 Introduction 1

1.1 Background . . . 1

1.1.1 Fundamentals of PEM fuel cells operation . . . 3

1.2 Fuel cell system modeling . . . 4

1.2.1 Control-oriented modeling of the fuel supply system . . . 5

1.2.2 Hydrogen transfer leak modeling . . . 6

1.3 Fuel cell system control . . . 7

1.3.1 Fuel overpressure control . . . 7

1.3.2 Hydrogen concentration control . . . 8

1.4 Thesis objectives . . . 9

1.5 Summary . . . 10

2 Modeling of Fuel Supply System 11

2.1 PEM fuel cell system configurations . . . 11

2.1.1 Flow-through anode . . . 11

2.1.2 Dead-ended anode . . . 14

2.1.3 Anode with recirculation . . . 14

2.2 Pneumatic modeling . . . 16

2.2.1 System model . . . 17
2.2.2 Actuator model . . . 23
2.3 Hydrogen transfer leak model . . . 25
2.4 Results . . . 26
2.4.1 System model parameters . . . 26
2.4.2 Actuator characterization . . . 27
2.4.3 Hydrogen transfer leak characterization . . . 30
2.5 Summary . . . 31

3 Fuel overpressure control **32**
3.1 Control architecture . . . 32
3.2 Control design . . . 33
3.2.1 Performance requirements and problem constraints . . . 33
3.2.2 Control problem formulation . . . 34
3.2.3 Stability and robustness . . . 36
3.2.4 Control limitations . . . 37
3.3 Results of controller performance . . . 38
3.3.1 Flow-through anode . . . 38
3.3.2 Dead-ended anode with periodic purging . . . 40
3.3.3 Anode with recirculation with load-based purging . . . 43
3.4 Reduction of hydrogen emission . . . 43
3.5 Impact on the cell voltage . . . 43
3.6 Summary . . . 45

4 Hydrogen concentration control **46**
4.1 Model-based estimation of hydrogen concentration . . . 46
4.1.1 Use of the pneumatic model . . . 47
4.1.2 Dynamic viscosity . . . 48
4.1.3 Model-based HC estimation method . . . 49
4.1.4 Results . . . 51
4.2 Multivariable control design . . . 56
4.3 Results . . . 58
4.4 Summary . . . 61

5 Conclusions **62**
5.1 Improved system performance by enhanced fuel overpressure control . . . 62
5.2 Model-based estimation of hydrogen concentration . . . 62
5.3 Hydrogen concentration control to improve fuel economy . . . 63
5.4 Future works . . . 63

List of Publications **64**

Bibliography **65**

Appendix A Reduction of Hydrogen Transfer by Constrained Control of Anode Hydrogen Recirculation in a Polymer Electrolyte Membrane Fuel Cell **70**

A.1 Modeling of the PEMFC with anode recirculation 71

A.1.1 State-Space Model 72

A.1.2 Actuator modeling 74

A.1.3 Hydrogen transfer leak characterization 75

A.2 Controller design 77

A.2.1 Control problem formulation 77

A.3 Simulation results 78

A.4 Conclusions 80

List of Tables

Table 2.1 The rotational speed of the HRB pump for selected control voltages . 15
Table 2.2 The hydrogen sensor voltage for various hydrogen concentrations . . . 16
Table 2.3 Model parameters on the anode side [33] (used with the permission of Elsevier) 27
Table 2.4 The valve characterization (P_{out} is relative to $P_{atm} \approx 1$bar) [33] (used with the permission of Elsevier) 28
Table 2.5 Leak size classification for cross-pressure $\in [1, 7]$ psi [33] 30

Table 4.1 The reference values of C, T_0, and μ_0 for selected gasses 49

List of Figures

Figure 1.1 General schematic of a fuel cell system [4] (used with the permission of IEEE) . . . 1
Figure 1.2 (a) The projected fuel cell transportation system costs per kW for high volume production (500,000 units per year), (b) a comparison of fuel cell transportation cost between 2007 and 2011 for a wide range of manufacturing volumes [6] . . . 2
Figure 1.3 Basic elements of a PEM fuel cell . . . 3
Figure 1.4 Different anode configurations [44] (used with the permission of Elsevier) . . . 9

Figure 2.1 The schematic of the Ballard 3kW test station with the flow-through anode [33] (used with the permission of Elsevier) . . . 12
Figure 2.2 (a) Humidifier, (b) Condenser . . . 13
Figure 2.3 A proportional solenoid valve . . . 13
Figure 2.4 The schematic of the Ballard 3kW test station with the dead-ended anode [40] (used with the permission of IEEE) . . . 14
Figure 2.5 The Ballard 3kW test station with hydrogen recirculation blower . 15
Figure 2.6 P&ID of the Ballard 3kW test station with anode recirculation . . . 16
Figure 2.7 The pneumatic model of the flow-through anode . . . 17
Figure 2.8 The pneumatic model of the dead-ended anode [40] (used with the permission of IEEE) . . . 20
Figure 2.9 The pneumatic model of the anode with recirculation [34] (used with the permission of IEEE) . . . 22
Figure 2.10 The inclusion of hydrogen transfer leaks in the pneumatic model [33] (used with the permission of Elsevier) . . . 25
Figure 2.11 (a) The input hydrogen flow rate intended for parameter identification, (b) Verification of the simulation model with the experimental data [33] (used with the permission of Elsevier) . . . 27
Figure 2.12 The 3D model of the valve characteristic function [33] (used with the permission of Elsevier) . . . 29
Figure 2.13 The HRB characterization for various anode stack inlet pressures . 29

Figure 2.14 Characterization of hydrogen transfer leaks for three different sizes of pinholes: Large(L), Medium(M), and Small(S) leak sizes [33] (used with the permission of Elsevier) 30

Figure 3.1 The control architecture for FOP control with an MPC controller (used with the permission of Elsevier) 32
Figure 3.2 Load current variations for (a) large, (b) medium, and (c) small leaky stacks [33] (used with the permission of Elsevier) 39
Figure 3.3 Tracking performance of the controller for: (a) large (L), (b) medium (M), and (c) small (S) leaky stacks. The control input (u_c) and the model input (u) represented in absolute pressure values for: (d) large (L), (e) medium (M), and (f) small (S) leaky stacks [33] (used with the permission of Elsevier) 39
Figure 3.4 A simulation scenario indicating the load variation and periodic purging [40] (used with the permission of IEEE) 41
Figure 3.5 The tracking performance of the controller: (a) Pressure responses on the anode and cathode sides, (b) The tracking error and the constraints [40] (used with the permission of IEEE) 42
Figure 3.6 The control input command [40] (used with the permission of IEEE) 42
Figure 3.7 The hydrogen emission as a function of fuel overpressure and load current in a large leaky stack (cell leak $\geq$ 50 sccm for cross-pressure $\geq$ 1 psi) [33] (used with the permission of Elsevier) 44
Figure 3.8 The cell voltage as a function of fuel overpressure for small, medium, and large leaky cells for I = 20A [33] (used with the permission of Elsevier) 45

Figure 4.1 A simplified pneumatic model of the PEMFC anode using the equivalent electrical circuit 47
Figure 4.2 Flowchart of the estimation algorithm for deriving the H_2 concentration 51
Figure 4.3 Parameter k for various H_2 concentrations at T = 65 C, P_{in} = 10 psi, and I = 125 A 52
Figure 4.4 Verification results at V_{hrb} = 2.5 V, I = 160 A, and P_{in} = 12 psi at T = 65 C: (a) H_2 sensor output and the measured pressure drop ΔP_m, (b) HC estimation HC_{est} versus HC measurement (HC_m) . 53

Figure 4.5 Effect of the operating conditions on estimation model performance at T = 65 C: (a) Comparison of ΔP_m for I = 110 and 160 A, P_{in} = 12, and V_{hrb} = 2.5 V (b) The verification of the estimation model for I = 110 and 160 A, P_{in} = 12, and V_{hrb} = 2.5 V, (c) The comparison of ΔP_m for P_{in} = 8 and 12 psi, I = 160 A, and V_{hrb} = 2.5 V, (d) The verification of the estimation model for for P_{in} = 8 and 12 psi, I = 160 A, and V_{hrb} = 2.5 V 55
Figure 4.6 The HRB characterization at V_{hrb} = 2.5 V and I = 110 and 160 A as well as V_{hrb} = 3.5 V and I = 125 A 56
Figure 4.7 The simulation scenario: (Top) Load current, (Bottom) Nitrogen crossover flow rate [34] 59
Figure 4.8 Controller tracking performance: (Top) Fuel overpressure, (Bottom) Variation in anode outlet pressure for 100% H_2 [34] 60
Figure 4.9 Controller input command: (Top) Pressure control valve resistor variation, (Bottom) Purge valve resistor variation [34] 60

Nomenclature

Δg_f	Gibbs free energy
ΔP	pressure drop
$\dot{m}_{cons}$	consumption flow rate
$\dot{m}_{leak}$	hydrogen transfer leak flow rate
$\dot{m}_{N_2}$	nitrogen crossover flow rate
$\dot{m}_o$	anode output flow rate
$\dot{m}_{wi}$	input water flow rate
$\dot{m}_{wo}$	output water flow rate
μ	dynamic viscosity
μ_m	dynamic viscosity of gas mixture
C_c	condenser pneumatic capacitor
C_{fc}	stack pneumatic capacitor
C_h	humidifier pneumatic capacitor
C_{in}	inlet manifold pneumatic capacitor
F	Faraday's constant
H_2	hydrogen
HC	hydrogen concentration
I	load current in [A]
I	load current
k	fuel cell constant
L	length of the pipe
l	leak size
N	number of cells
N_2	nitrogen

P_1	FC stack anode's inlet pressure
P_2	FC stack anode's outlet pressure
P_h	humidifier inlet pressure
P_h	hydrogen pressure
P_n	hydrogen pressure
P_{a1}	anode input pressure
P_{a2}	FC stack anode's inlet pressure
P_{a3}	FC stack anode's outlet pressure
P_{a4}	anode outlet pressure
P_{in}	FC stack anode's inlet pressure
P_{out}	anode outlet pressure
P_{sat}	saturation pressure
Q_h	hydrogen flow rate
Q_n	nitrogen flow rate
Q_r	recirculation flow rate
Q_{cons}	consumption flow rate
Q_c	consumption flow rate
Q_{in}	anode input flow rate
Q_{leak}	hydrogen transfer leak flow rate
Q_{N_2}	nitrogen flow rate
Q_o	anode output flow rate
Q_v	flow rate through the valve
Q_w	water flow rate
R	universal gas constant
r	radius of the pipe
R_c	condenser pneumatic resistor
R_h	humidifier pneumatic resistor
R_L	laminar resistor
R_p	purge valve pneumatic resistor
R_v	valve pneumatic resistor
R_{fc}	FC stack pneumatic resistor

R_{in} inlet manifold pneumatic resistor

Re Raynold's number

s leak size

T Temperature

T_h hydrogen temperature

T_n nitrogen temperature

V_h hydrogen volume

V_n nitrogen volume

V_{hrb} HRB control voltage

V_i valve input voltage

x mole fraction of a component in mixture

x_h hydrogen molar fraction, hydrogen concentration

x_n nitrogen molar fraction, nitrogen concentration

ΔP_m pressure drop across the FC stack anode

ΔP_{hrb} pressure drop across the HRB

ΔP_v pressure drop across the valve

HC_m measured hydrogen concentration

HC_{est} estimated hydrogen concentration

List of Abbreviations

AWR anode with recirculation

P&ID piping and Instrumentation Diagram

MFC mass flow controller

HRB hydrogen recirculation blower

HTL hydrogen transfer leak

OCV open circuit voltage

RH relative humidity

ICE internal combustion engine

DOE department of energy

FSS fuel supply system

PEM polymer electrolyte membrane

HC hydrogen concentration

MPC model predictive control

FC fuel cell

FOP fuel overpressure

BPV back pressure valve

MFM mass flow meter

GE general electric

NASA national aero space agency

MEA membrane electrode assembly

Chapter 1

Introduction

1.1 Background

Reducing environmental pollution along with the scarcity of fossil fuels, have escalated the necessity of finding alternative green energy sources where fuel cells (FC) are viable choices [1]. FCs provide a cleaner and more efficient form of power delivery compared to internal combustion engines (ICE) [2]. Approximately, 70% of today's electrical power consumption is generated from fossil combustibles [3]. Currently fuel cells are employed in a variety of applications including stationary backup power, distributed power generation, portable electronic equipment, and in the transportation industry [1,2]. In particular, during the 2010 Winter Olympic Games in Vancouver, Canada, Whistler buses were equipped with fuel cells. In recent years, various ongoing projects are looking for more fruitful and productive avenues for fuel cell usage, especially in automotive practices.

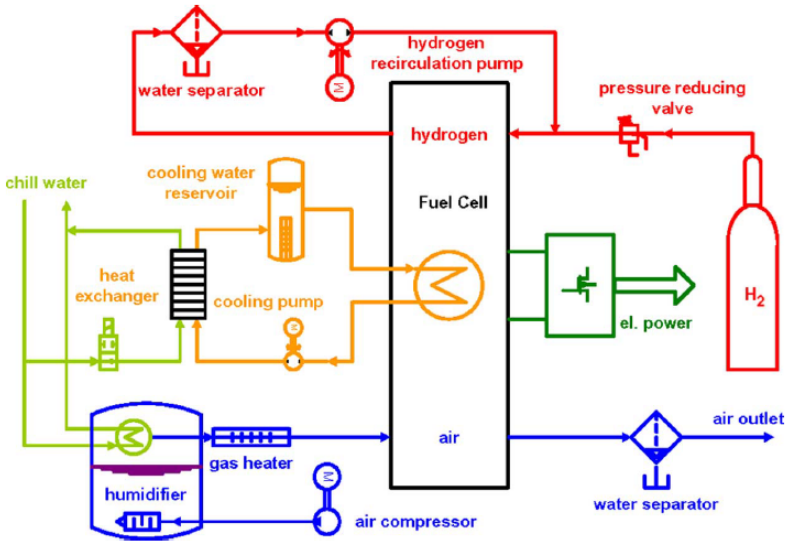

Figure 1.1: General schematic of a fuel cell system [4] (used with the permission of IEEE)

Among different types of fuel cell systems, Polymer Electrolyte Membrane (PEM) fuel cells operate at low temperatures, possess a compact design, and lack any corrosive fluid hazard [2]. Therefore, PEM fuel cells are a promising choice for automotive applications [5]. In addition to the stack, fuel cells are composed of several peripheral components such as the humidifier, reformer, or heat exchanger. Figure 1.1 depicts a general schematic of an FC system aimed for use in automotive applications [4].

Improving the efficiency, reliability, and durability of fuel cell systems are the primary focuses of researches in this area. Materials, auxiliary components, and system maintenance ultimately should be more cost efficient [6]. According to The U.S. Department of Energy (DOE) in 2011, the platinum content of a fuel cell reached to less than 0.2 g/kW with the DOE's target value of 0.125 g/kW. This has resulted in a 5-time reduction in platinum usage which has largely improved fuel cell durability. In addition, since 2008 the projected volume cost per kW, for fuel cells in light duty vehicles has declined by 30%. In Figure 1.2, the projected fuel cell transportation system cost per kW for a high volume production (500,000 units per year) is shown where the target value in 2017 is \$30/kW. Moreover, in Figure 1.2 for a broad range of manufacturing volumes, the cost of the fuel cell transportation system in 2011 is compared to that of 2007.

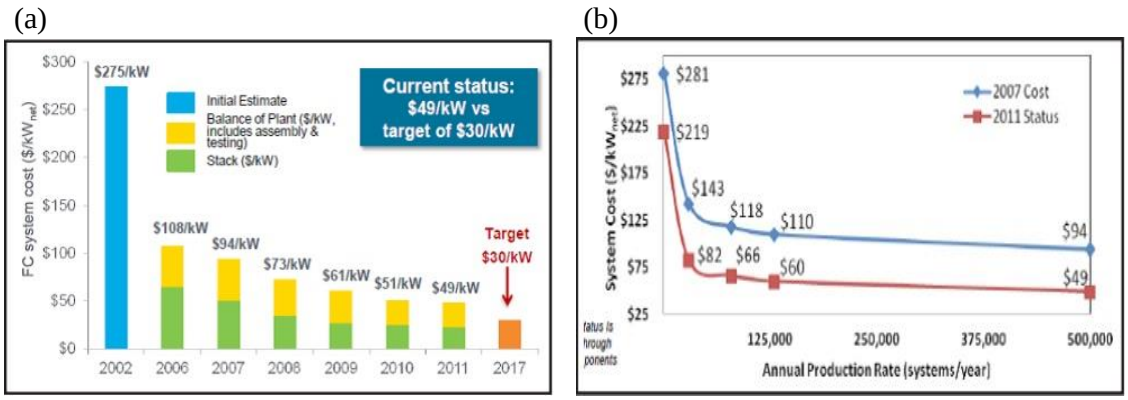

Figure 1.2: (a) The projected fuel cell transportation system costs per kW for high volume production (500,000 units per year), (b) a comparison of fuel cell transportation cost between 2007 and 2011 for a wide range of manufacturing volumes [6]

Fuel cell research is the grounds for interaction of various engineering disciplines such as electro-chemistry, materials, or fluid mechanics. Moreover, FCs manufacturing and employment involve other areas such as sensing, vibration, and control [7]. Since the first commercial use of FC by General Electric (GE) and US National Aero Space Agency (NASA) for the Gemini space project [8], researches on fuel cell technology and development have been boosted significantly.

1.1.1 Fundamentals of PEM fuel cells operation

In essence, fuel cells convert the electrochemical energy into the electrical energy through the reaction between hydrogen oxidization on the anode side and oxygen reduction on the cathode side, while water and heat are also generated as by-products. Figure 1.3 depicts the primary elements of a PEM fuel cell, including the Membrane Electrode Assembly (MEA) and gas flow channels. MEA is composed of the membrane, the anode, and the cathode.

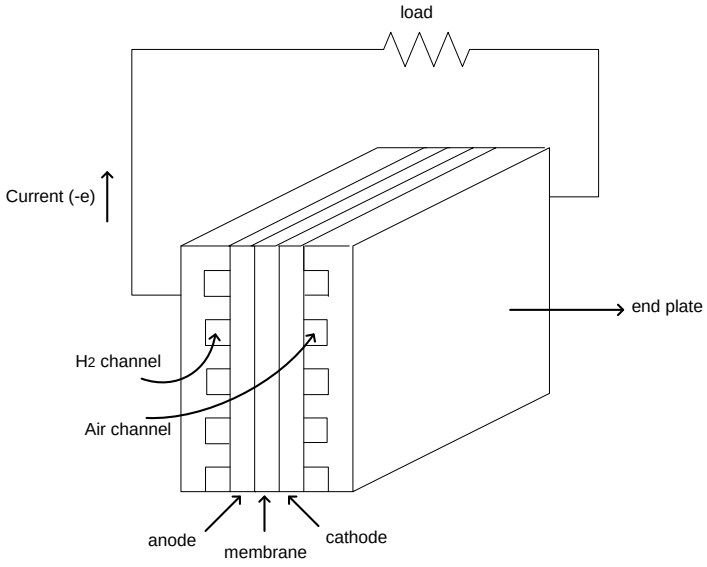

Figure 1.3: Basic elements of a PEM fuel cell

The hydrogen oxidization and the oxygen reduction reactions are expressed as follows:

$$2H_2 \rightarrow 4H^+ + 4e^- \tag{1.1}$$

$$O_2 + 4e^- + 4H^+ \rightarrow 2H_2O \tag{1.2}$$

The overall reaction is then formulated in the following:

$$H_2 + \frac{1}{2}O_2 \rightarrow H_2O \tag{1.3}$$

The released energy during an electrochemical reaction is calculated via the change in Gibbs free energy (Δg_f), which is equivalent to the difference between Gibbs free energy of products and of reactants [3]:

$$\Delta g_f = (g_f)_{products} - (g_f)_{reactants} \tag{1.4}$$

$$\Delta g_f = (g_f)_{H_2O} - (g_f)_{H_2} - \frac{1}{2}(g_f)_{O_2} \tag{1.5}$$

Gibbs free energy represents the available energy for the external circuit. Furthermore, Δg_f is dependent on the pressure and concentration of reactants as described in equation (1.6):

$$\Delta g_f = \Delta g_f^o - RT \ln(\frac{P_{H_2} P_{O_2}^{0.5}}{P_{H_2O}}) \tag{1.6}$$

where R is the universal gas constant, T is the stack temperature, P_{H_2} is the partial pressure of hydrogen, P_{O_2} is the partial pressure of oxygen, P_{H_2O} is the partial pressure of water, and Δg_f^o is the change in Gibbs free energy at the standard pressure (1 bar).

In an ideal reversible reaction, where all the Gibbs free energy is consumed for the external circuit with no losses, the electric work expresses the work for circulating two electrons for each mole of hydrogen as follows:

$$E = \frac{-\Delta g_f}{2F} \tag{1.7}$$

Therefore, the reversible voltage in a PEM fuel cell can be derived using (1.6) and (1.7), as follows:

$$E = E^o + \frac{RT}{2F} \ln(\frac{P_{H_2} P_{O_2}^{0.5}}{P_{H_2O}}) \tag{1.8}$$

where E_o is the electromotive force at the standard pressure. Values of Δg_f and E_o at different temperatures are provided in [2].

The actual operation of a PEM fuel cell is subjected to various losses including the activation, ohmic, and mass transport losses. Therefore, the operating voltage of a PEM fuel cell is expressed as follows:

$$V = \tilde{E} - \Delta V_{act} - \Delta V_{ohm} - \Delta V_{tran} \tag{1.9}$$

where $\tilde{E}$ is the open circuit voltage (OCV), ΔV_{act} is the activation loss, ΔV_{ohm} is the Ohmic loss, and ΔV_{tran} is the mass transport loss. $\tilde{E}$ is usually less than the theoretical value for the OCV (E) which was provided in equation (1.7) [2]. The voltage drawn from equation (1.9) is known as the polarization curve. Detailed discussion on these losses are outside of the scope of this work which can be found in [2].

In the following sections in this chapter, previous studies in the area of PEM fuel cell modeling and control as well as state of the art in fuel cell technology are presented.

1.2 Fuel cell system modeling

Fuel cell system modeling is a broad area, aiming at capturing the fuel cell system operation through physical or mathematical models, which establishes a basis for explaining different

phenomena occurring in the system. Numerous fuel cell models are focused on specific properties of the FC stack.

Employing both mechanistic and empirical modeling, a PEM fuel cell performance is described via a parametric model in [9, 10]. A more comprehensive steady-state electrochemical model of a PEMFC is provided in [11] which accounts for different active areas and membrane thicknesses even at high current densities. A dynamic model of PEM fuel cell system is provided in [12] which combines empirical modeling with mass and energy conservation equations. These models are expressing the steady-state behavior of the PEMFC. Also, such models are normally validated via the polarization curve of the PEMFC.

Control-oriented modeling is suitable for control applications where both transient and steady-state responses of the system are critical. The following section covers some of the existing control oriented models which have been used extensively in literature.

1.2.1 Control-oriented modeling of the fuel supply system

Employing pneumatic variables, such as a pneumatic resistor or a pneumatic capacitor, the dynamic model of the entire fuel cell system is developed in [13] for the air side. In analogy to the air side, the dynamic model of the fuel supply system (FSS) can be derived. A pneumatic resistor reflects friction forces in the gas flow channels while a pneumatic capacitor represents the storage capacity of the components. The model is also validated for a 25 cell PEM stack. This model is suitable for control design since it captures the transient as well as the steady-state behavior of the system, and is used in [14,15] for control purposes. In Chapter 2, we will adopt the pneumatic modeling technique for modeling the Ballard 3kW PEMFC test station.

Pukrushpan et al. [16,17] developed a comprehensive control oriented model for the fuel cell stack and all its auxiliary components. The model is appropriate for many fuel cell control applications. It employs mass conservation principles, thermodynamic, and psychometric properties of the reactant gasses, as well as the flow characteristics, and the inertia dynamics of the compressor. Model parameters are obtained using a 75 kW FC stack from a Ford P2000 fuel cell prototype, an Allied Signal compressor, and a Nafion 117 membrane. They have provided simulation results to demonstrate the control system performance using their proposed dynamic model. However, lack of experimental validation for control of an actual fuel cell vehicle which incorporates this model is noticeable. This model is popular among FC researchers and has been used in various FC control development efforts as the plant model, such as the works in [18–20].

A fully analytic model of the PEM fuel cell is presented in [4]. Dynamics of the air and fuel supply systems are formulated in the state-space form to facilitate the usage of this model for control applications. The model is then linked with the steady-state model of the PEM fuel cell stack to show the impact of operating conditions on fuel cell performance. The system configuration is tightly matched with the vehicular fuel cell topology, where

the air supply system consists of an air compressor, a humidifier, a fuel cell cathode flow channel, and an outlet water separator. On the anode side, the system is composed of a pressure reducing valve, a hydrogen recirculation blower, and a fuel cell anode flow channel.

Using both theory and experiment, del Real et al. [21] developed a dynamic model for Ballard 1.2 kW PEM fuel cell stack, which has also been validated. They have presented an innovative approach for deriving the polarization curve. Also, this semi-empirical control oriented model can represent the thermal effect in an air cooled stack as well as in the flooding phenomenon.

In [22], a control oriented model for the air supply system together with an analytic model of hydrogen flow in the presence of hydrogen recirculation pump is provided. The model can explain the effect of gas flow, pressure, and humidity on the cell performance. However, it lacks experimental validation where it is only supported via simulation results. A dynamic model of a PEM fuel cell suitable for control design is presented in [23]. This model is also validated and has been employed in various works including [24–26].

A vast majority of fuel cell literature focuses on modeling and control strategies for a fully operational healthy fuel cell system. However, in the actual deployment of the cell, it is susceptible to possible damages. Therefore, it is vital to understand the behavior of the system in a faulty condition. Hydrogen transfer leak (HTL) due to the appearance of membrane pinholes is a common defect that could occur in any cell. These pinholes result in system malfunctions that could significantly deteriorate the cell performance. Relevant works on HTL are presented next.

1.2.2 Hydrogen transfer leak modeling

Different phenomena could eventually affect the membrane and result in the creation or growth of pinholes. These events are linked to thermal, mechanical or chemical processes [27]. In [28], effects of membrane pinholes on PEM fuel cell performance are discussed, and a method for leak detection based on the increasing anode pressure is discerned.

To analyze the gas permeation regarding diffusive and convective transports, the authors used a gas tracer concept in [29]. Despite being capable of measuring the transfer leak rate and detecting the location of pinholes, their proposed method is not practical as each cell in the stack demands a separate gas tracer.

Localization of defected cells in the stack in [30] is carried out by using the time response of the stack voltage drop, subjected to hydrogen sudden stop at the open circuit condition. However, their method lacks reliability regarding the precise location of the pinholes since various phenomena can result in OCV drop. For a membrane with pinholes, the rate of OCV drop is higher compared to those of an intact membrane. Employment of the OCV as a diagnostic tool for detection of leak formation and leak localization is also discussed in [31].

A novel diagnostic tool for a precise characterization of the in-situ hydrogen transfer leak in a PEM fuel cell was proposed in [27]. Their technique provided a formulation for hydrogen transfer leak rate based on the nitrogen flow rate, stack temperature, OCV, and the anode and cathode pressures. In [32], a model-based hydrogen leak detection method is presented, which relies on the mass conservation equations while taking into account the natural leak of the stack.

1.3 Fuel cell system control

To achieve a more efficient, durable, and cost-effective operation in a PEM fuel cell system, there exist different challenges where a well-designed control system plays a significant role in coping with them. In this work, control objectives are first, to maintain the fuel overpressure (FOP) at the desired level [33], and second, to control the hydrogen concentration (HC) above a designated level. The difference between the anode and cathode pressures, at the inlet side of the PEMFC stack, is known as the fuel overpressure. Hydrogen concentration refers to the amount of available hydrogen in the anode. HC control is carried out via purge control [34]. Control requirements for a fuel cell system mainly address the reactant's pressure or flow, to meet the design specifications. In the following sections, a summary of major previous works on FOP control as well as the HC control is provided.

1.3.1 Fuel overpressure control

Danzer et al. [14] applied a nonlinear model-based algorithm for multivariable control of the cathode pressure and the oxygen excess ratio. Their proposed modeling and control algorithm can also be applied to the anode side. A mass flow controller (MFC) and an outlet throttle are used as actuators. This control technique utilizes the flatness-based control principle and a tracking observer for estimating the oxygen partial pressure by measuring the pressure at the outlet throttle. A comparison between the performances of their proposed controller and a PI controller is provided to demonstrate the effectiveness of their approach. The effect of membrane pinholes and nitrogen crossover are not considered in their model.

Pukrushpan et al. [16, 17] have designed an observer based feed-forward and feedback controller for the air flow. The controller can handle the trade-off between the parasitic loss reduction and the quick net power output during the load current change. However, their control design lacks experimental validation.

A gain-scheduled control structure for regulating the fuel overpressure as well as the anode and cathode humidities is provided in [18]. Two actuators are used in the ejector based anode recirculation system including the dry hydrogen flow and the anode back pressure valve.

In [35], a control method for maintaining the fuel overpressure in the desired region is described. A mathematical model for the cathode side is used while hydrogen consumption is treated as a disturbance during power generation. The actuation is executed by the outlet throttle on the cathode side and the inlet pressure valve on the anode side. Experimental results have also been provided to show the controller performance. However, the effects of HTL are not considered in the control design.

Fuel overpressure control together with the control of the air stoichiometric ratio and the air pressure is discussed in [24] via simulation results, for a PEM fuel cell with hydrogen recirculation. This method used both linear and nonlinear control techniques by employing a linearized model of the system to achieve the performance requirements. A time-delay control is applied for controlling the reactant's flow rate as well as the stack fuel overpressure in [36], considering a complete model of the fuel cell system.

Application of the Model Predictive Control (MPC) method [37] in related fuel cell control problems is discussed in [38–43]. Using the MPC approach, actuator limitation as well as output constraints can be formulated as part of the control problem. FOP control in [33] is achieved via the Back Pressure Valve (BPV) in a PEM fuel cell system with the inclusion of HTL. Both model and controller are experimentally verified using the Ballard 3kW test station. The pneumatic modeling technique has been applied to capture the fuel supply system behavior. In [40], FOP control in a dead-ended anode configuration is carried out by the MPC approach during periodic purging.

1.3.2 Hydrogen concentration control

Various anode configurations with different fuel efficiency and cell performance are available. In a PEM fuel cell the phenomenon of gas crossover is inevitable, i.e., regardless of the membrane thickness or type, gas permeation will always take place. This is driven by the concentration gradient. Therefore, nitrogen (N_2) will cross over to the anode side due to the higher N_2 concentration on the cathode side. Accumulation of nitrogen on the anode side will eventually result in decay in the stack voltage as well as the cell performance. In an anode with recirculation configuration, it is necessary to model the N_2 gas build up on the anode side to design an active purge control.

Different anode configurations are depicted in Figure 1.4. In [44], a simple analytic model for the nitrogen gas build up on the anode side of a PEM fuel cell is provided. It has been shown that in a pure recirculation anode, dilution of hydrogen with nitrogen can significantly deteriorate the cell performance. A slight anode outlet flow bleed can considerably improve the performance by dropping the anode N_2 concentration. Effects of HTL are not considered in their work. The performance of a PEM fuel cell with a dead-ended anode structure is more prone to nitrogen (N2) accumulation [45, 46].

A complete study of the nitrogen build up in a PEM fuel cell is presented in [47]. According to this study, nitrogen crossover depends on several factors including the fuel N_2

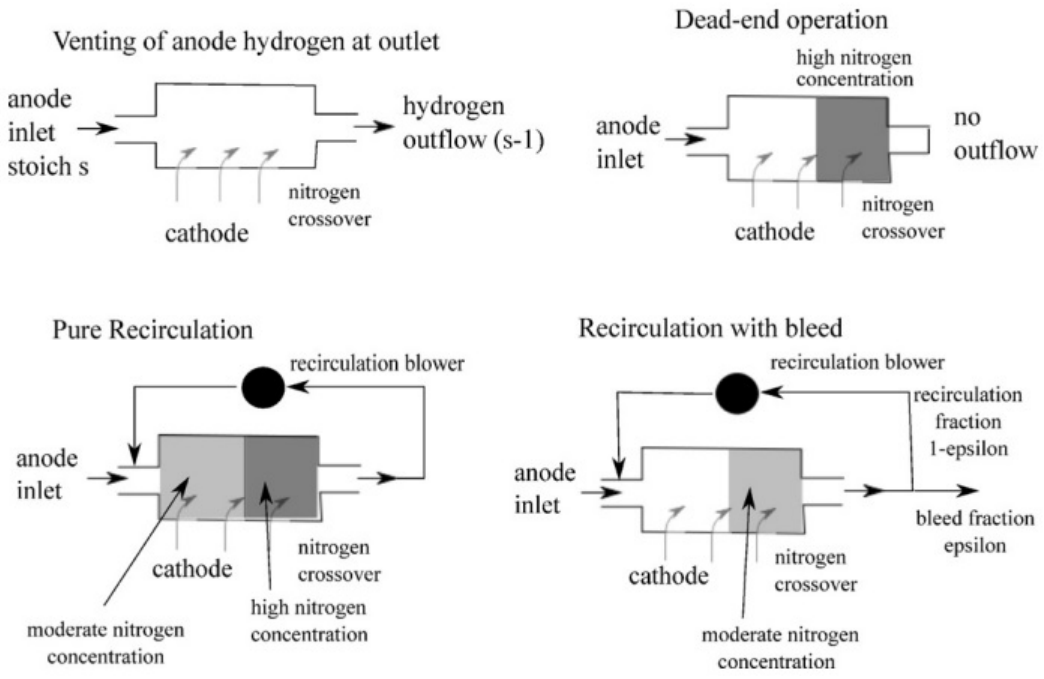

Figure 1.4: Different anode configurations [44] (used with the permission of Elsevier)

content, power level, membrane thickness, and the purge rate. Their study demonstrates the effect of N_2 build up on the performance of a 90 kW PEM fuel cell system. In a similar study [48], crossover of nitrogen is measured by the help of a mass spectrometer at different operating conditions, for both the OCV and power generation conditions. Based on this study, N_2 crossover increases with temperature in all relative humidity (RH) states.

A complete study of nitrogen crossover in a PEM fuel cell system with different purging strategies is presented in [49]. Using the validated stack data, the proposed model is verified. Simulation results for various purging techniques show that the anode bleed-out of 3% maintains the N_2 concentration to less than 1%. Both fixed and automatic purge intervals are simulated. However, no experimental verification of the purging strategies is presented. Furthermore, the effects of HTL are not included in the model. An anode purging strategy for a single cell PEM fuel cell is discussed in [50], using a mathematical model for estimation of nitrogen build up. The model is experimentally validated based on variations in the cell voltage.

1.4 Thesis objectives

The primary goals of this research are to address membrane longevity and fuel economy. In this thesis we address the following objectives:

- Dynamic modeling of the fuel supply system employed by the controller

- Fuel overpressure control in presence of hydrogen transfer leaks
- Hydrogen concentration control to enhance fuel economy

Modeling of the FSS is developed according to the anode configuration. Common FSS topologies are presented in chapter 2 along with more details on each configuration and their respective components. Furthermore, by deploying the pneumatic modeling technique, a dynamic model of the FSS is provided for each configuration together with the experimental validation.

Fuel overpressure control is thoroughly discussed in chapter 3. Using the model predictive control approach, the controller is designed and experimentally validated. More importantly, the effect of hydrogen transfer leak is included during the entire process. Besides improving the stack performance, FOP control could potentially reduce the hydrogen emission.

In a novel approach, a model-based method for estimation of anode hydrogen concentration is proposed in chapter 4. This approach is further employed in the multivariable control of hydrogen concentration and fuel overpressure. Finally, in chapter 5, this work is concluded by summarizing the key achievements as well as indicating the pathways for future works in this area.

1.5 Summary

Modeling and control of the fuel supply system used in various literature were summarized in the chapter. Some important control-oriented models that have been used extensively in the related fuel cell control studies were presented. Hydrogen transfer leak modeling was also discussed. Furthermore, an overview of some of the existing works in control of fuel overpressure and hydrogen concentration were provided. Finally, the objectives of this work were summarized.

Chapter 2

Modeling of Fuel Supply System

The fuel supply system encompasses all subsystems on the anode side which varies depending on the anode configuration. In this chapter, three primary FSS topologies, namely, the flow-through anode, the dead-ended anode, and the anode with recirculation (AWR) are explained. We will cover a detailed description of the components in each topology as well as the usage of each setup. The pneumatic modeling technique, covering both the plant and the actuator modeling, is also presented. Hydrogen leak characterization based on an ex-situ measurement setup is provided in this chapter. Finally, the results of the experimental validation for modeling each anode configuration are shown.

2.1 PEM fuel cell system configurations

There exist three primary anode configurations including, the flow-through anode, the dead-ended anode, and the anode with recirculation which are discussed next.

2.1.1 Flow-through anode

This anode configuration is primarily suitable for research purposes. Due to the continuous purging of hydrogen at the outlet, this setup possesses a poor fuel economy as the unused hydrogen is wasted. However, the flow-through mode provides a suitable platform to study the FC stack as well as the effects of various operating conditions on system performance. Furthermore, modeling and control algorithms can be developed and evaluated for this configuration before applying them to more practical setups.

Figure 2.1 shows the Piping and Instrumentation Diagram (P&ID) of the Ballard 3kW fuel cell test station with the flow-through anode. Considering the anode side in Figure 2.1, the main components are as follows:

- **Fuel delivery unit**: This comprises of the hydrogen reservoir as well as the input pressure regulator which reduces the pressure of the tank to below 40 psi (this pressure setpoint is adjustable).

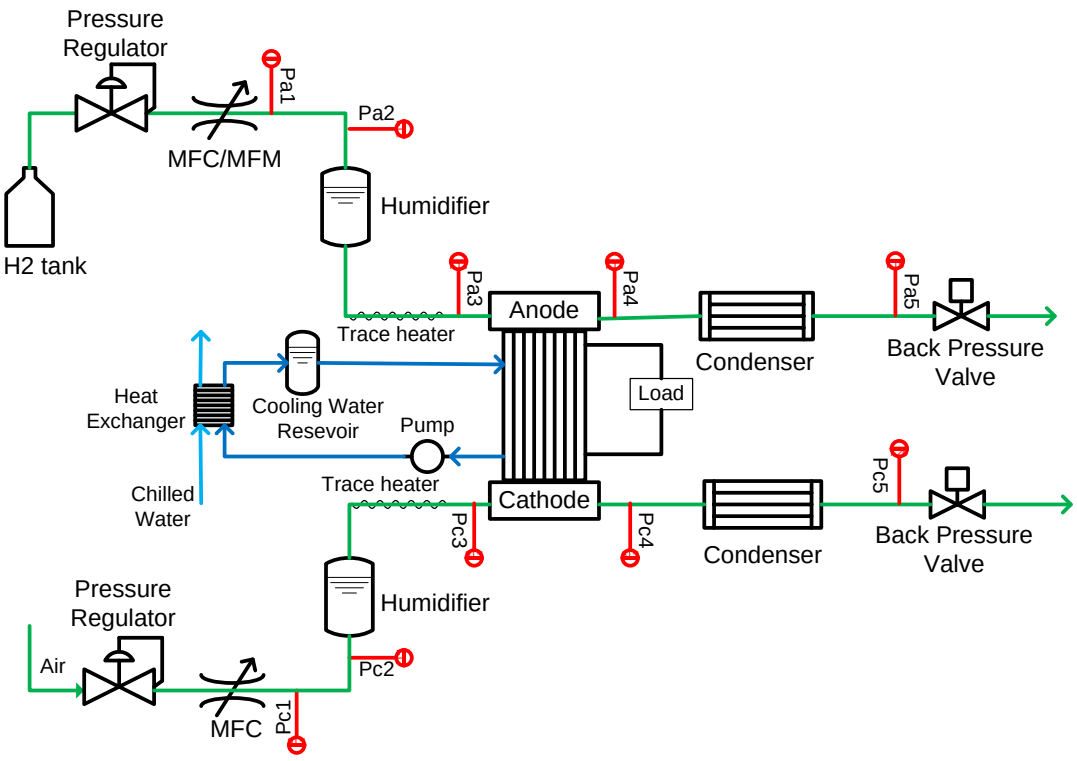

Figure 2.1: The schematic of the Ballard 3kW test station with the flow-through anode [33] (used with the permission of Elsevier)

- **Mass flow controller/meter**: The purpose of using a mass flow controller (MFC) is to adjust the anode input hydrogen flow rate. This device can also be employed in the mass flow meter (MFM) mode where it only measures the input hydrogen flow rate. The input H_2 flow rate is set according to the H_2 stoichiometry, λ, which is defined in the following:

$$\lambda = \frac{\text{amount of input hydrogen}}{\text{amount of hydrogen consumption}} = \frac{\dot{m}_{in}}{\dot{m}_c} \tag{2.1}$$

  where the inverse of λ is known as the hydrogen utilization.

- **Humidifier**: To improve the FC performance a humidification unit is used to increase the proton conductivity of the fuel cell membrane, which otherwise stays dry [2]. As shown in Figure 2.1, both anode and cathode sides are humidified, where on the cathode this increases the oxygen reduction reaction. Figure 2.2a shows the humidifier used in this study.

- **Fuel cell stack anode**: A 9-cell Mk1100 PEM fuel cell is utilized in this work.

- **Condenser**: A condenser is used to remove water from the anode. This water on the anode side is the result of humidification as well as the back-diffusion of water from

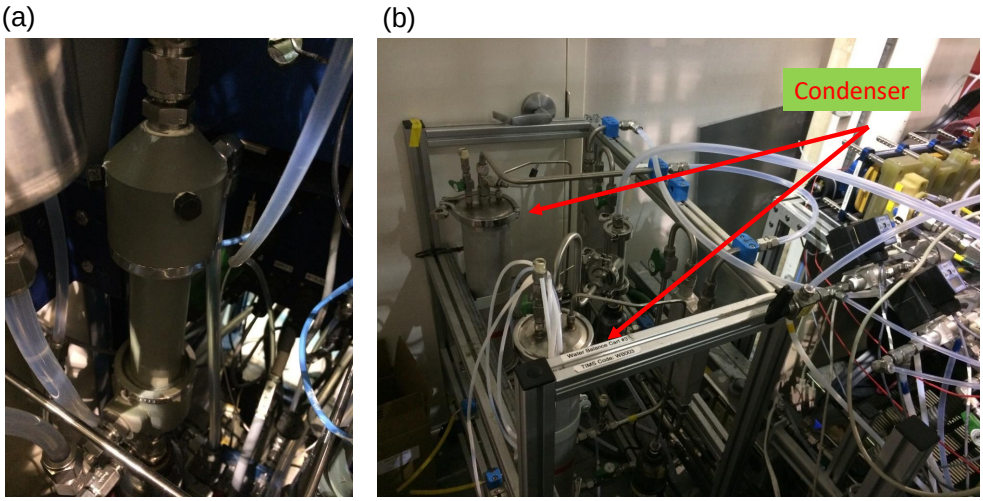

Figure 2.2: (a) Humidifier, (b) Condenser

the cathode side. The removal of water will improve the control action achieved by the actuator by protecting it from flooding. Figure 2.2b depicts the condenser unit that is deployed in this work. It is composed of 2 condenser units with a water separator for each unit. To ensure complete removal of water, an extra water separator is employed. The main reason for water removal is the protection of measurement devices, such as the MFM, whose functionality is jeopardized by liquid water.

Figure 2.3: A proportional solenoid valve

- **Back pressure valve**: This actuator in the flow-through anode is responsible for controlling the inlet pressure of the stack on the anode side based on the desired fuel overpressure. However, in the dead-ended anode or the AWR configurations, the back pressure valve (BPV) is utilized as the purge valve for controlling the fuel purging. The BPV is a proportional solenoid valve which is illustrated in Figure 2.3.

- **Pressure sensors**: Different pressure sensors are installed to monitor the changes in pressure at various spots on the anode side.

2.1.2 Dead-ended anode

Considering PEM fuel cell products, either the dead-ended anode or the anode with recirculation structures are deployed. In stationary systems, due to sizing flexibility, the dead-ended anode structure is commonly used. This configuration is more prone to N_2 crossover since the anode outlet path is blocked when the purge valve is closed. Figure 2.4 depicts the dead-ended anode setup where the air side configuration is similar to the one in Figure 2.1.

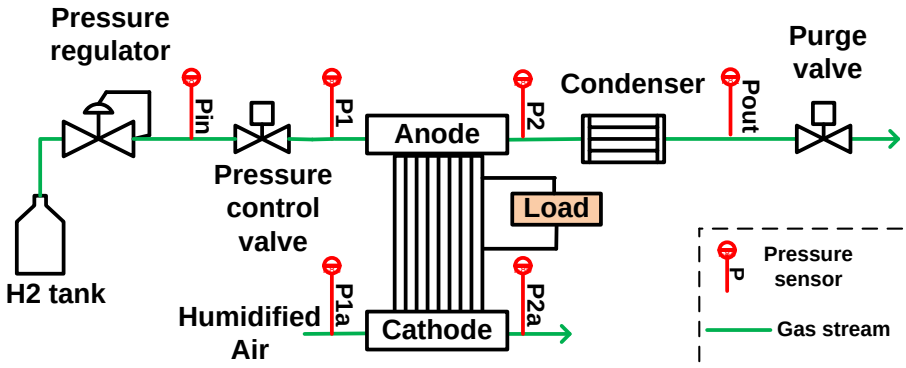

Figure 2.4: The schematic of the Ballard 3kW test station with the dead-ended anode [40] (used with the permission of IEEE)

Comparing Figures 2.1 and 2.4, the following changes in the setup are noticeable:

- **Pressure control valve**: This valve is used for regulation of the stack anode inlet pressure according to the required FOP. In flow-through mode, this pressure was controlled by the BPV.
- **Purge valve**: The BPV's role in this configuration is as a purge valve which aims at maintaining a higher anode H_2 concentration. In general, fuel purging is performed based on a timing scheme which can be periodic or dynamic.

2.1.3 Anode with recirculation

The AWR structure is the most efficient anode configuration which elevates H_2 utilization by recirculating the unused hydrogen back into the stack. A Hydrogen Recirculation Blower (HRB) is placed parallel to the fuel cell stack, as shown in Figure 2.5, illustrating the AWR configuration. The fuel cell stack and the HRB form a loop which is known as the *anode loop*. The P&ID of the PEMFC with AWR configuration is shown in Figure 2.6. Aside

from the aforementioned components for the dead-ended anode configuration, the following components are used in the AWR structure:

- **Hydrogen recirculation blower**: Using A brushless direct current (BLDC) motor, the HRB recirculates the anode gas mixture consisting of H_2 and N_2. To control the HRB pump speed, a control voltage V_{hrb} is applied. Table 2.1 provides the equivalent pump rotational speed for some selected V_{hrb}s.

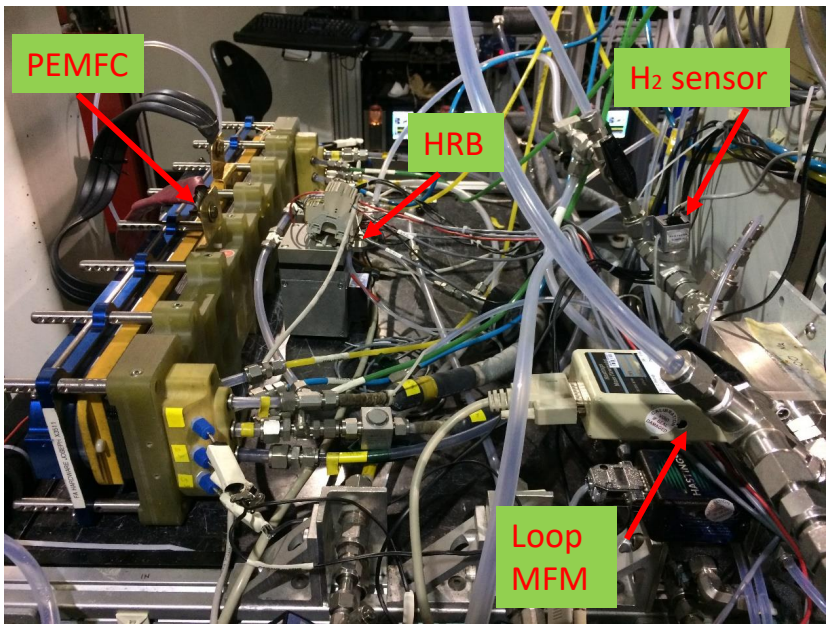

Figure 2.5: The Ballard 3kW test station with hydrogen recirculation blower

- **Anode loop MFM**: This flow meter is specifically used for measuring the gas mixture flow rate inside the *anode loop*. The flow meter is capable of measuring both H_2 and N_2 gas flow rates. The presence of the condenser inside the *anode loop* and before the MFM ensures secure operation of the MFM which is also shown in Figure 2.5.

  Table 2.1: The rotational speed of the HRB pump for selected control voltages

control voltage [V]	pump speed [rpm]
1	440
2	1032
3	1589
4	2171
5	2770

- **Hydrogen sensor**: A 0-5 volts hydrogen sensor from Neodym Technologies is employed for measuring the hydrogen concentration inside the *anode loop*. Similar to

the loop MFM, the H_2 sensor is operating safely, since it is not exposed to any water molecules due to the usage of the condenser. Table 2.2 shows the H_2 sensor voltage for some selected H_2 concentrations. This sensor is also highlighted in Figure 2.5.

Table 2.2: The hydrogen sensor voltage for various hydrogen concentrations

H_2 concentration [%]	sensor voltage [V]
100	4.8
90	4.8
85	4.6
80	4.3
75	4.0
70	3.8
65	3.6

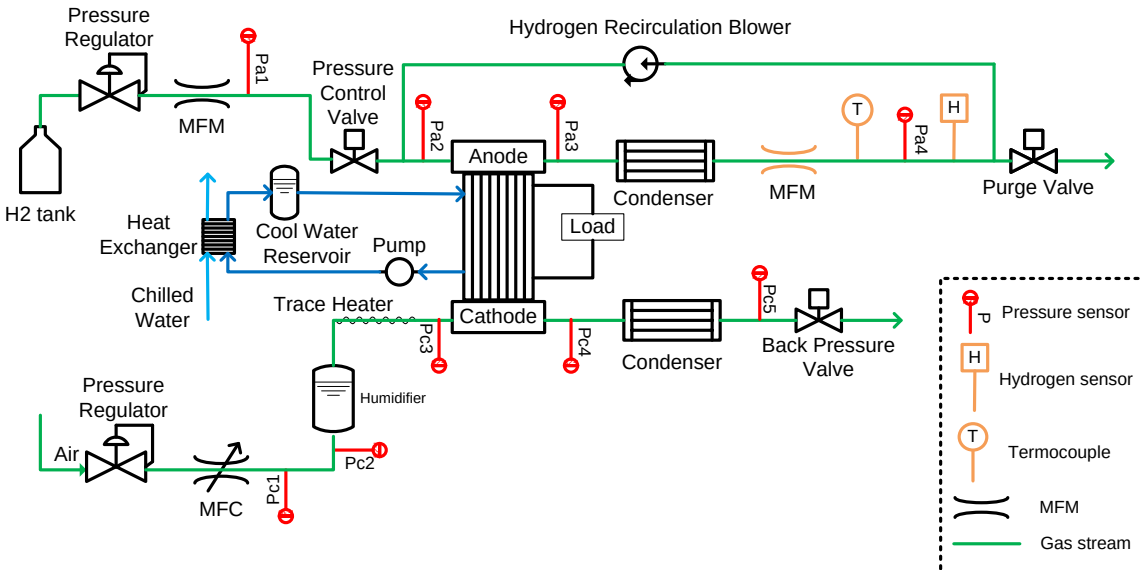

Figure 2.6: P&ID of the Ballard 3kW test station with anode recirculation

2.2 Pneumatic modeling

To capture the dynamic behavior of the entire PEMFC system, the pneumatic modeling approach introduced in [13] is utilized. According to this technique, each component is modeled by pneumatic variables such as the pneumatic resistor and the pneumatic capacitor. The friction forces in gas flow channels are reflected via pneumatic resistors while pneumatic capacitors express the storage potentials of components.

Depending on the flow regime, a pneumatic variable can be laminar or turbulent. This is decided by the Reynold's number, Re, where for $Re \geq 2500$ the flow is turbulent, and otherwise, it is laminar. In this work, the flow regime is laminar. Therefore, all pneumatic variables are laminar. Turbulent flows are likely to occur in high flow rates which cause the pneumatic variable to be nonlinear. For a laminar resistor (R_L), the following relation holds between the pressure drop across the resistor (ΔP), and the flow rate through the resistor (Q):

$$\Delta P = R_L Q \tag{2.2}$$

In the rest of this section, a pneumatic model of each anode configuration is developed first, followed by details of actuator modeling.

2.2.1 System model

Employing pneumatic variables, each of the aforementioned anode configurations can be modeled. Starting with the flow-through anode, Figure 2.7 illustrates the equivalent circuit of the system in Figure 2.1, in analogy to electrical systems.

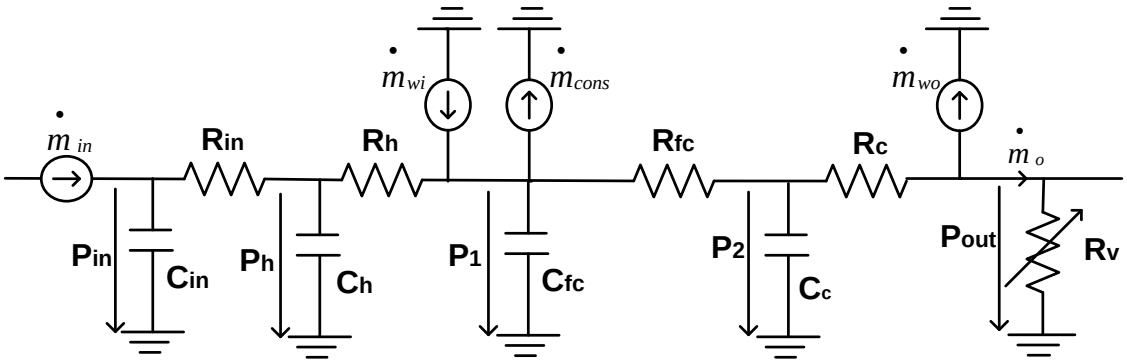

Figure 2.7: The pneumatic model of the flow-through anode

Pressure variables in Figure 2.7 point to the same nodes as in Figure 2.1. Each component located between two consecutive sensors is replaced by its pneumatic model. These include the inlet manifold, the humidifier, the PEM fuel cell anode, the condenser, and the BPV which is the actuator. The input hydrogen flow is expressed by a flow source since the MFC supplies a fixed flow rate depending on the load consumption as well as the H_2 stoichiometry. The added water by the humidifier is also represented by a flow source. Assuming 100% relative humidity [2], and in reference to the cathode side calculation provided in [13], the water mass flow rate is obtained as follows:

$$\dot{m}_{hum} = \frac{R_{H_2}}{R_{H_2O}} \frac{P_{sat}(T)}{P_1 - P_{sat}(T)} = 8.936 \frac{P_{sat}(T)}{P_1 - P_{sat}(T)} \qquad (T = 60^\circ C) \tag{2.3}$$

where P_{sat} is the saturation pressure of water. In addition to this, a back-diffusion of water from the cathode side and the drag of water molecules, due to electro-osmotic phenomenon [2], would also affect the total water flow rate which are not considered for this study. This leads to the same water mass flow rate as stated in (2.3), at the condenser knock out; i.e., $\dot{m}_{wo} = \dot{m}_{wi}$.

Moreover, the load consumption is also shown by a flow source in the model. This flow can be calculated using the Faraday's law as stated in the following:

$$\dot{m}_c = \frac{NI}{2F} \tag{2.4}$$

where N is the number of cells, I is the load current, and F is the Faraday's constant.

Lastly, the BPV is modeled as a variable resistor since as an actuator, it should be adjustable to regulate the pressure. The details of the actuator model are provided in section 2.2.2.

Using the pneumatic model in Figure 2.7, the flow-through anode configuration can be represented in a state-space form as follows:

$$\begin{cases} C_{in}\dot{x}_1 = -\dfrac{x_1 - x_2}{R_{in}} + w_1 \\ C_h\dot{x}_2 = \dfrac{x_1 - x_2}{R_{in}} - \dfrac{x_2 - x_3}{R_h} \\ C_{fc}\dot{x}_3 = \dfrac{x_2 - x_3}{R_h} - \dfrac{x_3 - x_4}{R_{fc}} + w_2 - w_3 \\ C_c\dot{x}_4 = \dfrac{x_3 - x_4}{R_{fc}} - \dfrac{x_4 - u}{R_c} \\ y = x_3 \end{cases} \tag{2.5}$$

where $x(t)$, $u(t)$, and $w(t)$ are expressed here:

$$\begin{cases} x(t) = \begin{bmatrix} P_{in}(t) & P_h(t) & P_1(t) & P_2(t) \end{bmatrix}^T \\ u(t) = P_{out}(t) \\ w(t) = \begin{bmatrix} \dot{m}_{in}(t) & \dot{m}_{wi}(t) & \dot{m}_{cons}(t) \end{bmatrix}^T \end{cases} \tag{2.6}$$

Therefore, the pressure variables on the anode side are the state variables which include the inlet manifold pressure, the humidifier inlet pressure, and the stack anode inlet and outlet pressures. Also, the hydrogen input flow rate, the water flow rate, and the H_2 consumption flow rate are included in the disturbance vector. To achieve a linear state-space model, the control input (u) is chosen as the output pressure instead of the valve resistor (R_v) in Figure 2.7. As will be clarified in section 2.2.2, the nonlinear valve model

is expressed as follows:

$$P_{out} = f(V_{in}, \dot{m}_o) \tag{2.7}$$

$$R_v = P_{out}/\dot{m}_o \tag{2.8}$$

where P_{out} is the output pressure, $\dot{m}_o$ is the output flow (Figure 2.7), and f is the nonlinear valve model. Therefore, by selecting P_{out} as the control input, the valve resistor can be calculated using (2.8). In the flow-through anode, the output flow can be written as stated here:

$$\dot{m}_o = \dot{m}_{in} - \dot{m}_{cons} - \dot{m}_{leak} \tag{2.9}$$

where $\dot{m}_{leak}$ is the leakage flow which is considered as zero at this point.

In a matrix form, the state-space model is written as follows:

$$\dot{x}(t) = Ax(t) + Bu(t) + Ew(t) \tag{2.10}$$

where matrices A, B, and E are defined below:

$$A = \begin{bmatrix} \frac{-1}{R_{in}C_{in}} & \frac{1}{R_{in}C_{in}} & 0 & 0 \\ \frac{1}{R_{in}C_h} & \frac{-R_{in}-R_h}{R_{in}R_hC_h} & \frac{1}{R_hC_h} & 0 \\ 0 & \frac{1}{R_hC_{fc}} & \frac{-R_{fc}-R_h}{R_{fc}R_hC_{fc}} & \frac{1}{R_{fc}C_{fc}} \\ 0 & 0 & \frac{1}{R_{fc}C_c} & \frac{-R_{fc}-R_c}{R_{fc}R_cC_c} \end{bmatrix} \tag{2.11}$$

$$B = \begin{bmatrix} 0 & 0 & 0 & \frac{1}{R_cC_c} \end{bmatrix}^T \tag{2.12}$$

$$E = \begin{bmatrix} \frac{1}{C_{in}} & 0 & 0 \\ 0 & 0 & 0 \\ 0 & \frac{1}{C_{fc}} & \frac{-1}{C_{fc}} \\ 0 & 0 & 0 \end{bmatrix} \tag{2.13}$$

Next, the pneumatic model of the dead-ended anode is depicted in Figure 2.8 based on the P&ID schematic in Figure 2.4.

Compared to the flow-through anode, there exist some differences in the model. Instead of an input hydrogen flow source, a voltage source is used. This stems from the fact that in the flow-through anode, the hydrogen flow can be set to any value since there is always a path for its exit (continuous purging). However, the dead-ended anode is subjected to

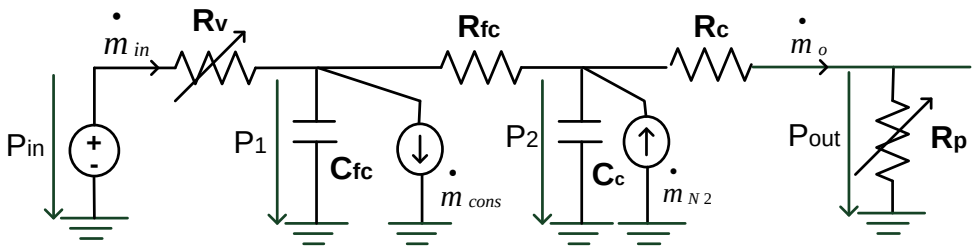

Figure 2.8: The pneumatic model of the dead-ended anode [40] (used with the permission of IEEE)

periodic or dynamic purging which affects the input flow rate. Therefore, the pressure after the upstream regulator which is constant is replaced with a voltage source. Moreover, there exist two actuators in this configuration, namely, the pressure control valve (R_v) and the purge valve (R_p). The humidifier is not used in this anode mode. Crossover of nitrogen is also reflected via a flow source. Considering Figure 2.8, the following equations can be written:

$$C_{fc}\dot{P}_1 = \frac{P_{in} - P_1}{R_v} - \dot{m}_{cons} - \frac{P_1 - P_2}{R_{fc}} \tag{2.14}$$

$$C_c\dot{P}_2 = \frac{P_1 - P_2}{R_{fc}} - \frac{P_2 - P_{out}}{R_c} + \dot{m}_{N_2} \tag{2.15}$$

$$\dot{m}_{in} = \frac{P_{in} - P_1}{R_v} \tag{2.16}$$

The purge valve operates in the ON-OFF mode which introduces significant pressure variations across the valve. Depending on the application, the purge valve can run periodically or dynamically. Assuming periodic purging, the output pressure is considered as a disturbance input and therefore, P_{out} is used in (2.15). The actuator command in (2.14) is the valve resistor R_v. However, to obtain a linear state-space model the input flow rate is assumed as the control input as stated in the following:

$$u_c = \dot{m}_{in} = \frac{P_{in} - P_1}{R_v} \tag{2.17}$$

The state-space formulation of the dead-ended anode with periodic purging can be developed as follows:

$$\begin{cases} C_{fc}\dot{x_1} = \dfrac{-x_1 + x_2}{R_{fc}} - w_1 + u \\ C_c\dot{x_2} = \dfrac{x_1 - x_2}{R_{fc}} + w_2 - \dfrac{x_2 - w_3}{R_c} \end{cases} \tag{2.18}$$

where $x(t)$, $u(t)$ and $w(t)$ are defined in (2.19):

$$\begin{cases} x(t) = \begin{bmatrix} x_1(t) & x_2(t) \end{bmatrix}^T = \begin{bmatrix} P_1(t) & P_2(t) \end{bmatrix}^T \\ u(t) = u_c(t) \\ w(t) = \begin{bmatrix} w_1(t) & w_2(t) & w_3(t) \end{bmatrix}^T = \begin{bmatrix} \dot{m}_{cons}(t) & \dot{m}_{N_2}(t) & P_{out}(t) \end{bmatrix}^T \end{cases} \tag{2.19}$$

The state variables are the stack anode inlet and outlet pressures. The control input signal (u) is the input flow rate as provided in (2.17). The disturbances w_1, w_2 and w_3 are the hydrogen consumption flow rate, the nitrogen crossover flow rate, and the output pressure, respectively. The consumption flow rate cannot be zero. In a matrix form, the state-space model is expressed as follows:

$$\begin{cases} \dot{x} = Ax + \overbrace{\left[\begin{array}{c:cc} B_1 & B_2 \end{array}\right]}^{B} \left[\begin{array}{c} u \\ \hdashline w \end{array}\right] \\ y = Cx \end{cases} \tag{2.20}$$

$$\begin{cases} A = \begin{bmatrix} \dfrac{-1}{R_{fc}C_{fc}} & \dfrac{1}{R_{fc}C_{fc}} \\ \dfrac{1}{R_{fc}C_c} & \dfrac{-R_c - R_{fc}}{R_c R_{fc} C_c} \end{bmatrix} \\ B = \left[\begin{array}{c:cc} \dfrac{1}{C_{fc}} & \dfrac{-1}{C_{fc}} & 0 \\ \hdashline 0 & 0 & \dfrac{1}{C_c} \end{array} \quad \begin{array}{c} 0 \\ \dfrac{1}{R_c C_c} \end{array}\right] \\ C = \begin{bmatrix} 1 & 0 \end{bmatrix} \end{cases} \tag{2.21}$$

The choice of matrix C depends on the control objectives where an arbitrary matrix is introduced in (2.21).

Lastly, the pneumatic model of the anode with recirculation is shown in Figure 2.9 for the schematic of the AWR configuration in Figure 2.6. There exist 3 actuators in the AWR structure where depending on the control task each of them could be utilized. These are the pressure control valve, the purge valve, and the HRB.

The HRB is shown with a variables flow source, and the effects of nitrogen and water are included in the model. Considering Figure 2.9. the following equations are valid:

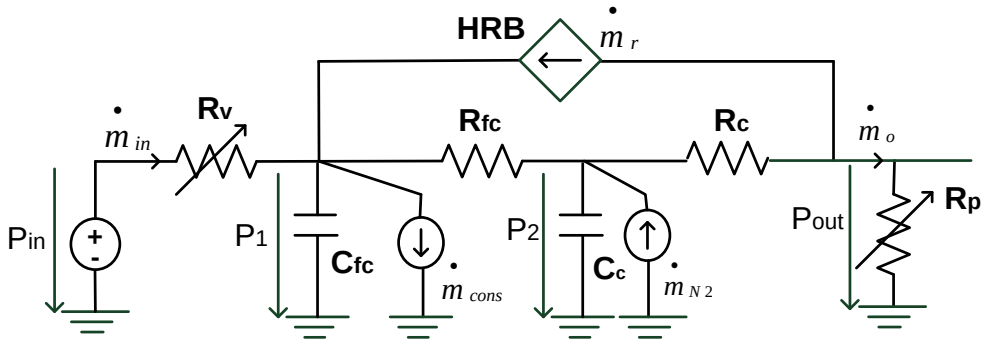

Figure 2.9: The pneumatic model of the anode with recirculation [34] (used with the permission of IEEE)

$$C_{fc}\dot{P}_1 = \frac{P_{in} - P_1}{R_v} + \dot{m}_r - \dot{m}_{cons} - \frac{P_1 - P_2}{R_{fc}} \tag{2.22}$$

$$C_c\dot{P}_2 = \frac{P_1 - P_2}{R_{fc}} - \frac{P_2 - P_{out}}{R_c} + \dot{m}_{N_2} \tag{2.23}$$

$$\frac{P_2 - P_{out}}{R_c} = \frac{P_{out}}{R_p} + \dot{m}_r \tag{2.24}$$

The choice of a state-space representation is directly related to the selection of controlled variables as well as control inputs. In [34], the control inputs are the pressure control valve (R_v) and the purge valve (R_p). The HRB operates at a fixed voltage. The state-space of the system is linearized around each operating condition in [34]. However, similar to the approach used for the other two anode configurations, nonlinear transformations, as provided in (2.25) and (2.26), can be used to linearize the system:

$$u_1 = \dot{m}_{in} = \frac{P_{in} - P_1}{R_v} \tag{2.25}$$

$$u_2 = \dot{m}_o = \frac{P_{out}}{R_p} \tag{2.26}$$

These nonlinear transformations lead to a linear state-space model as shown here:

$$\begin{cases} C_{fc}\dot{x_1} = \dfrac{-x_1 + x_2}{R_{fc}} - w_1 + w_2 + u_1 \\ C_c\dot{x_2} = \dfrac{x_1 - x_2}{R_{fc}} + w_2 + w_3 + u_2 \end{cases} \tag{2.27}$$

where $x(t)$, $u(t)$ and $w(t)$ are defined in (2.19):

$$\begin{cases} x(t) = \begin{bmatrix} x_1(t) & x_2(t) \end{bmatrix}^T = \begin{bmatrix} P_1(t) & P_2(t) \end{bmatrix}^T \\ u(t) = \begin{bmatrix} u_1(t) & u_2(t) \end{bmatrix}^T = \begin{bmatrix} \dot{m}_{in}(t) & \dot{m}_o(t) \end{bmatrix}^T \\ w(t) = \begin{bmatrix} w_1(t) & w_2(t) & w_3(t) \end{bmatrix}^T = \begin{bmatrix} \dot{m}_{cons}(t) & \dot{m}_r(t) & \dot{m}_{N_2}(t) \end{bmatrix}^T \end{cases} \tag{2.28}$$

The state-space model in (2.27) can also be expressed in a matrix form as provided in the following:

$$\dot{x}(t) = Ax(t) + Bu(t) + Ew(t) \tag{2.29}$$

where matrices A, B, and E are as follows:

$$\begin{cases} A = \begin{bmatrix} \dfrac{-1}{R_{fc}C_{fc}} & \dfrac{1}{R_{fc}C_{fc}} \\ \dfrac{1}{R_{fc}C_c} & \dfrac{-1}{R_{fc}C_c} \end{bmatrix} \\ B = \begin{bmatrix} 1 & 0 \\ 0 & 1 \end{bmatrix} \\ C = \begin{bmatrix} -1 & 1 & 0 \\ 0 & 1 & 1 \end{bmatrix} \end{cases} \tag{2.30}$$

2.2.2 Actuator model

Depending on the PEM fuel cell configuration and the control objectives, actuator signals are then chosen. In the flow-through anode only the back pressure valve is the actuator. In the dead-ended anode, the pressure control valve and the purge valve are the actuators where one or both can be used as control commands. In the AWR configuration, the HRB is also an actuator, in addition to the pressure control valve and the purge valve.

In this study, the valves (both the pressure control valve and the purge valve) are proportional solenoid valves. By applying an input control voltage, the valve orifice is opened commensurate with the voltage. Considering the pneumatic model of the valve, changing the control voltage would affect the valve resistor. In general, the dynamic behavior of the valve can be expressed in this manner:

$$\Delta P_v = f(V_{in}, Q_v) \tag{2.31}$$

$$R_v = \Delta P_v / Q_v \tag{2.32}$$

where ΔP_v is the pressure across the valve, and Q_v is the flow through the valve.

In the previous section, the system model was represented in a linear state-space form. All nonlinear transformations that were used in different anode configurations for deriving a linear model include the valve resistor at the denominator. For instance, looking at equations (2.25) and (2.26) both R_v and R_p are located at the denominator. Once the control action is determined by the controller, using the valve model and the pressure measurements, the control input of the valve can be calculated as stated by (2.33). The valve modeling results are provided in Section 2.4.2.

$$V_{in} = f^{-1}(\Delta P_v, Q_v) \tag{2.33}$$

The hydrogen recirculation blower is controlled by input voltage that is applied to a Brushless Direct Current (BLDC) motor. To accurately model the HRB, knowledge about the BLDC motor is required. A more practical approach is to obtain a model reflecting the HRB's role in the system in a real scenario. This results in determining the recirculated flow by the HRB for various stack anode inlet pressures and input voltages as stated by the function g:

$$Q_{hrb} = g(P_{hrb}, V_{hrb}) \tag{2.34}$$

where based on Figure 2.9, this can be written as follows:

$$Q_r = g(P_1, V_{hrb}) \tag{2.35}$$

As will be clarified in chapter 4, N_2 crossover will decrease the H_2 concentration on the anode side. Depending on the hydrogen gas concentration (x_h), Q_r can be different for the same inlet pressure and input voltage. Therefore, (2.35) can be extended to include various H_2 concentrations:

$$Q_r = g(P_1, V_{hrb}, x_h) \tag{2.36}$$

Another way of describing the HRB dynamic response is to use the pressure drop across the HRB (ΔP_{hrb}) instead of the inlet pressure, in which case there is no need to include x_h in the HRB model. In fact, x_h affects the pressure drop. Therefore, x_h can be dropped from the model as stated in (2.37). However, in practice this requires keeping the pressure dropped, as well as the input voltage at fixed values to measure the Q_r, where maintaining a fixed pressure drop is not trivial.

$$Q_r = g(\Delta P_{hrb}, V_{hrb}) \tag{2.37}$$

Therefore, the model in (2.35) is used as the HRB model without having to include the BLDC motor characterization. The result of HRB dynamic modeling is also provided in Section 2.4.2.

2.3 Hydrogen transfer leak model

During the system modeling, leakage of hydrogen due to membrane pinholes was not considered in the model. In fact, HTL is a very common defect in PEM fuel cell systems. In the pneumatic system model, HTL can be added as an additional flow source that is placed at either side of the stack depending on the location of pinholes. In the flow-through anode configuration, as provided in [33], this is placed at the inlet side of the stack as shown in Figure 2.10:

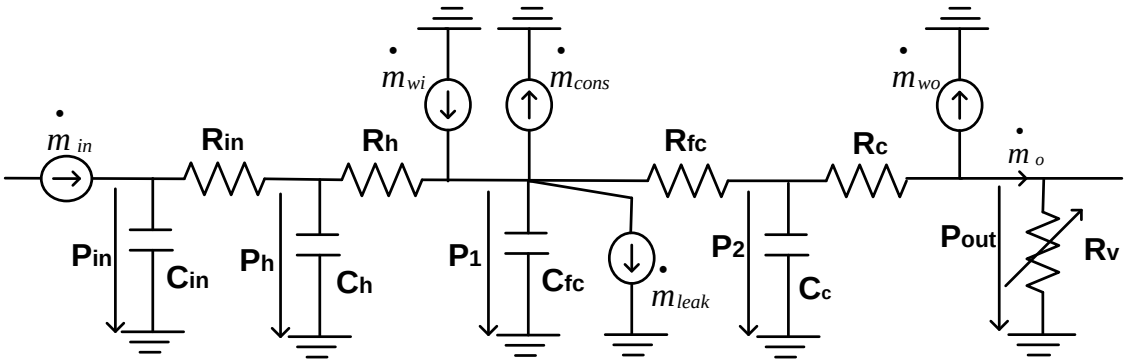

Figure 2.10: The inclusion of hydrogen transfer leaks in the pneumatic model [33] (used with the permission of Elsevier)

In a similar way, HTL can be included in the other anode configurations. In general, HTL is a function of leak size as well as fuel overpressure as stated in [27]:

$$Q_{leak} = H(s, \text{FOP}) \tag{2.38}$$

where s indicates the leak size while FOP is the fuel overpressure. Depending on the leak rate, pinhole sizes are categorized as small, medium, and large, respectively. Since membrane pinholes accelerate the degradation process, it is necessary to control or reduce the leak rate. Therefore, including the HTL model will facilitate the control task. In the state-space model, HTL is included in the disturbance vector as stated in the following for the flow-through anode:

$$\begin{cases} C_{in}\dot{x}_1 = -\dfrac{x_1 - x_2}{R_{in}} + w_1 \\ C_h\dot{x}_2 = \dfrac{x_1 - x_2}{R_{in}} - \dfrac{x_2 - x_3}{R_h} \\ C_{fc}\dot{x}_3 = \dfrac{x_2 - x_3}{R_h} - \dfrac{x_3 - x_4}{R_{fc}} + w_2 - w_3 - w_4 \\ C_c\dot{x}_4 = \dfrac{x_3 - x_4}{R_{fc}} - \dfrac{x_4 - u}{R_c} \\ y = x_3 \end{cases} \tag{2.39}$$

$$\begin{cases} x(t) = \begin{bmatrix} P_{in}(t) & P_h(t) & P_1(t) & P_2(t) \end{bmatrix}^T \\ u(t) = P_{out}(t) \\ w(t) = \begin{bmatrix} \dot{m}_{in}(t) & \dot{m}_{wi}(t) & \dot{m}_{cons}(t) & \dot{m}_{leak}(t) \end{bmatrix}^T \end{cases} \tag{2.40}$$

Similarly, the state-space model of the dead-ended anode and AWR configurations can be extended to include hydrogen transfer leaks as a disturbance in the model. Characterization of hydrogen transfer leaks is provided in Section 4.2.3.

2.4 Results

In this section, modeling results are presented which includes parameter identification as well as experimental validation of the model. Moreover, characterization of the hydrogen transfer leak using the ex-situ measurement setup is provided.

2.4.1 System model parameters

Considering the flow-through anode system in Figure 2.10, the following parameter vector is defined:

$$\Psi = \begin{bmatrix} R_{in} & R_h & R_{fc} & R_c & C_{in} & C_h & C_{fc} & C_c \end{bmatrix}^T \tag{2.41}$$

As already mentioned, the flow regime as well as the parameters are laminar. To derive parameters, a series of input hydrogen flow rates are supplied to the anode side, and the pressure sensor values are measured [13]. During this, the BPV is fixed at the fully opened position ($V_{in} = 10$) to disengage the actuator effect [13]. Setting the valve in any other position ($V_{in} < 10$) would not affect the laminar variables.

For parameter identification, the following least square function has to be minimized [13]:

$$\Phi = \sum_{k=1}^{N} \left(y_{mea}(k) - y_m(k)\right)^2 \tag{2.42}$$

where y_{mea} is the measurement vector, and y_m is the equivalent pneumatic model of each component in the linear subsystem [42]. Figure 2.11(a) illustrates the test scenario used for parameter identification while Figure 2.11(b) depicts the verified simulation model with the experimental data. The simulation model is developed using Simulink environment in Matlab based on the procedure explained in [13]. Table 2.3 summarizes the identified parameters.

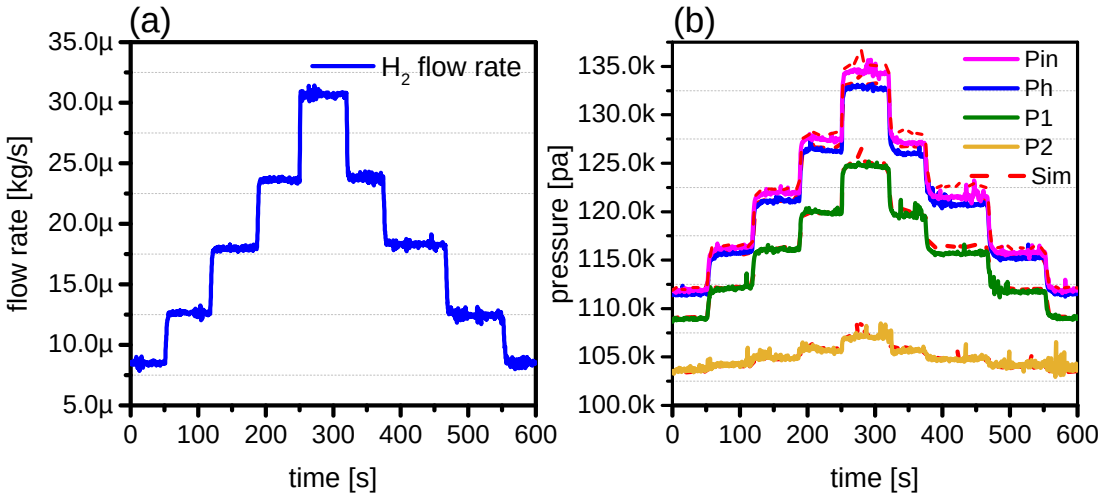

Figure 2.11: (a) The input hydrogen flow rate intended for parameter identification, (b) Verification of the simulation model with the experimental data [33] (used with the permission of Elsevier)

Table 2.3: Model parameters on the anode side [33] (used with the permission of Elsevier)

Parameter	Value	Unit
C_{in}	2.6×10^{-9}	ms^2
C_h	2.4×10^{-9}	ms^2
C_{fc}	6.8×10^{-9}	ms^2
C_c	9.8×10^{-9}	ms^2
R_{in}	6.2×10^{7}	$(\text{ms})^{-1}$
R_h	2.8×10^{8}	$(\text{ms})^{-1}$
R_{fc}	2.3×10^{8}	$(\text{ms})^{-1}$
R_c	0.5×10^{8}	$(\text{ms})^{-1}$

2.4.2 Actuator characterization

Both the pressure control valve (located upstream of the stack) and the purge valve (located at the anode outlet) are proportional solenoid valves. To obtain the nonlinear valve dynamic,

for various hydrogen flow rates, the valve input voltage is changed, and the pressure across the valve is measured. To run this test, the load current is set to zero to avoid the load effect. Also, the PEM fuel cell stack includes intact membranes only. This will result in a complete look up table representing the actuator model. The valve characteristic function has been introduced in a general continuous form via (2.31) and (2.33). Actuator modeling is shown in Figure 2.12 where P_{out} is the pressure across the valve which was denoted by u in (2.5) and (2.6).

In high flow rates ($\dot{m}_{in} \geq 6$ slpm), variations of the hydrogen flow would only slightly affect the curve in $P_{out} - V_{in}$ plane. Therefore, one average function for the $P_{out} - V_{in}$ curve is used at high flow rates. Similarly, for the low hydrogen flow rates ($\dot{m}_{in} < 6$ slpm), a new average function is deployed. The valve is of a solenoid type and has a small level of hysteresis (less than 3%) in its voltage-flow response. This hysteresis is neglected. Among different nonlinear curve-fitting methods, the exponential function closely describes (2.33) as provided in Table 2.4. Applying (2.33) to the flow-through anode configuration of Figure 2.10, the following holds:

$$V_{in} = f^{-1}(P_{out}, \dot{m}_o) \tag{2.43}$$

The operating range for V_{in} is between 0 to 10 V. However, as illustrated in Table 2, this range is limited to between 2.5 and 6 V for ($\dot{m}_{in} \geq 6$ slpm), and to between 2.5 and 5.1 V for ($\dot{m}_{in} < 6$ slpm). This is due to the orifice size of the valve which is incorporated in this work. The valve is capable of operating at much higher flow rates (≈ 1000 slpm) while the maximum hydrogen flow rate used in this study is only 50 slpm.

Table 2.4: The valve characterization (P_{out} is relative to $P_{atm} \approx 1$bar) [33] (used with the permission of Elsevier)

$\dot{m}_{in}$ [slpm]	P_{out} [kPa]	V_{in} [V]
$\dot{m}_{in} < 6$	$P_{out} \geq 150$	2.5
$\dot{m}_{in} < 6$	$P_{out} \leq 1$	5.1
$\dot{m}_{in} < 6$	$1 < P_{out} < 150$	$9.3e^{-0.002P_{out}} + 3.9e^{-2.9\times10^{-6}P_{out}}$
$\dot{m}_{in} \geq 6$	$P_{out} \geq 160$	2.5
$\dot{m}_{in} \geq 6$	$P_{out} \leq 2$	6
$\dot{m}_{in} \geq 6$	$2 < P_{out} < 160$	$4.1e^{-0.0004P_{out}} + 4.2e^{-3.2\times10^{-6}P_{out}}$

The next actuator is the hydrogen recirculation blower whose model was explained in Section 2.2.2. The HRB dynamic behavior is shown in Figure 2.13 for various stack inlet pressures and input voltages. Assuming that the purge valve operates periodically, the H_2 concentration remains close to 100%. Therefore, in Figure 2.13 only the pure hydrogen case ($x_h = 1$) is illustrated.

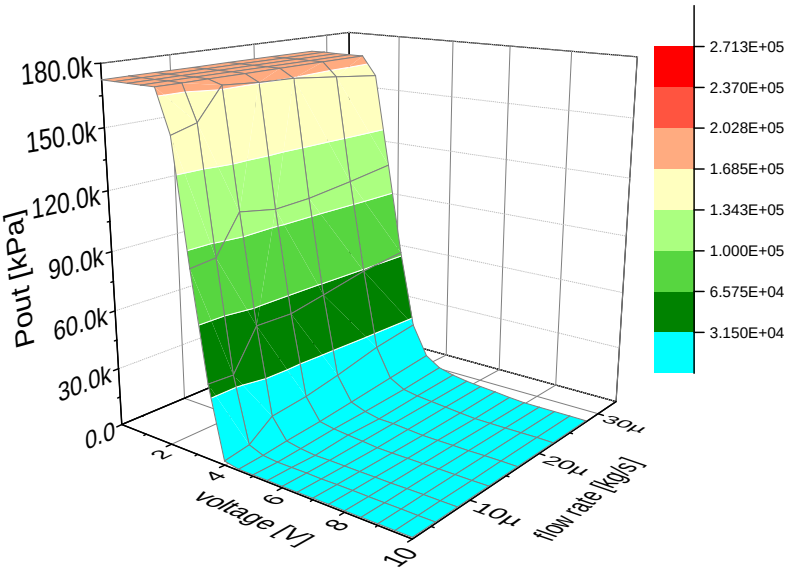

Figure 2.12: The 3D model of the valve characteristic function [33] (used with the permission of Elsevier)

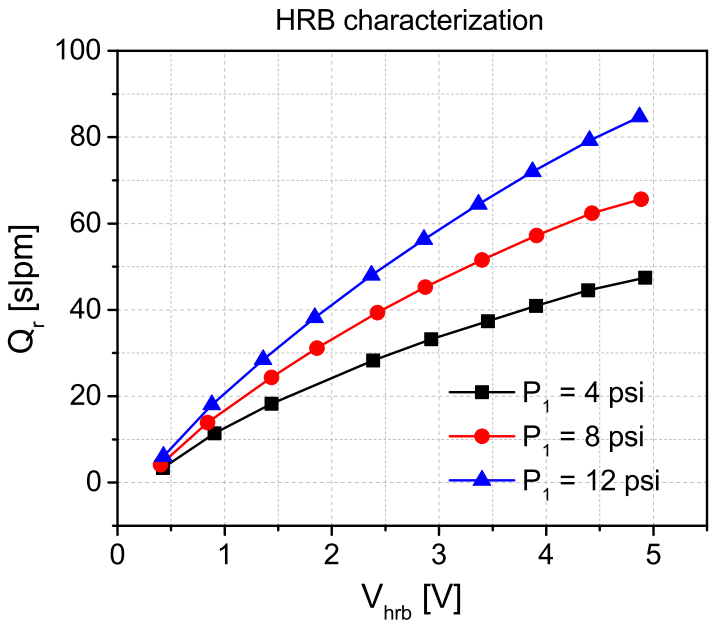

Figure 2.13: The HRB characterization for various anode stack inlet pressures

2.4.3 Hydrogen transfer leak characterization

Different approaches for measuring the HTL flow rate are presented in [27] and [32]. In this study, different membranes with small, medium, and large leak sizes are employed. The sizing of the membrane pinholes is decided according to the data in Table 2.5, which is defined specifically for this study.

Table 2.5: Leak size classification for cross-pressure $\in [1, 7]$ psi [33]

Leak size	ex-situ leak rate [sccm]
Small(S)	$0 < \dot{m}_{leak} \leq 15$
Medium(M)	$15 < \dot{m}_{leak} \leq 50$
Large(L)	$\dot{m}_{leak} > 50$

To classify the available membranes in terms of their respective leak sizes, the ex-situ crossover measurement setup at Ballard, described in [27], was used. In Figure 2.14, for the selected membranes, the results of the leak size measurements are shown.

As can be seen in Figure 2.14, the leak rate is typically proportional to the cross-pressure between the anode and cathode sides. To build a fuel cell stack with 9 cells, a combination of 8 intact membranes and a single leaky membrane was used. This was placed in the middle of the stack as the fifth cell. As already mentioned, the rate of the hydrogen transfer leak is a function of FOP and leak size [27].

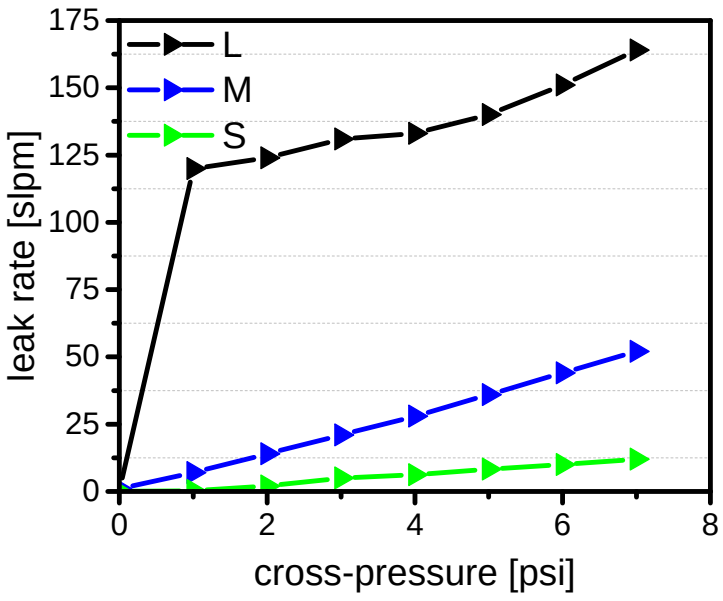

Figure 2.14: Characterization of hydrogen transfer leaks for three different sizes of pinholes: Large(L), Medium(M), and Small(S) leak sizes [33] (used with the permission of Elsevier)

2.5 Summary

Modeling of the fuel supply system was discussed in detail. Various configurations of the fuel supply system and their differences in components and applications were presented. Using the pneumatic modeling technique, each component was replaced by a pneumatic representation, and then, the state-space model of each FSS configurations was obtained. Actuator characterization as well as modeling of the hydrogen transfer leaks were also explained. Lastly, the experimental results were provided.

Chapter 3

Fuel overpressure control

Fuel overpressure control can substantially mitigate the effect of membrane pinholes in performance degradation of PEMFCs by reducing the transfer of reactants through the membrane. Furthermore, FOP control prolongs the lifetime of an intact membrane by limiting excessive pressures across the MEA. In this chapter, a comprehensive discussion on fuel overpressure control in various anode configurations is provided.

3.1 Control architecture

In chapter 2, the state-space model of various anode configurations was explained whereby using a nonlinear transformation, a linear model was obtained. Both the linear model and the nonlinear transformation should be included in the control architecture. Depending on the control problem, the architecture can be different. In PEM fuel cell applications, FOP control is usually carried out as part of a larger multivariable control problem. Therefore, different architectures can be adopted which encompass FOP control.

Considering fuel overpressure control alone, Figure 3.1 illustrates the control architecture:

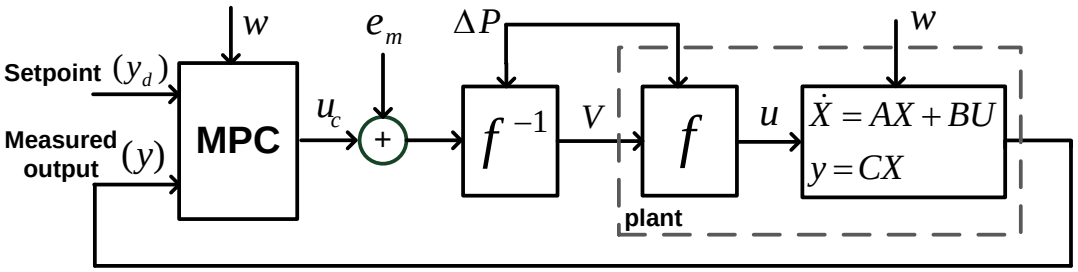

Figure 3.1: The control architecture for FOP control with an MPC controller (used with the permission of Elsevier)

The controller used in Figure 3.1 is the Model Predictive Controller (MPC). y_d is the FOP setpoint. u_c is the control input which could be the pressure across the valve as in (2.6), or the flow through the valve as in (2.17). f is the actuator model. In case of no modeling mismatch ($e_m = 0$), $f.f^{-1} = 1$, and hence, $u = u_c$. However, if there exists a modeling error, the actual control command (u_c) will be different from the computed command (u). If u_c represents flow, then according to (2.43), to obtain the valve input voltage (V_{in}), pressure measurement (ΔP) is required. e_m represents uncertainties due to the plant modeling error or any other unknown disturbance (e.g., HTL). The state-space model was provided in (2.39) and (2.40).

3.2 Control design

The main controller objective is to maintain the fuel overpressure, at the inlet side of the PEMFC stack, within a specified region. To explain all details of control design, the flow-through anode in Figure 2.10 is considered. The control design can be further extended to multivariable control systems. The PEMFC stack can include degraded membranes with pinholes. These pinholes cause a portion of the H_2 flow to depart from the anode and migrate to the cathode. From the control perspective, the change in the H_2 flow rate affects the pressure where the controller is responsible for the pressure recovery. This is especially important in the case of large transfer leaks. Moreover, the change of flow would influence the valve characteristic function. Note that Figure 2.12 was obtained using a PEMFC stack with intact membranes. Therefore, the controller has to ensure the robustness of the response to uncertainties.

Furthermore, the control problem is subjected to a number of constraints on the control input as well as the system output. Therefore, the control problem is formulated as a constrained control problem. The model predictive control method is used to achieve the control objectives as well as to handle problem constraints. Regarding the output error minimization with minimum changes of the control effort, MPC provides an optimal control input [37]. Applicability to multivariable systems, ability to satisfy problem constraints, and providing an optimal control input, make MPC a more powerful control approach than the PID controller. Utilization of MPC, as the state of the art technology, in industrial control applications, has grown significantly during recent years [37].

3.2.1 Performance requirements and problem constraints

As mentioned earlier, there are some requirements and constraints that are explained next.

1) *Membrane safety*: This requires the FOP to always stay above zero. This ensures no crossover of oxygen to the anode side upon the presence of pinholes. The occurrence of the reaction on the membrane surface on the anode side could severely damage the membrane and undercut local hydrogen availability to the cell. This imposes an output constraint as

follows:

$$y(t) - P_{c3}(t) \geq 0 \Longrightarrow FOP(t) \geq 0 \tag{3.1}$$

where P_{c3} is the stack inlet pressure on the cathode side, as shown in Figure 2.1. The FOP setpoint falls between 0 to 2.5 psi for the safest and more durable operation of the membrane. The control system promptly responds to the variation of P_{c3} to maintain the FOP at a prescribed value. However, due to the possible latency in the controller reaction, the FOP is not chosen near zero to avoid a feasibility issue for the MPC. In this work, the setpoint for FOP has been chosen at 1 psi. Therefore, the controller should comply with (16) during both transient and steady state operations.

2) *Cell durability*: To increase the longevity of a fuel cell membrane, from the system perspective, fuel overpressure is bound by an upper limit to prevent the exertion of excessive pressure across the membrane, as stated below:

$$y(t) - P_{c3}(t) \leq P_{max} \Longrightarrow FOP(t) \leq P_{max} \tag{3.2}$$

where P_{max} is chosen at 8 psi for this work.

3) *Actuator limitation*: The range and slew rate of the valve are restricted as provided here:

$$u_{min} \leq u(t) \leq u_{max} \tag{3.3}$$

$$\dot{u}_{min} \leq \dot{u}(t) \leq \dot{u}_{max} \tag{3.4}$$

As explained earlier, the operating range for V_{in} is from 0 to 10 V. Furthermore, based on Table 2.4, due to the valve orifice size, this range is limited. Based on this, for $\dot{m}_{in} \geq 6$ slpm, the valve fully opens for $V_{in} \geq 6$ V, and fully closes for $V_{in} \leq 2.5$ V. This changes to between 2.5 and 5.1 V for $\dot{m}_{in} < 6$ slpm. Therefore, to ensure that the valve operates between the two boundaries, u_{min} is set at 2.6 V, and u_{max} is chosen at 5.9 V and 5 V for high and low flow rates, respectively. Using (2.7) and Table 2.4, these actuator limitations can be described in terms of P_{out}.

3.2.2 Control problem formulation

According to (2.7), the input u (P_{out}) to the state-space model is a function of V_{in}. The inverse of this function in (2.43), as presented in Table 2.4, is used to convert the control input u_c to V_{in} as shown in the control architecture of Figure 3.1.

Remark 1. *In the control problem formulation, HTL is not considered in the prediction model since it is an unknown disturbance during the system operation. Hence,* $\dot{m}_{leak} = 0$. *This is a critical assumption for solving the MPC optimization problem, which makes*

the model to be independent of unknowns. In Section 3.2.3, the effect of HTL as a non-measurable disturbance is considered.

Since the problem encompasses multiple constraints to be handled, MPC is utilized. Using an internal model, MPC predicts the system output, $\hat{y}$, over the prediction horizon, H_p. Consequently, MPC determines the future set of control inputs, $\hat{u}$, that minimizes the cost function J in (3.5). For now, we assume that a perfect plant model is available. Therefore, the actual and predicted outputs are the same, i.e., $y = \hat{y}$. The same assumption is applied to the actual and estimated control input. Throughout this section, the discrete time notation is used where $t = kT_s$ with T_s as the sampling time.

$$J(k) = \sum_{i=H_w}^{H_p} \|y(k+i|k) - r(k+i|k)\|^2_{Q(i)} + \sum_{i=0}^{H_u-1} \|\Delta u(k+i|k)\|^2_{R(i)} \tag{3.5}$$

where matrices $Q \geq 0$ and $R \geq 0$ penalize the output error, and the control input, respectively [37]. $r(k)$ is the reference trajectory, and H_u is the control horizon, which is usually set lower than the prediction horizon. Moreover, H_w determines the start of the output error penalization. Since the problem is subjected to various constraints, a constrained optimization problem has to be solved at each sampling time.

$$\min_{\Delta U_t} J(y, \Delta u) \tag{3.6}$$

subject to:

$$x(k+i+1|k) = A_d x(k+i|k) + B_d u(k+i|k) + E_d w(k+i|k) \tag{3.7}$$

$$u(k+i|k) = u(k+i-1|k) + \Delta u(t+k|k) \tag{3.8}$$

$$x(k|k) = x(k) \tag{3.9}$$

$$u(k-1|k) = u(k-1) \tag{3.10}$$

$$w(k|k) = w(k) \tag{3.11}$$

$$u_{min} \leq u(k+i|k) \leq u_{max} \tag{3.12}$$

$$\Delta u_{min} \leq \Delta u(k+i|k) \leq \Delta u_{max} \tag{3.13}$$

$$y_d - \gamma_{min} \leq y(k+i|k) \leq y_d + \gamma_{max} \tag{3.14}$$

where $\Delta U_t = [\Delta u(k), \cdots, \Delta u(k+H_u-1)]$ is the vector of future control input increments that is the solution to the optimization problem (3.5). For $H_u \leq i \leq H_p-1$, the control input u remains unchanged. Therefore, $\Delta u(k+i) = \Delta u(k+H_u-1)$. In (3.7), A_d, B_d, and E_d are obtained from the discretization of the continuous state-space model. Actuator limitations

are reflected via (3.12 - 3.13), while the membrane safety and the cell durability constraints are expressed in (3.14). Formulations (3.6 - 3.14) are based on the control structure in Figure 3.1 assuming no modeling mismatch. Therefore, no uncertainty is considered in deriving them. Consequently, u and u_c are equal. However, the actual actuator limitation is on the range and the slew rate of the valve, where using (2.7) and Table 2.4 these constraints on the valve input voltage can be described in terms of u (P_{out}).

The solution to the Quadratic Programming (QP) problem in (3.5) can be found analytically by having a linear model of the system. Ensuring the existence of a feasible solution is the main challenge in the application of MPC. Actuator constraints cannot be violated. However, the output constraint can be softened if a feasibility problem occurs [37, 42]. The convex cost function J in (3.5), with the linear equality constraint (3.7), and the convex inequality constraints (3.12 - 3.14), form a convex problem. Therefore, any local optimum is also a global optimum.

3.2.3 Stability and robustness

In this section, a brief overview of the system stability and robustness is presented. A more comprehensive survey on these aspects of the MPC approach is provided in [51].

1) *Stability*: The open loop stability is verified via the eigenvalues of matrix A in the state-space model. To ensure stability of the open loop system, these eigenvalues must not have a positive real part. For instance, in the flow-through anode configuration, eigenvalues of A in (2.11) have a negative real value ($\lambda_i|_{i=1}^{4} = -13.7, -0.2, -1.3, -2.6$). However, using the MPC, it is of interest to check the closed loop stability. Rawlings and Muske [52] have shown that the stability is guaranteed by choosing an infinite prediction horizon. Therefore, H_p is set to a sufficiently large value during the controller implementation to achieve a stable closed loop response. The state-space model of the flow-through anode in Figure 2.10, in a discrete time domain, can be rewritten as follows:

$$x(k+1) = A_d x(k) + \overbrace{\left[\begin{array}{c:c} B_d & E_d \end{array}\right]}^{B_t} \left[\begin{array}{c} u(k) \\ \hdashline w(k) \end{array}\right] \tag{3.15}$$

where matrices A, B and E are provided in [33], with A_d, B_d, and E_d as their respective matrices in a discrete time domain.

Provided that the pair (A_d, B_t) is stabilizable, any bounded input results in a bounded output response. Despite being non-measurable, the hydrogen transfer leak is assumed as a bounded input; i.e., $\dot{m}_{leak} \in \mathcal{W}$, where $\mathcal{W}$ is a bounded set. Therefore, the system remains stable for a varying but bounded HTL.

2) *Robustness*: During the control problem formulation, the effect of uncertainties was not considered; i.e., perfect state estimation was assumed ($\hat{x}(k) = x(k)$). The uncertainties can stem from the plant model mismatch as well as the unknown disturbance of HTL. In

regards to the plant model, uncertainties are related to both the linear model (identified by the parameters in Table 2.3), and the valve characteristic function. MPC uses the linear model as the internal model for the state estimation.

Provided that both the open loop and the closed loop systems are stable, norm-bounded uncertainties (which is the case in this work) cannot impair stability. To eliminate the effects of modeling error as well as HTL on the steady state response, an integral action is used. According to this, the difference between the actual output, $y(k)$, and the estimated output, $\hat{y}(k)$, is used to provide an offset-free tracking performance [37]. This would consequently affect $\Delta\mathcal{U}$ that is the solution to the optimization problem (3.6), and determines a new control input which meets the constraints. Note, that in the presence of uncertainties, the actual and estimated control inputs are not equal, i.e., $u \neq u_c$. This discrepancy is shown by e_m in Figure 3.1.
Finally, it has to be mentioned that the consistency of the identified parameters in Table 2.3 has been verified through multiple tests. Therefore, the plant model mismatch is to a large extent related to the valve characteristic function f. Defining only two operating regions for the actuator in Table 2.4, in addition to the neglected valve hysteresis, make the actuator model more prone to inaccuracies. However, it is sufficient to use Table 2.4 in this work, which will be clarified via the experimental results.

3.2.4 Control limitations

During the discussion on uncertainties, the crucial assumption was that all of the uncertainties are bounded. In this work, the uncertainty level is high if the following condition holds:

$$\left|\frac{u - u_c}{u_c}\right| > \alpha \tag{3.16}$$

where $\alpha = 15\%$ in this work. The choice of α depends on the required accuracy for the application. Either the plant modeling error or HTL could potentially result in (3.16) to hold. To overcome this, the plant model can be updated. However, if the HTL disturbance is very large, the controller would saturate and will be incapable of controlling the FOP. This is the main limitation of the controller that could impede its functionality.

This can be explained by Figure 2.10, where HTL is shown as a flow source. If this flow is large, most of the supplied flow rate ($\dot{m}_{in}$) is drained via $\dot{m}_{leak}$. Consequently, the flow rate passing through the valve is becoming so small that the valve can no longer adjust the pressure. This suggests that it might be better to also control the input flow rate $\dot{m}_{in}$. However, in this work, a testing priority was to choose a minimum number of actuators to decrease the cost. Therefore, only the BPV is utilized for FOP control. Furthermore, unlike the air flow control, this particular approach for fuel flow control is not in line with

practical applications. Fuel flow directly relates to fuel economy. Hence, compensating for large leak rates by supplying more hydrogen is not a good idea since it wastes more fuel.

This limitation can also be rectified by replacing the defected membranes with intact ones. In practice, the air flow rate is often controlled to cope with the effects of large transfer leaks which will be discussed during the experimental results. However, this cannot solve the aforementioned control issue. We have not included the air flow control in this work since our focus here is on the significance of FOP control.

3.3 Results of controller performance

This section provides the controller performance results in regulating the fuel overpressure in various anode configurations. As already mentioned, most fuel cell applications include multivariable control problems. Therefore, FOP control is usually a part of a larger control system. However, in this chapter, the focus is solely on FOP control in various PEMFC structures.

3.3.1 Flow-through anode

First, performance of the fuel overpressure control system is shown for the flow-through anode which is also discussed in [33]. Considering Figure 2.10, where the hydrogen transfer leak was also included in the model, the controller performance is evaluated during the load current change. The FOP control in the flow-through anode is achieved via an active control of the BPV. Since the valve is continuously engaged in controlling the FOP, a portion of the input hydrogen is continuously purged at the outlet. As mentioned before, the flow-through anode possesses a poor fuel economy due to this continuous purging. State-space representation of the system was expressed via (2.39) and (2.40). The control design and formulation has also been discussed in Section 3.2.

Using the 9-cell Ballard PEM fuel cell stack, the controller is experimentally evaluated. Moreover, to capture the leak effect on controller response, various membrane leak sizes have been considered where the leaky cell is placed as the middle cell in the stack. Three different leak sizes, namely, a large (L), a medium (M), and a small (S) leaky membranes are incorporated in the stack. Testing scenarios that are used for each case are depicted in Figure 3.2.

Figure 3.3 illustrates tracking performance of the FOP control system for the load variation scenarios of Figure 3.2 and various membrane leak sizes.

According to Figure 3.3 a, b, & c, the controller is able to maintain the fuel overpressure at the setpoint in spite of various hydrogen transfer leaks during the load changes. Moreover, the FOP also stays within the desired region, which for this experiment has been set to ± 1 psi ($\approx$ 6.9 kPa). The input hydrogen flow rate is chosen at a fixed rate (25 slpm) to cover all the load demands considered for these experiments. As mentioned earlier, the fuel

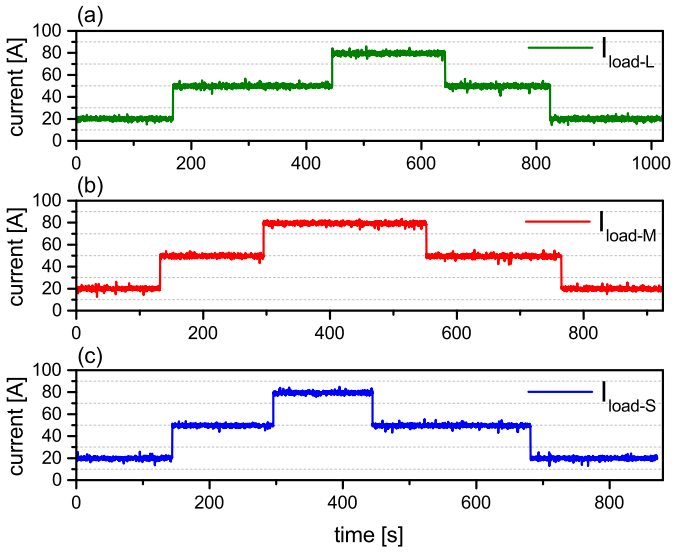

Figure 3.2: Load current variations for (a) large, (b) medium, and (c) small leaky stacks [33] (used with the permission of Elsevier)

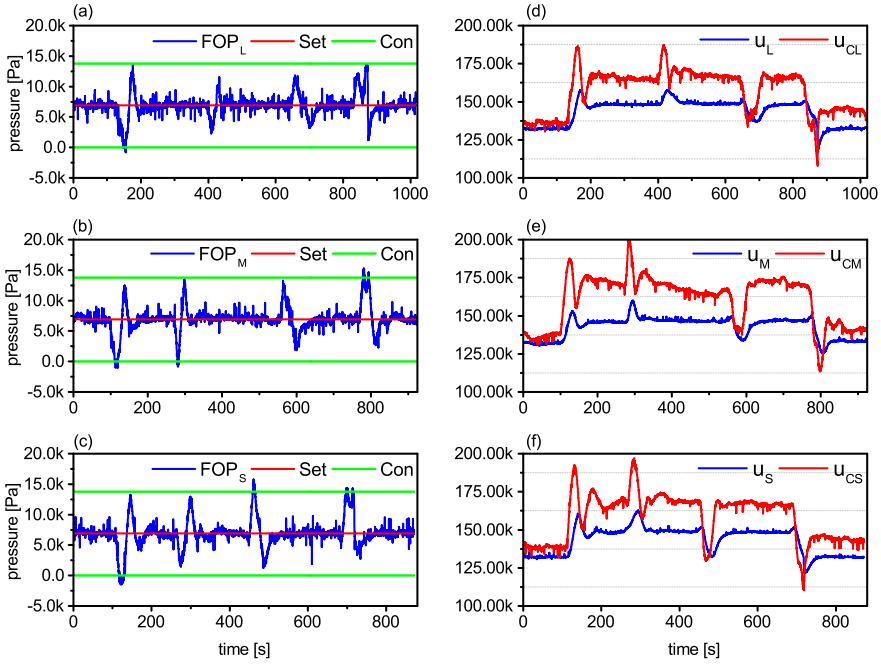

Figure 3.3: Tracking performance of the controller for: (a) large (L), (b) medium (M), and (c) small (S) leaky stacks. The control input (u_c) and the model input (u) represented in absolute pressure values for: (d) large (L), (e) medium (M), and (f) small (S) leaky stacks [33] (used with the permission of Elsevier)

overpressure setpoint has to be as low as possible. Therefore, the FOP setpoint is chosen at 1 psi. It is possible to accept even a lower setpoint. However, due to delays in system response, this could possibly result in a feasibility issue. The cathode side pressure changes first, and the anode side reacts afterward. Therefore, there exists a latency in the anode response.

In Figure 3.3 d, e, & f, both the control input u_c and the system input u, corresponding to Figure 3.3 a, b, & c, respectively, are shown which reflect the modeling error due to the sources mentioned in Section 3.2.3. In all cases, the control input u_c is higher than u (P_{out}) during both the transient and the steady-state responses. The modeling error criterion in (3.16) is approximately 8%. To reduce this gap, the plant model can be updated. However, due to the aforementioned uncertainties, some level of offset between the modeled and the actual responses are expected. In spite of this discrepancy between u and u_c, MPC retains a stable offset-free tracking response. The prediction horizon ($H_p = 30$) is chosen considerably higher than the control horizon ($H_u = 2$).

3.3.2 Dead-ended anode with periodic purging

In a dead-ended anode setup, fuel overpressure control is achieved by using the pressure control valve located upstream of the PEM fuel cell stack. The BPV is used as a purge valve in order to maintain the hydrogen concentration (HC) level in a desired region. The HC control is the subject of the next chapter. Therefore, dynamic control of the purge valve is discussed in chapter 4. Here, purging is carried out periodically. Hence, the control problem only covers the FOP regulation. This work has been detailed in [40] where here the results of controller performance are provided. The state-space model of the system is expressed via (2.20) and (2.21) where the output pressure in Figure 2.8 (pressure across the purge valve) is considered as a disturbance.

The performance of the controller in response to load dynamics, purging, and valve model uncertainty is presented for a Ballard 9-cell liquid-cooled PEMFC test station. The simulation is carried out on an experimental data set. The response of the controller is measured for a load and purge timing scenario of Figure 3.4. Notable in this figure are the three load transients. First, the rising edge occurs immediately after a purge at 48s; followed by the falling edge of the load at 279s which coincides with the purge valve opening. Lastly, the drop in the load at 407s happens right after the purge action. These events represent special cases in which the controller capability to maintain a satisfactory performance without violating the constraints is examined.

The model predictive controller is implemented using MATLAB's MPC Toolbox. The sampling time of the controller is set to 0.1s to ensure a fast enough response with respect to the fastest dynamic of the plant. The purging is performed every 30s at 7% duty cycle. Due to the high frequency of purging, it is assumed that the concentration of N_2 in both the anode and the cathode is constant. This allows for the nitrogen crossover to be modeled with

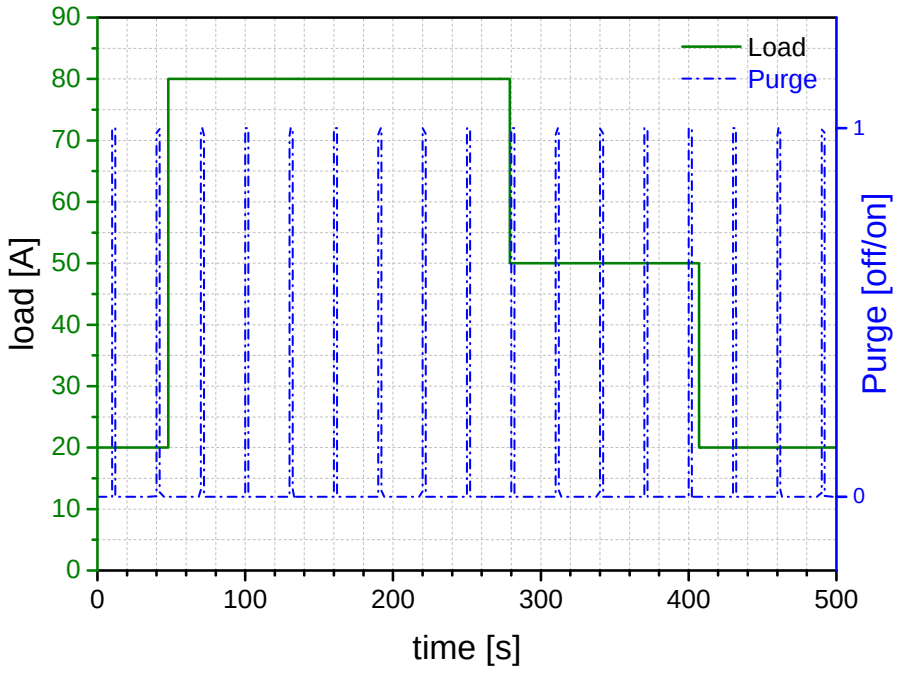

Figure 3.4: A simulation scenario indicating the load variation and periodic purging [40] (used with the permission of IEEE)

a constant. The uncertainty in the valve characteristic function is modeled as a Gaussian noise, e_m, as depicted in Figure 3.1.

The tracking performance of the controller is shown in Figure 3.5. The dashed red line in Figure 3.5(a) shows the cathode inlet pressure, and the anode inlet pressure is illustrated in the blue graph for $P_{set} = 5000$Pa. The tracking error of the controller is shown in Figure 3.5(b). For the entire simulation, the error (e) remains within the desired range of $\pm$5000Pa. From the 50s to 300s, where the load is high, the purging action causes the control input to reach the upper constraint. This is because both load and purging drop the anode pressure, and the controller is unable to sufficiently increase the control input to recover the pressure. As shown in Figure 3.6, during this period the controller becomes saturated at the maximum actuator constraint.

According to Figure 3.5(b), during the load increase, the controller has successfully compensated for the load demand. Similarly, when purging and load-decrease occur simultaneously at 279s, the controller response remains satisfactory. However, during the falling edge at 407s, there is no purging right after the transient, causing the controller to saturate at the lower constraint. As a result, the anode pressure does not decrease as fast as the cathode pressure, even with the control input at zero. With reference to the diagram of Figure 2.8, in this scenario when the purge valve is closed and the control input is zero, only the consumption decreases the anode pressure. Therefore, the system is bounded by

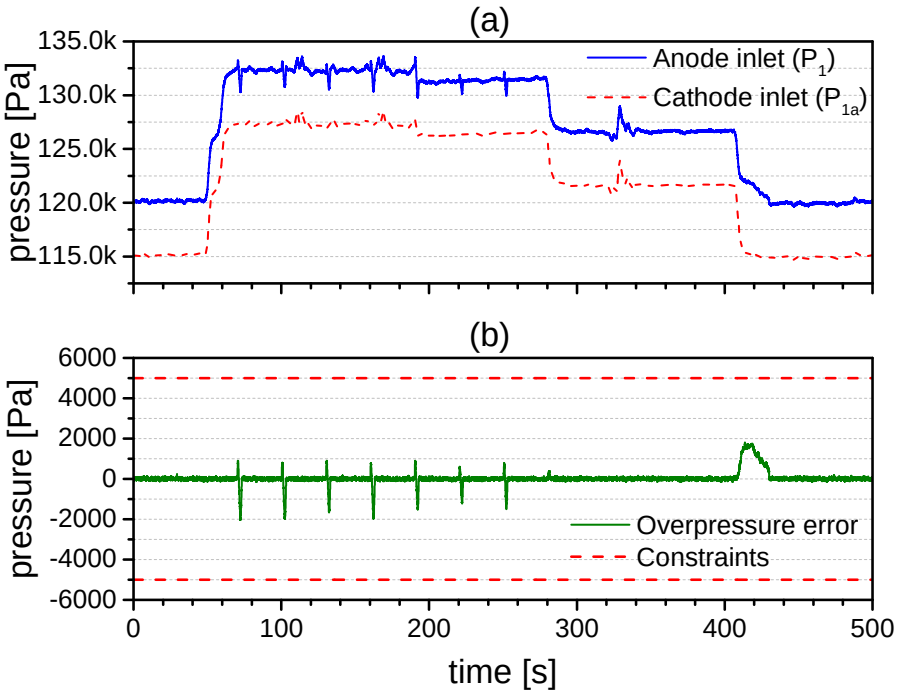

Figure 3.5: The tracking performance of the controller: (a) Pressure responses on the anode and cathode sides, (b) The tracking error and the constraints [40] (used with the permission of IEEE)

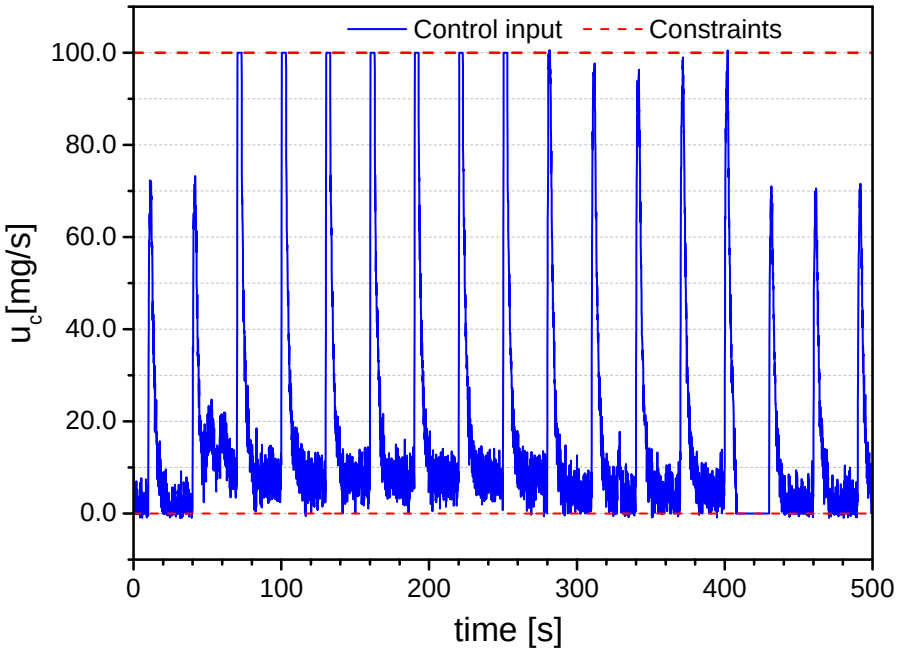

Figure 3.6: The control input command [40] (used with the permission of IEEE)

$\dot{m}_{cons}$. It is important to note that in all cases, the controller operates in the presence of valve model uncertainty.

3.3.3 Anode with recirculation with load-based purging

Fuel overpressure control in the AWR setup with load-based purging is provided in Appendix A. Besides FOP control, the hydrogen transfer leak rate is also reduced by using the HRB. Hence, a multivariable control system is utilized. Since the purge valve operates in the ON-OFF mode (with a frequency that is determined by the load), it is not among the control variables. However, HRB is utilized for reducing the leak rate. In the case that the HRB is not used as an actuator (i.e., operating at a constant voltage), the problem will only include the FOP control which is to the most extent similar to the Section 3.3.2. This multivariable control problem, that includes both FOP and leak control, is presented in detail in Appendix A. Furthermore, the multivariable control of fuel overpressure and hydrogen concentration is explained in the next chapter.

3.4 Reduction of hydrogen emission

In the presence of hydrogen transfer leaks, migration of hydrogen to the cathode would take place. This excessive hydrogen could recombine with the oxygen (air) on the cathode side and generate water. However, if the leak rate is high, this hydrogen could not only combine with all of the available oxygen, but also this oxygen starvation can then cause current-based production of hydrogen, which can also show up in the cathode exhaust. This is known as a hydrogen pumping phenomenon and should be avoided because it can lead to flammable or ignitable emissions in the cathode exhaust. Based on the experimental observations, in the case of small or medium leaky stacks, the hydrogen transfer leak was not observed to result in hydrogen emission, which is measured by a hydrogen sensor (from RKI instrument) located downstream in the cathode exhaust. However, for large leaky stacks, an H_2 emission can occur depending on the fuel overpressure level and the load current as shown in Figure 3.7. This figure shows that the lower the fuel overpressure is, the less hydrogen emission occurs. The emission is represented as the concentration of hydrogen in the cathode exhaust. In practice, aside from the FOP, the air flow could also be controlled to reduce the emission. The excess oxygen entering the stack would react with the transferred hydrogen leaks to prevent the H_2 flow to the cathode exhaust by delaying full oxygen starvation and the onset of hydrogen pumping.

3.5 Impact on the cell voltage

Various operational faults in the PEM fuel cells result in dropping of cell voltage. Figure 3.8 illustrates the effect of FOP on the cell voltage for small, medium, and large leaky cells, for

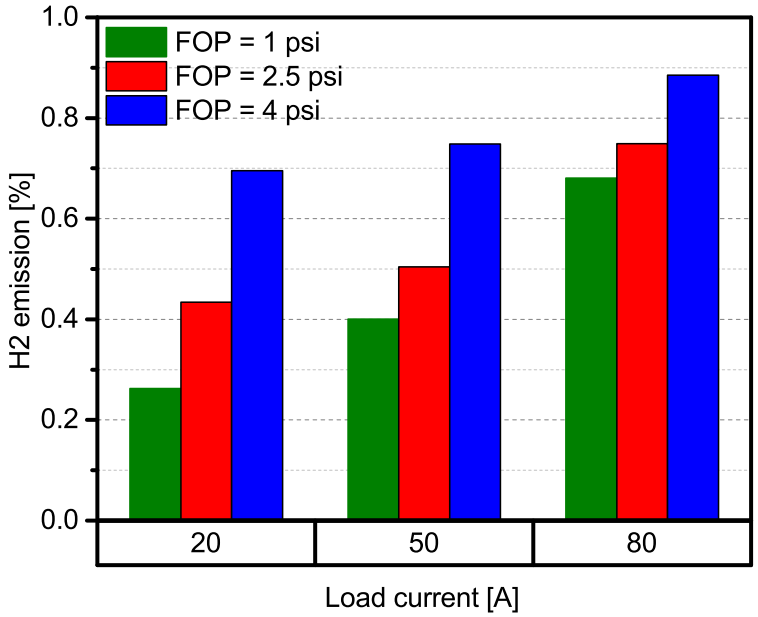

Figure 3.7: The hydrogen emission as a function of fuel overpressure and load current in a large leaky stack (cell leak $\geq$ 50 sccm for cross-pressure $\geq$ 1 psi) [33] (used with the permission of Elsevier)

a load current of 20 A. In this figure, a large span for FOP is used to increase the resolution on the cell voltage drop.

According to Figure 3.8, for the large leaky cell, the cell voltage collapses for all values of fuel overpressure which indicates that the cell is operating nearly entirely oxygen-starved. Nonetheless, the FOP still slightly affects the voltage level. This low voltage level is due to an air starvation phenomenon resulting from the excessive reaction between the HTL and the oxygen in the cell. This depletes the air side from oxygen and hence, the cell voltage drops. To recover the cell voltage, the air flow rate can be increased. In the case of the small leaky cell, the cell voltage is barely influenced by the FOP, indicating that very little hydrogen is crossing over. However, the impact of fuel overpressure on the medium leaky cell exhibits more interesting results. By increasing the FOP, the cell voltage eventually drops. The level of the voltage drop depends on the leak size, where in this test it drops around 10% for the FOP increase from 1 to 15 psi. The absence of FOP control could therefore further intensify this effect for a medium leaky cell. This will result in a severe voltage drop as seen for the large leaky cell, and consequently, require retiring the stack sooner due to low performance or emissions. This voltage drop can be explained via the Nernst equation for the cell potential [2], as follows:

$$E = E^0 + \frac{RT}{2F} ln(\frac{P_{H_2} P_{O_2}^{0.5}}{P_{H_2O}}) \tag{3.17}$$

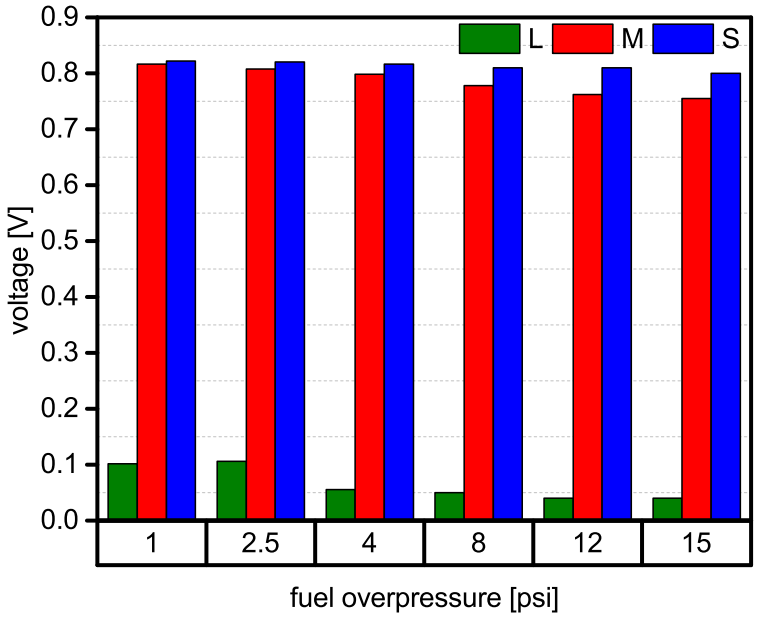

Figure 3.8: The cell voltage as a function of fuel overpressure for small, medium, and large leaky cells for $I = 20$A [33] (used with the permission of Elsevier)

In the presence of HTL, hydrogen partial pressure, P_{H_2}, drops due to the hydrogen transfer to the cathode side. Therefore, the cell potential decreases. The fuel overpressure control maintains the anode pressure at the desired level and prevents the reduction in H_2 partial pressure.

3.6 Summary

A comprehensive study of the fuel overpressure control in PEM fuel cells using the model predictive control approach was explained in this chapter. The goal was to improve both the transient and the steady-state behaviors of the FOP, which was achieved by maintaining the fuel overpressure in the desired region. The use of the MPC ensured that the FOP stayed within the limits and did not leave the desired region. Control design and limitations were discussed. Experimental results of the FOP control in the flow-through anode setup, in presence of various hydrogen transfer leaks were shown. Furthermore, the FOP control in the dead-ended anode was provided. Finally, the effect of fuel overpressure control on hydrogen emission as well as its impact on the cell voltage were discussed.

Chapter 4

Hydrogen concentration control

This chapter covers the estimation and control of the anode hydrogen concentration in PEM fuel cells. For an efficient operation of the purge valve, information about the anode H_2 content is necessary. This directly affects the fuel economy of the system. Using the outcome of the estimation algorithm, control of H_2 concentration is carried out in a multivariable control structure. Results of both the estimation method and the controller performance are also provided.

4.1 Model-based estimation of hydrogen concentration

Improving fuel economy in PEM fuel cells is crucial for cost-effective system operation. Moreover, it contributes to fuel savings considering the limited sources of hydrogen fuel. This section presents an innovative model-based approach for estimation of the anode hydrogen concentration, based on the pressure drop across the fuel cell stack. This model correlates the pressure difference to the dynamic viscosity of hydrogen-nitrogen gas mixtures. The effect of water in the estimation model is not studied here due to the usage of a condenser unit after the stack which knocks out the water from the anode. The results show the capability of the algorithm to estimate the hydrogen content with less than 3% error, in the anode side of a fuel cell test station. This station is equipped with a 9-cell Ballard bus-type fuel cell short stack, a hydrogen recirculation blower, a condenser, a pressure control valve, and a purge valve. The proposed method promises a reliable and low-cost way of monitoring the anode hydrogen concentration that can be utilized as a basis for purging.

The global necessity to transition from fossil fuels to green energy sources makes fuel cells a prime alternative [1]. However, the shortage of hydrogen availability is the main hindrance in this contention. Therefore, knowledge about the amount of available hydrogen (H_2), known as the hydrogen concentration (HC), in the fuel cell anode is vital.

Various phenomena in PEM fuel cells can alter the anode hydrogen concentration. Using air as the medium on the cathode side results in the crossover of nitrogen (N_2) to the anode

side. This is driven by the gas concentration gradient [47] which reduces the anode HC. Back-diffusion of water molecules from the cathode side can also change the anode HC, and in the case of a fuel cell with membrane pinholes, migration of hydrogen from the anode to the cathode side can further disturb the anode HC.

In this section, the detailed modeling procedure is explained. Using a pneumatic model of the system, the effect of dynamic viscosity on the FC stack pneumatic variable is studied. This effect is further investigated for different hydrogen-nitrogen gas mixtures. The estimation algorithm is then presented.

4.1.1 Use of the pneumatic model

The pneumatic model consisting of pneumatic variables such as resistors and capacitors [13] was already explained in detail in Chapter 2. A complete pneumatic model for the 3kW test station has been provided in [33]. In this section, a more in-depth view of the model is invested to simplify the understanding of the estimation method. Figure 4.1 depicts a simplified pneumatic model of the system in Figure 2.6 (the anode with recirculation configuration) using the equivalent electrical circuit, where the emphasis on this figure is on different flows entering or exiting the fuel cell anode. Q_{in} is the input flow rate to the stack. R_{fc} and C_{fc} are the pneumatic resistor and pneumatic capacitor of the FC stack, respectively [33]. Q_c is the load consumption flow rate [2].

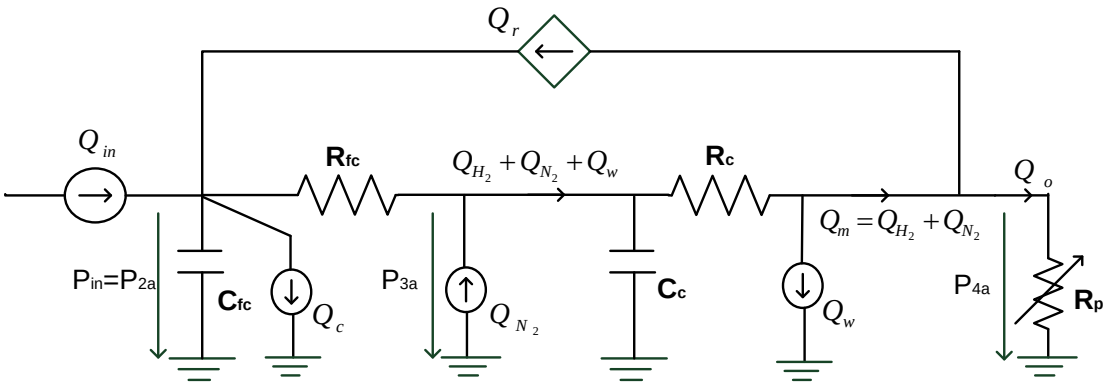

Figure 4.1: A simplified pneumatic model of the PEMFC anode using the equivalent electrical circuit

During the reaction between hydrogen and oxygen, some of the remaining nitrogen on the cathode side crosses over to the anode side due to the difference in N_2 concentration. Even in the no load condition, crossover of nitrogen would take place. The N_2 crossover flow is replaced with a flow source in Figure 4.1 (Q_{N_2}), which is located after the FC stack, and indicates the total N_2 crossover flow. In addition to nitrogen, back diffusion of water from the cathode side to the anode side causes the flow rate after the FC stack to be a

mixture of hydrogen, nitrogen, and water as shown in Figure 4.1. However, back diffusion of water is considered negligible here.

Using the condenser with pneumatic variables of R_c and C_c, would assure removal of water from the anode side. Therefore, the flow after the condenser contains only hydrogen and nitrogen. This will protect the MFM and hydrogen sensor operation from being endangered by the potential flow of liquid water. The purge valve is shown with a variable resistor since it is aimed at controlling the HC [34]. Finally, the HRB is replaced with a controllable flow source, Q_r. This is because by changing the HRB's control voltage, the pumping speed varies, and consequently, the gas flow rate inside the *anode loop* changes. In Figure 4.1, the FC stack, together with the condenser and the HRB, form a loop that is known as the *anode loop*. Comparing the model in Figure 4.1 to [14], there are a number new elements that have been added to model the AWR structure. These changes include the nitrogen crossover flow as well as the HRB model [34]. Considering a laminar flow regime, a pneumatic resistor can be described as follows:

$$R_L = \frac{\Delta P}{Q} \tag{4.1}$$

In a cylindrical pipe, (4.1) can be expressed according to the Hagen-Poiseuille equation [53] as shown here:

$$\Delta P = \frac{8\mu L}{\pi r^4} Q \tag{4.2}$$

$$R_L = \frac{8\mu L}{\pi r^4} \tag{4.3}$$

where L is the length of the pipe, μ is the dynamic viscosity, and r is the radius of the pipe. Considering (4.3), in a fixed pipe with known physical properties, the laminar resistor is a function of dynamic viscosity (μ). This result can also be applied to a fuel cell stack with fixed physical properties. Therefore, the laminar stack resistor can simply be described as follows:

$$R_L = k\mu \tag{4.4}$$

where k is assumed to be constant.

Since dynamic viscosity is dependent on the gas type as well as the gas mixture, it can be used to study the effect of different gases on the stack resistor.

4.1.2 Dynamic viscosity

The resistance of a fluid to shearing flows is described as dynamic viscosity [54]. μ for ideal gases can be expressed as a function of temperature via Sutherland's formula [55] as stated

in (4.5):

$$\mu = \mu_0 \frac{T_0 + C}{T + C} (\frac{T}{T_0})^{1.5} \tag{4.5}$$

where μ_0 is the reference viscosity at the reference temperature T_0, and C is Sutherland's constant. In this work, the temperature variation is considered negligible. Therefore, the temperature is assumed constant. Table 4.1 shows the values of C and μ_0 for the reference temperature of T_0 and selected gasses.

Table 4.1: The reference values of C, T_0, and μ_0 for selected gasses

Gas	C [K]	T_0 [K]	μ_0 [μPa.s]
N_2	111	300.55	17.81
H_2	72	293.85	8.76
air	120	291.15	18.27
O_2	127	292.25	20.18

The FC stack on the anode side contains a mixture of hydrogen and nitrogen. In the anode with recirculation structure, the accumulation of nitrogen on the anode side could significantly affect the performance. Therefore, to study the N_2 effect on the stack resistor, the dynamic viscosity of the anode gas mixtures is considered.

The equation for the gas mixture dynamic viscosity, provided in [56], is described as follows:

$$\mu_m = \sum_{i=1}^{n} \frac{\mu_i}{1 + \frac{1}{x_i} \sum\limits_{\substack{j=1 \\ j \neq i}}^{j=n} x_j \phi_{ij}} \tag{4.6}$$

where ϕ_{ij} is:

$$\phi_{ij} = \frac{[1 + (\mu_i/\mu_j)^{\frac{1}{2}} (M_j/M_i)^{\frac{1}{4}}]^2}{(4/\sqrt{2})[1 + (M_i/M_j)]^{\frac{1}{2}}} \tag{4.7}$$

In the above equations, M is the gas molecular weight, x is the mole fraction of a component in the mixture, and μ is the dynamic viscosity. With this introduction on the system pneumatic model as well as the gas mixture dynamic viscosity, we can proceed with the concentration estimation algorithm in the next part.

4.1.3 Model-based HC estimation method

As shown in Figure 4.1, the gas flow passing through the FC stack anode includes hydrogen, nitrogen, and water. As already mentioned, the effect of water is negligible. Therefore,

considering the mixture of H_2-N_2 and the dynamic viscosity of the gas mixture, the stack pneumatic resistor can be expressed as follows:

$$R_L(x_h, x_n) = k\mu(x_h, x_n) \tag{4.8}$$

where x_h and x_n are the mole fractions of hydrogen and nitrogen in the H_2-N_2 mixture, respectively. The mole fraction can be described in terms of flow rate. Assuming ideal gasses, the following equations can be written:

$$P_h V_h = x_h R T_h \tag{4.9}$$

$$P_n V_n = x_n R T_n \tag{4.10}$$

where R is the universal gas constant, P is the gas pressure, V is the gas volume, and T is the temperature. In the anode, pressure and temperature are the same for both H_2 and N_2. Therefore,

$$\frac{V_h}{V_n} = \frac{x_h}{x_n} \tag{4.11}$$

$$\frac{V_h/\Delta t}{V_n/\Delta t} = \frac{x_h}{x_n} \tag{4.12}$$

$$\frac{Q_h}{Q_n} = \frac{x_h}{x_n} \tag{4.13}$$

where Q_h and Q_n are the volumetric flow rate of hydrogen and nitrogen, respectively. In this chapter, all flow rates are considered volumetrically. The MFM placed after the condenser in Figure 2.6, is used to measure the gas mixture flow rate.

The flowchart shown in Figure 4.2 depicts the model-based algorithm for finding the HC. This algorithm utilizes the pressure drop across the anode, the gas mixture dynamic viscosity, the MFM measurement (or the HRB characterization), and the FC stack constant k to derive the HC.

Considering Figure 4.2, the hydrogen concentration is obtained as follows:

$$(x_h, x_n) = G(\mu_m, T) = G(\frac{\Delta P_m}{kQ_m}, T) \tag{4.14}$$

where ΔP_m is the measured pressure drop across the anode, T is the gas mixture temperature, and Q_m is the MFM flow rate. G is the inverse function of (4.6) which outputs x_h and x_n in an H_2-N_2 mixture using μ_m and T.

When x_h falls below $x_{h(min)}$, the purging decision unit will activate the purge valve to regulate the HC back to the desired region that is between $x_{h(min)}$ and 100%. $x_{h(min)}$ is the minimum acceptable level of anode HC. Discussion on details of purge valve control is

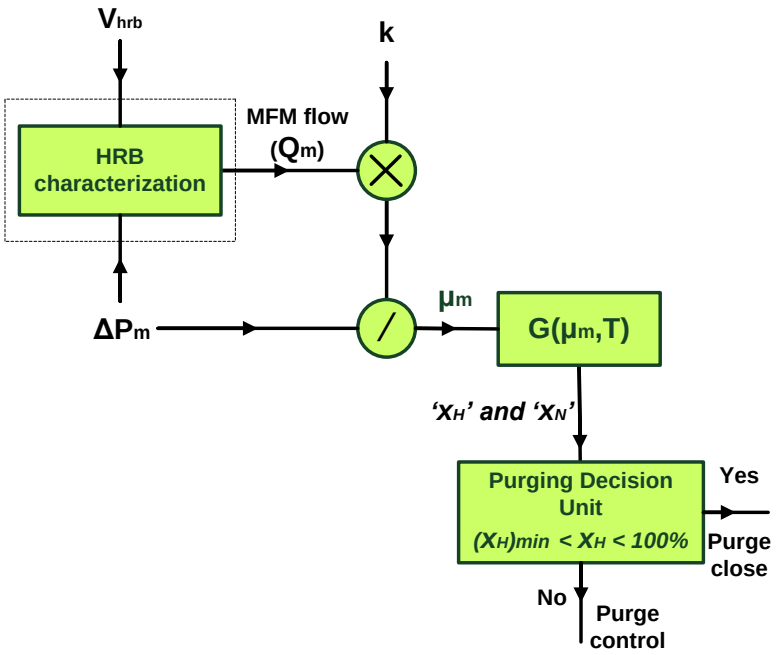

Figure 4.2: Flowchart of the estimation algorithm for deriving the H_2 concentration

not within the scope of this work, but this can either be a fixed orifice valve with time-open control, or a more sophisticated approach using a proportional control valve for purging.

Considering the estimation algorithm, one key parameter to derive is k in (4.8) which theoretically should be constant for a fuel cell stack with fixed physical properties. This parameter is obtained experimentally in the next section. The HC estimation algorithm in Figure 4.2 suggests the use of pressure drop across the anode for evaluating the HC.

To apply this method in real world FC applications, it is necessary to employ the HRB characterization for obtaining the gas flow rate in the *anode loop* as highlighted in Figure 4.2. In most FC products, due to the presence of liquid water in the anode, mass flow meters are not used to measure recirculation flow, where the actual HRB characterization data would typically be used instead. This characterization will be discussed in the next section.

4.1.4 Results

To apply the HC estimation method introduced in Section 4.1.3, first the parameter k in equation (4.8) should be derived. Secondly, the HC model-based algorithm should be verified. The effects of various operating conditions, such as the load demand, also need to be investigated. To tackle these objectives, a fixed HRB voltage is used, where this is in line with current practices where the HRB control voltage is often maintained constant. At the end of this section, the HRB characterization is explained, which can eliminate the usage of the MFM for *anode loop* flow measurement.

To capture the nitrogen buildup on the anode side, the system in Figure 2.6 should operate with a closed purge valve. Hence, no periodic or dynamic purging is enforced. The purpose of purging is to maintain the HC above a certain level. However, the aim of this work is to observe the effect of N_2 crossover and to estimate the HC. This is done in practice by letting the anode concentration change over time without purging to replenish the loop. The inlet pressure of the anode is controlled via the pressure control valve in Figure 2.6.

1. **Deriving** k: To obtain k, the pressure drop across the anode in Figure 2.6 is measured while the MFM reads the anode flow rate. Moreover, the hydrogen sensor is utilized to derive the HC and to calculate the dynamic viscosity of the anode gas mixture. Considering (4.1) and (4.4), k is obtained as follows:

$$k = \frac{\Delta P}{\mu_m Q} = \frac{P_{a2} - P_{a3}}{\mu_m Q_m} \tag{4.15}$$

where μ_m is the gas mixture viscosity expressed in (4.6), P_{a2} and P_{a3} are the inlet and outlet pressures of the FC stack anode, respectively, and Q_m is the measured flow rate by the MFM.

Figure 4.3 illustrates the variation of k observed during an experiment where the purge valve is closed (as already explained), the load current is set to 125 A, and the inlet pressure of the stack is adjusted at 10 psi. This is chosen as a sample scenario for obtaining k.

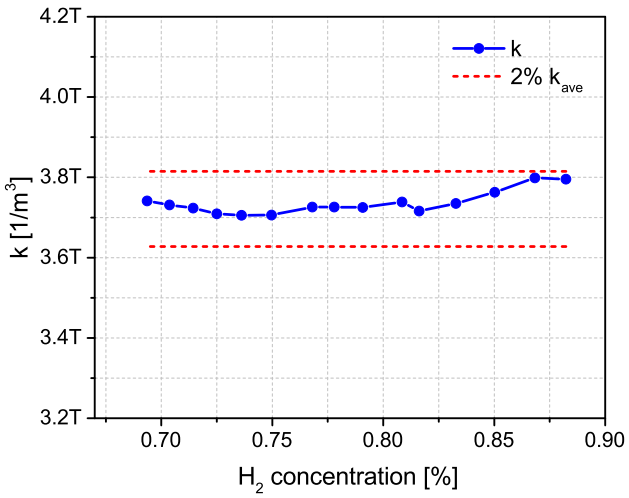

Figure 4.3: Parameter k for various H_2 concentrations at T = 65 C, P_{in} = 10 psi, and I = 125 A

As shown in Figure 4.3, k is remaining well within 2% of the k_{avg} which is the average k value for various concentrations. As is expected, k can be considered constant at

3.7×10^{12} (k_{avg}). The variation in k could stem from the accuracy of measurement devices such as the MFM.

2. **Verification of the model-based method**: To verify the model-based HC estimation algorithm, the purge valve is closed, and the HRB control voltage is fixed. Using the pressure drop across the anode, the H_2 concentration is estimated (HC_{est}) following the flowchart of Figure 4.2. The calculated HC is then compared with the H_2 sensor output (HC_m) to evaluate the estimation accuracy.

   The verification results are shown in Figure 4.4 for a scenario where the load current, I, is set to 160 A, the inlet pressure of the FC stack anode, P_{in}, is regulated at 12 psi, and the HRB control voltage, V_{hrb}, is set at 2.5 V.

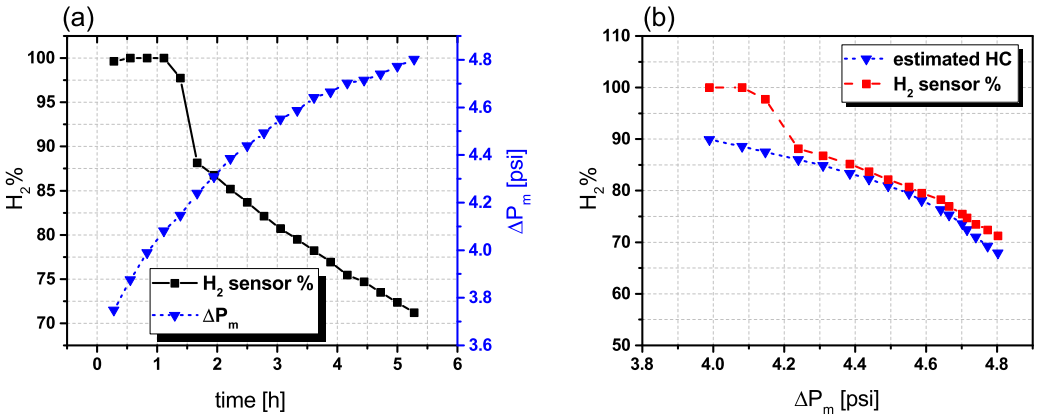

Figure 4.4: Verification results at $V_{hrb} = 2.5$ V, $I = 160$ A, and $P_{in} = 12$ psi at T = 65 C: (a) H_2 sensor output and the measured pressure drop ΔP_m, (b) HC estimation HC_{est} versus HC measurement (HC_m)

Figure 4.4(a) illustrates the measured pressure drop, ΔP_m, across the FC stack anode as well as the H_2 sensor output as the test progresses without purging over time. Considering the operating conditions, experimental setup, and the membrane properties in this test, a 30% drop in H_2 concentration is observed to occur over approximately 5 hours, where this primarily occurs because the size of components used in this testing, such as the condenser, is considerably larger compared to the anode loop volumes in FC modules used in products. Therefore, the effect of nitrogen crossover is observed at a much lower pace in these tests than in products.

As shown in Figure 4.4(a), the Neodym H_2 sensor is incapable of distinguishing the HC above 90%, which is a limitation of the sensor. Therefore, verifying the HC estimation method for very high H_2 concentrations is challenging. However, the pressure drop in that region displays a noticeable change. In most fuel cell applications, the H_2 concentration is maintained over 70%.

In Figure 4.4(b), the verification result is shown where HC_{est} exhibits over $\sim$ 97% matching with the measured HC for $HC_m < 90\%$ H_2. As mentioned, the verification of the algorithm for $HC_m > 90\%$ is not possible due to the H_2 sensor's limitation. However, the model-based method can detect changes in the H_2 content above 90%.

3. **Effect of load current and pressure**: To evaluate the performance of the HC estimation algorithm, it is necessary to examine it during various operating conditions. Among the most important conditions, are changes in I and P_{in} which frequently occur in various FC applications. Considering Figure 4.1, with a closed purge valve ($Q_o = 0$), and neglecting Q_w, a significant portion of the input flow rate is consumed by the load, i.e., $Q_{in} \approx Q_c$, and the remaining hydrogen circulates in the *anode loop* where $Q_m = Q_r$. Therefore, the variation of the load current will affect the *anode loop* flow rate and consequently, it impacts the pressure drop across the anode. This is shown in Figure 4.5(a) where ΔP_m for $V_{hrb} = 2.5$ V and $P_{in} = 12$ psi, is compared for two different load currents, where increasing the load current raises the pressure drop. However, the estimation algorithm remains within $\sim$ 97% matching with the measured H_2 concentration for $HC_m < 90\%$ H_2, as depicted in Figure 4.5(b).

   Figure 4.5(c) & 4.5(d) show the impact of P_{in} on the algorithm performance with $V_{hrb} = 2.5$ V and $I = 160$ A, for two different anode inlet pressures. Since P_{in} is adjusted based on the fuel overpressure, it can vary during operation depending on the pressure at the cathode inlet of the FC stack [33]. ΔP_m is only changing slightly while the estimation algorithm is in agreement with the HC measurement within $\sim$ 98% matching for $HC_m < 90\%$ H_2.

   Therefore, the model-based algorithm is capable of estimating the H_2 concentration in the anode over different operating conditions with less than 3% error over the ranges that we are most interested in (between $\sim$ 70 to 90% H_2).

4. **HRB characterization**: Earlier in Table 2.1, the rotational speed of the HRB pump for some selected control voltages was shown. In general, the HRB characterization is a function of the pressure difference across the HRB (ΔP_{hrb}) and the control voltage of the HRB(V_{hrb}) as follows:

$$Q_r = F(V_{hrb}, \Delta P_{hrb}) \tag{4.16}$$

   where V_{hrb} in (4.15) can be replaced by the rotational speed of the pump, ω_{hrb}. Moreover, V_{hrb} is considered equivalent to ΔP_m by neglecting the pressure drop across the condenser, which is minuscule.

   By considering Figure 4.1, when the purge valve is closed ($Q_o = 0$), the HRB flow rate is directly obtained via the MFM ($Q_r = Q_m$). Therefore, the HRB characterization can be done by changing V_{hrb} and ΔP_{hrb} while the purge valve is closed. However,

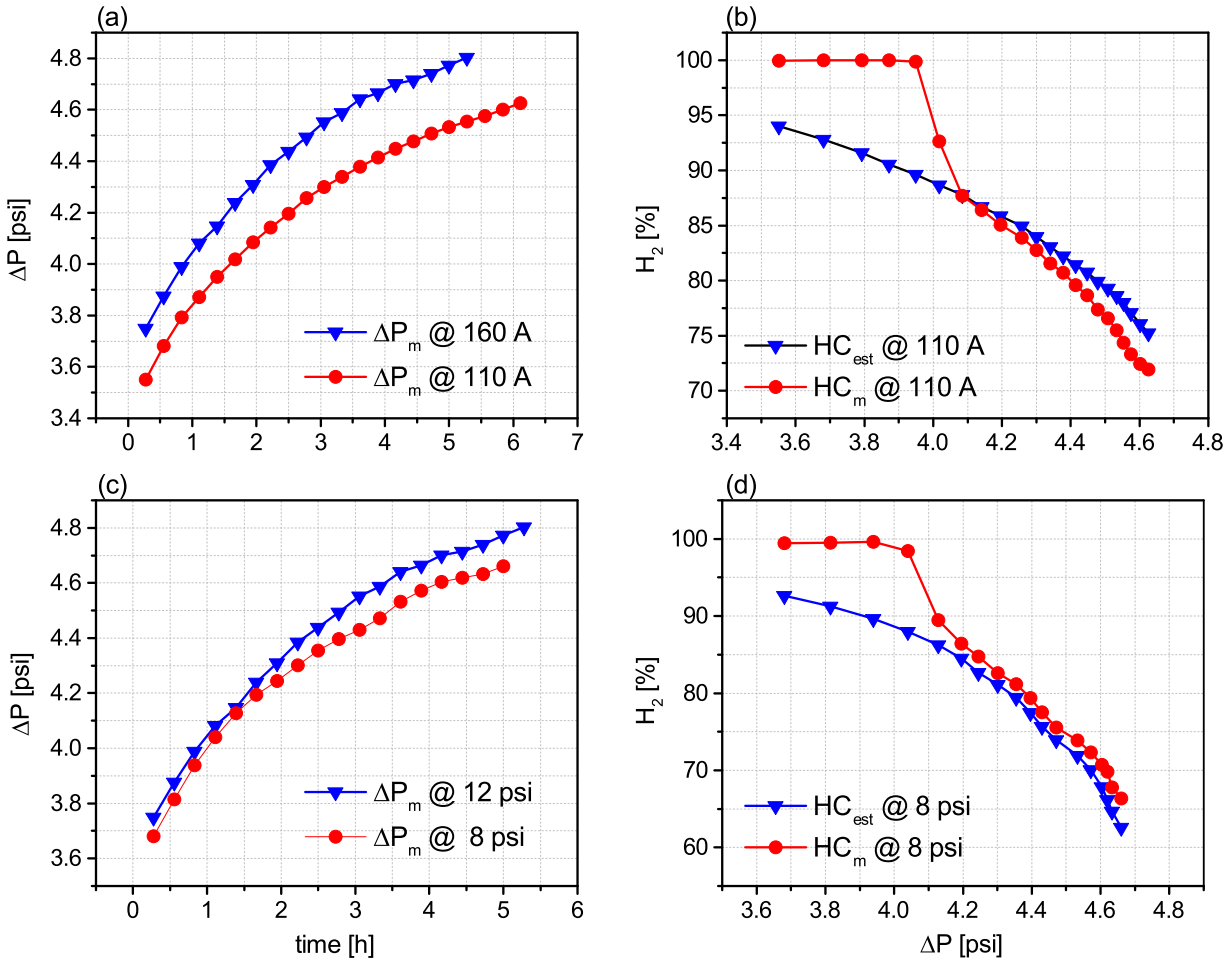

Figure 4.5: Effect of the operating conditions on estimation model performance at T = 65 C: (a) Comparison of ΔP_m for I = 110 and 160 A, P_{in} = 12, and V_{hrb} = 2.5 V (b) The verification of the estimation model for I = 110 and 160 A, P_{in} = 12, and V_{hrb} = 2.5 V, (c) The comparison of ΔP_m for P_{in} = 8 and 12 psi, I = 160 A, and V_{hrb} = 2.5 V, (d) The verification of the estimation model for for P_{in} = 8 and 12 psi, I = 160 A, and V_{hrb} = 2.5 V

changing ΔP_{hrb} is not a trivial task. The source of the pressure drop variation across the HRB is the addition of nitrogen flow which enters the anode side. Therefore, to characterize the HRB, the system in Figure 2.6 operates at different testing scenarios that are depicted in Figure 4.6 for three cases.

The control voltage is chosen at 2.5 V and 3.5 V. As can be seen, the change in V_{hrb} changes the ΔP_m-Q_m curve. In addition, Figure 4.6 illustrates that for a fixed V_{hrb}(2.5 V), Q_m is a function of ΔP_m. Hence, it confirms that the HRB characterization can be presented by equation (4.16). Therefore, it is possible to derive the *anode loop* flow in Figure 4.2 by employing the HRB characterization without using the MFM.

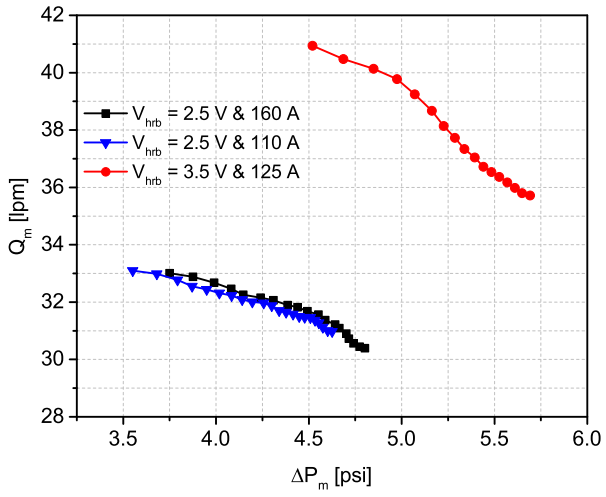

Figure 4.6: The HRB characterization at $V_{hrb} = 2.5$ V and I = 110 and 160 A as well as $V_{hrb} = 3.5$ V and I = 125 A

In practice, the HRB control voltage is chosen depending on the stack size or the maximum load current, which is usually fixed.

4.2 Multivariable control design

Employing the proposed estimation method, the purge valve can be dynamically controlled to maintain the hydrogen concentration at the desired level. A model-based controller design is explained here. Considering Figure 4.1 (or equivalently Figure 2.9), governing equations on the system were provided via (2.22-2.24). In Chapter 2, using nonlinear transformations, a linear state-space model was derived. However, based upon the work in [34], the nonlinear state-space model here is linearized around each operating condition (without using those nonlinear transformation expressed in (2.25) and (2.26)). Using (2.24 - 2.26), the equations explaining the system dynamics can be written as below:

$$\begin{cases} C_{fc}\dot{x_1} = (\dfrac{-1}{u_1} - \dfrac{1}{R_{fc}})x_1 + \dfrac{1}{R_{fc}}x_2 + \dfrac{1}{u_1}w_1 + w_2 - w_3 \\ C_c\dot{x_2} = \dfrac{x_1}{R_{fc}} - (\dfrac{R_c + R_{fc}}{R_c R_{fc}})x_2 + \dfrac{(x_2 - R_c w_2)u_2}{R_c(R_c + u_2)} + w_4 \end{cases} \tag{4.17}$$

where the vectors $x(t)$, $u(t)$ and $w(t)$ are provided in (4.18) in the following:

$$\begin{cases} x(t) = \begin{bmatrix} x_1(t) \\ x_2(t) \end{bmatrix} = \begin{bmatrix} P_1(t) \\ P_2(t) \end{bmatrix} = y(t) \\ \\ u(t) = \begin{bmatrix} u_1(t) \\ u_2(t) \end{bmatrix} = \begin{bmatrix} R_{v_1} \\ R_{v_2} \end{bmatrix} \\ \\ w(t) = \begin{bmatrix} w_1(t) \\ w_2(t) \\ w_3(t) \\ w_4(t) \end{bmatrix} = \begin{bmatrix} P_{in}(t) \\ \dot{m}_r(t) \\ \dot{m}_{cons}(t) \\ \dot{m}_{N_2}(t) \end{bmatrix} \end{cases} \tag{4.18}$$

Having (x_0, u_0) as the equilibrium point the linearized state-space model is obtained via the equations below:

$$\begin{cases} \tilde{x}(t) = x(t) - x_0 \\ \tilde{u}(t) = u(t) - u_0 \end{cases} \tag{4.19}$$

$$\dot{\tilde{x}}(t) = \left.\frac{\partial f}{\partial x}\right|_{(x_0,u_0)} \tilde{x}(t) + \left.\frac{\partial f}{\partial u}\right|_{(x_0,u_0)} \tilde{u}(t) \tag{4.20}$$

where $f = dx/dt$ and

$$\begin{aligned} \tilde{x}(t) &= [\tilde{x}_1(t), \tilde{x}_2(t)]^T \\ \tilde{u}(t) &= [\tilde{u}_1(t), \tilde{u}_2(t), \tilde{w}_1(t), \tilde{w}_2(t), \tilde{w}_3(t), \tilde{w}_4(t)]^T \end{aligned} \tag{4.21}$$

As can be seen, the control input vector is lumped in with the disturbance vector. The general formulation of the linearized model in [42] is also applied here for both the continuous and the discrete time domains.

The aim with the controller design is to achieve the problem objectives as follows:

- To maintain the hydrogen concentration in the desired level.
- To control the fuel overpressure, such that the stack inlet pressure on the anode side stays slightly above the stack inlet pressure on the cathode side.

The estimation method has a limitation at very high (over 90%) H_2 concentrations. However, the pressure drop curve in Figure 4.4(a) was still capable of distinguishing between 100% and 90% HCs. The validation was not possible due to H_2 sensor limit. Using the

pressure drop curve of Figure 4.4(a), it is feasible to define a setpoint for the outlet pressure of the PEMFC stack, knowing the inlet pressure. Therefore, following setpoints are defined:

$$y_{1d} = P_{air} + P_{set} \tag{4.22}$$

$$y_{2d} = y_{1d} - R_{fc(100\%H_2)} \times \dot{m}_{r(100\%H_2)} \tag{4.23}$$

where $0 \leq P_{set} \leq 10^4$ (Pa). By defining the setpoint for y_1 and utilizing Figure 4.4(a), a setpoint for the stack outlet pressure, y_2, can be determined as provided in (4.23).

Equation (4.23) introduces a novel approach for controlling the H_2 concentration by defining a setpoint that results in a steady H_2 concentration at a designated level. To explain more about (4.23), it is helpful to consider Figure 2.9 at the steady state with a fully closed purge valve. In this case, the input flow rate ($\dot{m}_{in}$) will be equal to the consumption flow rate ($\dot{m}_{cons}$) while the recirculation flow rate ($\dot{m}_r$) will be passing through the anode. This is a reasonable setpoint since by slightly opening the purge valve, the nitrogen will leave the stack and pure hydrogen flows through again.

The constraints of the problem include the actuator limitation on both the range and the rate of change as well as the output constraints as summarized in equations (4.25 - 4.28) (for simplicity of the notation the sampling time T_s is assumed to be 1). Note that the same constraints apply to both valves.

$$\tilde{x}(k+i+1|k) = \hat{A}\tilde{x}(k+i|k) + \hat{B}\tilde{u}(k+i|k) \tag{4.24}$$

$$u_{min} \leq \tilde{u}(k+i|k) \leq u_{max} \tag{4.25}$$

$$\delta u_{min} \leq \delta\tilde{u}(k+i|k) \leq \delta u_{max} \tag{4.26}$$

$$y_{1d} - \gamma_{min} \leq \tilde{y}_1(k+i|k) \leq y_{1d} + \gamma_{max} \tag{4.27}$$

$$y_{2d} - \beta_{min} \leq \tilde{y}_2(k+i|k) \leq y_{2d} + \beta_{max} \tag{4.28}$$

where $i = H_w, \cdots, H_p$. u_{min} and u_{max} are the boundaries on the actuator range. δu_{min} and δu_{max} are the limits on the rate of change of the actuator. γ_{min}, γ_{max}, β_{min} and β_{max} are the limits on the maximum allowed deviation from the desired trajectory for outputs.

4.3 Results

To evaluate the proposed algorithm, the MATLAB Model Predictive Control Toolbox is used for a simulation scenario that covers variations in both the load current and the nitrogen crossover flow rate. In fact, as stated in the model in (4.18), the N_2 crossover is a disturbance. The model has to be linearized around each operating condition. However, the linear model around each point is valid for $\Delta I \approx \pm 20A$. Therefore, the model, as well as

the controller parameters, need to be updated. The operating condition is defined based on load current and hydrogen concentration which in this simulation study should stay around 100%. For the simulation, experimental data is used for the air side to help to determine the anode pressure setpoint according to (4.22). Figure 4.7 illustrates the simulation scenario.

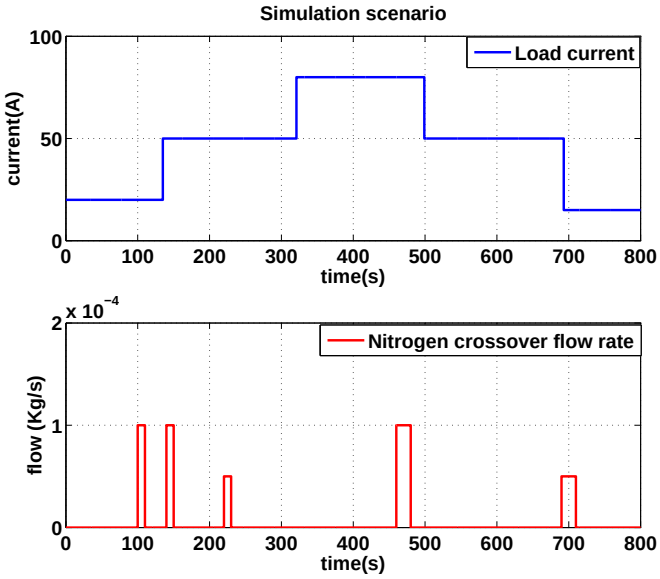

Figure 4.7: The simulation scenario: (Top) Load current, (Bottom) Nitrogen crossover flow rate [34] (used with the permission of IEEE)

As can be seen, the variation in N_2 crossover flow has been considered both when the load is fixed and when the load is varying. The anode outlet pressure is an indicator of hydrogen concentration. This, as well as the fuel overpressure, are the controlled variables. Figure 4.8 shows the tracking performance of the controller.

Considering the simulation scenario, the controller reacts quickly without violating the constraints. The output constraints allow the deviation of ± 5000 (Pa) around the desired trajectory, which is the case in Figure 4.8. The fuel overpressure setpoint (P_{set}) used in deriving the tracking error was 5000 (Pa) while for the anode outlet pressure equation (4.23) was used. Nevertheless, the output error has to reach zero. As illustrated in Figure 4.8, the FOP stays within the specified range with $|\gamma_{min}| = |\gamma_{max}| = |\beta_{min}| = |\beta_{max}| = 5000\ (Pa)$. Lastly, Figure 4.9 depicts the changes in the control input commands.

Because in the beginning of the simulation, the model was linearized around $20A$ and 100% H_2 concentration, the control inputs ($\tilde{u}$) are initially at rest. Figure 4.9 shows the features of the multivariable control. The pressure control valve is primarily regulating the fuel overpressure during the load change. However, it also reacts during N_2 crossover and controls the fuel overpressure. The purge valve is largely responsible for controlling the anode outlet pressure during N_2 crossover while it also reacts during the load change. With

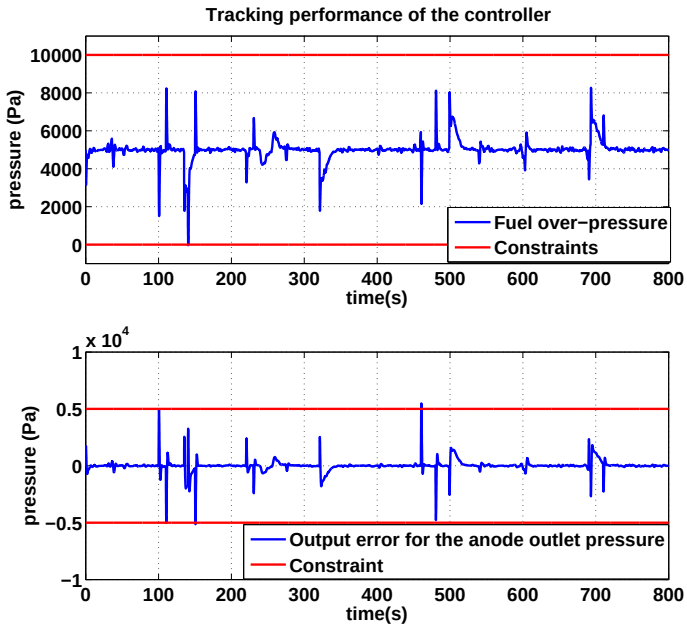

Figure 4.8: Controller tracking performance: (Top) Fuel overpressure, (Bottom) Variation in anode outlet pressure for 100% H_2 [34] (used with the permission of IEEE)

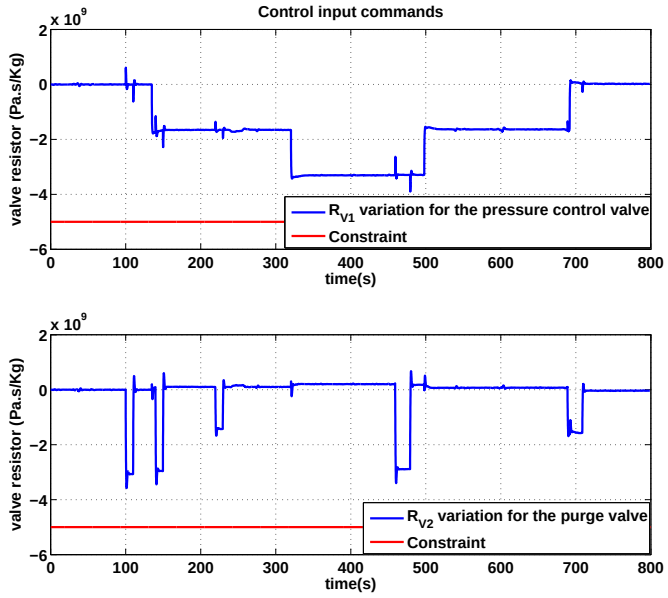

Figure 4.9: Controller input command: (Top) Pressure control valve resistor variation, (Bottom) Purge valve resistor variation [34] (used with the permission of IEEE)

the load current increase from 20 to 50 A, the model had to be updated. In Figure 4.9, both

control inputs comply with the constraints on the actuators where only the low constraint is shown for this simulation scenario.

4.4 Summary

A novel technique for estimation of the hydrogen concentration on the anode side of the PEM fuel cell was presented. The model-based estimation approach utilized the pneumatic model of the anode as well as the pressure drop measurement across the stack, and correlated the hydrogen content to the dynamic viscosity of the anode gas mixture. Employing a condenser, the water on the anode side was removed after the stack. As a result, the dry anode gas mixture included hydrogen and nitrogen only. To use the estimation algorithm in fuel cell products, the HRB characterization was incorporated in the model. The results of experimental validation of the algorithm were provided in various operating conditions. Lastly, the multivariable control design based on the proposed estimation algorithm was explained which aimed at improving the fuel economy.

Chapter 5

Conclusions

Modeling and control of the fuel supply system in three major anode configurations were explained in detail in this work. System modeling was carried out using the pneumatic modeling technique. Both fuel overpressure control and hydrogen concentration control were discussed where the MPC approach was utilized to achieve the control objectives. The following highlights summarize the benefits of this study which were explained in the previous chapters.

5.1 Improved system performance by enhanced fuel overpressure control

By maintaining the fuel overpressure in the desired region, while having an intact membrane, the exertion of excessive pressure across the membrane could be prevented. Moreover, while having a membrane with pinholes, the transfer of reactants to the opposite side would be minimized. Hence, fuel overpressure control could avoid fuel starvation and membrane damage. Fuel overpressure was actively controlled near zero with a limited deviation. The Model predictive approach ensured that the boundaries on the control input and the outputs were respected. As as result, the FOP stayed within the desired region in the presence of various hydrogen transfer leaks. Furthermore, the FOP control reduced the hydrogen emission and prevented the collapse in the cell voltage when the transfer leaks were not large.

5.2 Model-based estimation of hydrogen concentration

The hydrogen concentration on the anode side after the stack was estimated by a model-based algorithm which practically used the pressure drop measurement across the stack as well as the HRB characterization. This pressure drop was correlated to the dynamic

viscosity of gas mixtures. The estimation algorithm was validated in various operating conditions which exhibited less than a 3% estimation error.

5.3 Hydrogen concentration control to improve fuel economy

By utilizing the proposed estimation algorithm, a multivariable control system was developed which controls the HC as well as the FOP. Controlling the hydrogen concentration could ultimately limit the amount of fuel purged at the anode outlet in order to save more hydrogen.

5.4 Future works

Future works include the implementation of the multivariable control system for the HC and the FOP control in the AWR structure, using the H_2 estimation method, in the presence of hydrogen transfer leaks. Furthermore, a comparative study can be conducted to evaluate the fuel savings of the current-based purging strategy, with the model-based multivariable control system that uses the proposed estimation algorithm, as the basis of purging.

List of Publications

1. A. Ebadighajari, J. DeVaal, F. Golnaraghi, “Optimal control of fuel overpressure in a polymer electrolyte membrane fuel cell with hydrogen transfer leak during load change,” Journal of Power Sources 340 (2017), 247-257

2. A. Ebadighajari, H. Homayouni, J. DeVaal, F. Golnaraghi, “Model-based estimation of hydrogen concentration in a polymer electrolyte membrane fuel cell,” Submitted to the Journal of Power Sources

3. A. Ebadighajari, H. Homayouni, J. DeVaal, F. Golnaraghi, “Model predictive control of polymer electrolyte membrane fuel cell with dead-end anode and periodic purging,” 2016 IEEE Conference on Control Applications (CCA), Buenos Aires, Argentina, pp. 1500-1505

4. A. Ebadighajari, J. DeVaal, F. Golnaraghi, "Multivariable control of hydrogen concentration and fuel over-pressure in a polymer electrolyte membrane fuel cell with anode re-circulation," 2016 American Control Conference (ACC), Boston, MA, 2016, pp. 4428-4433

5. A. Ebadighajari, J. DeVaal, F. Golnaraghi, "Optimal control of fuel over-pressure in a polymer electrolyte membrane fuel cell system during load change," 2015 American Control Conference (ACC), Chicago, IL, 2015, pp. 3236-3241

6. A. Ebadighajari, J. DeVaal, F. Golnaraghi, "Reduction of hydrogen transfer by constrained control of anode hydrogen recirculation in a polymer electrolyte membrane fuel cell with anode re-circulation," submitted to the 2017 IEEE Control and Decision Conference (CDC), Melbourne, Australia, Dec 12-15, 2017

Bibliography

[1] Fuel Cell Handbook. EG&G Technical Services, inc. *US Department of Energy, 2004*, 2004.

[2] James Larminie, Andrew Dicks, and Maurice S McDonald. *Fuel cell systems explained*. Wiley New York, 2003.

[3] Cristian Kunusch, Paul Puleston, and Miguel Mayosky. *Sliding-Mode control of PEM fuel cells*. Springer Science & Business Media, 2012.

[4] Felix Grasser and Alfred Rufer. A fully analytical PEM fuel cell system model for control applications. *IEEE transactions on industry applications*, 43(6):1499–1506, 2007.

[5] Noriko Hikosaka Behling. *Fuel cells: current technology challenges and future research needs*. Newnes, 2012.

[6] U S Department of Energy DOE. 2011 Fuel cell technologies market report. (July):69, 2012.

[7] Matthew M Mench. *Fuel cell engines*. John Wiley & Sons, 2008.

[8] John H Scott. The development of fuel cell technology for electric power generation: From nasa's manned space program to the "hydrogen economy". *Proceedings of the IEEE*, 94(10):1815–1825, 2006.

[9] John C Amphlett, Rob M Baumert, Ronald F Mann, Brant A Peppley, Pierre R Roberge, and Thomas J Harris. Performance modeling of the ballard mark iv solid polymer electrolyte fuel cell i. mechanistic model development. *Journal of the Electrochemical Society*, 142(1):1–8, 1995.

[10] John C Amphlett, RM Baumert, Ronald F Mann, Brant A Peppley, Pierre R Roberge, and Thomas J Harris. Performance modeling of the ballard mark iv solid polymer electrolyte fuel cell ii. empirical model development. *Journal of the Electrochemical Society*, 142(1):9–15, 1995.

[11] Ronald F Mann, John C Amphlett, Michael AI Hooper, Heidi M Jensen, Brant A Peppley, and Pierre R Roberge. Development and application of a generalised steady-state electrochemical model for a PEM fuel cell. *Journal of power sources*, 86(1):173–180, 2000.

[12] Chrysovalantou Ziogou, Spyros Voutetakis, Simira Papadopoulou, and Michael C Georgiadis. Modeling, simulation and experimental validation of a PEM fuel cell system. *Computers & Chemical Engineering*, 35(9):1886–1900, 2011.

[13] Jörg Wilhelm. *Modellierung, Identifikation und Regelung der kathodenseitigen Gaszufuhr einer PEM-Brennstoffzelle*. PhD thesis, 2005.

[14] Michael A Danzer, Jörg Wilhelm, Harald Aschemann, and Eberhard P Hofer. Model-based control of cathode pressure and oxygen excess ratio of a PEM fuel cell system. *Journal of Power Sources*, 176(2):515–522, 2008.

[15] Michael A Danzer, Simon J Wittmann, and Eberhard P Hofer. Prevention of fuel cell starvation by model predictive control of pressure, excess ratio, and current. *Journal of Power Sources*, 190(1):86–91, 2009.

[16] Jay T Pukrushpan, Anna G Stefanopoulou, and Huei Peng. *Control of fuel cell power systems: principles, modeling, analysis and feedback design*. Springer Science & Business Media, 2004.

[17] Jay T Pukrushpan, Anna G Stefanopoulou, and Huei Peng. Modeling and control for PEM fuel cell stack system. In *American Control Conference, 2002. Proceedings of the 2002*, volume 4, pages 3117–3122. IEEE, 2002.

[18] Amey Y Karnik, Jing Sun, Anna G Stefanopoulou, and Julia H Buckland. Humidity and pressure regulation in a PEM fuel cell using a gain-scheduled static feedback controller. *IEEE transactions on control systems technology*, 17(2):283–297, 2009.

[19] Imad Matraji, Salah Laghrouche, and Maxime Wack. Pressure control in a PEM fuel cell via second order sliding mode. *international journal of hydrogen energy*, 37(21):16104–16116, 2012.

[20] SC Olteanu, Abdel Aitouche, Mohamad Oueidat, and Adnan Jouni. PEM fuel cell modeling and simulation via the takagi-sugeno fuzzy model. In *Renewable Energies for Developing Countries (REDEC), 2012 International Conference on*, pages 1–7. IEEE, 2012.

[21] J Alejandro, Alicia Arce, and Carlos Bordons. Development and experimental validation of a PEM fuel cell dynamic model. *Journal of power sources*, 173(1):310–324, 2007.

[22] Cheng Bao, Minggao Ouyang, and Baolian Yi. Modeling and control of air stream and hydrogen flow with recirculation in a PEM fuel cell system—i. control-oriented modeling. *International journal of hydrogen energy*, 31(13):1879–1896, 2006.

[23] Paul Hendrik Rodatz. *Dynamics of the polymer electrolyte fuel cell: Experiments and model-based analysis*. PhD thesis, Swiss Federal Institute of Technology Zurich, 2003.

[24] Cheng Bao, Minggao Ouyang, and Baolian Yi. Modeling and control of air stream and hydrogen flow with recirculation in a PEM fuel cell system—ii. linear and adaptive nonlinear control. *International journal of hydrogen energy*, 31(13):1897–1913, 2006.

[25] MJ Khan and MT Iqbal. Modelling and analysis of electro-chemical, thermal, and reactant flow dynamics for a PEM fuel cell system. *Fuel cells*, 5(4):463–475, 2005.

[26] Jay T Pukrushpan, Anna G Stefanopoulou, and Huei Peng. Control of fuel cell breathing. *IEEE control systems*, 24(2):30–46, 2004.

[27] Amir M Niroumand, Oldooz Pooyanfar, Natalia Macauley, Jake DeVaal, and Farid Golnaraghi. In-situ diagnostic tools for hydrogen transfer leak characterization in PEM fuel cell stacks part i: R&d applications. *Journal of Power Sources*, 278:652–659, 2015.

[28] Weizhong Lü, Zhixiang Liu, Cheng Wang, Zongqiang Mao, and Milin Zhang. The effects of pinholes on proton exchange membrane fuel cell performance. *International Journal of Energy Research*, 35(1):24–30, 2011.

[29] Stefan Kreitmeier, Gabriel A Schuler, Alexander Wokaun, and Felix N Büchi. Investigation of membrane degradation in polymer electrolyte fuel cells using local gas permeation analysis. *Journal of Power Sources*, 212:139–147, 2012.

[30] MR Ashraf Khorasani, S Asghari, A Mokmeli, MH Shahsamandi, and B Faghih Imani. A diagnosis method for identification of the defected cell (s) in the PEM fuel cells. *International Journal of Hydrogen Energy*, 35(17):9269–9275, 2010.

[31] J Stumper, R Rahmani, and F Fuss. Open circuit voltage profiling as diagnostic tool during stack lifetime testing. *Journal of Power Sources*, 195(15):4928–4934, 2010.

[32] Ari Ingimundarson, Anna G Stefanopoulou, and Denise A McKay. Model-based detection of hydrogen leaks in a fuel cell stack. *IEEE Transactions on Control Systems Technology*, 16(5):1004–1012, 2008.

[33] Alireza Ebadighajari, Jake DeVaal, and Farid Golnaraghi. Optimal control of fuel overpressure in a polymer electrolyte membrane fuel cell with hydrogen transfer leak during load change. *Journal of Power Sources*, 340:247–257, 2017.

[34] Alireza Ebadighajari, Jake DeVaal, and Farid Golnaraghi. Multivariable control of hydrogen concentration and fuel over-pressure in a polymer electrolyte membrane fuel cell with anode re-circulation. In *American Control Conference (ACC), 2016*, pages 4428–4433. IEEE, 2016.

[35] Nobutaka Takahashi. Control of differential air and hydrogen pressures in fuel cell systems. *Journal of System Design and Dynamics*, 5(1):109–124, 2011.

[36] Young-Bae Kim. Improving dynamic performance of proton-exchange membrane fuel cell system using time delay control. *Journal of Power Sources*, 195(19):6329–6341, 2010.

[37] Jan Marian Maciejowski. *Predictive control: with constraints*. Pearson education, 2002.

[38] Alicia Arce, J Alejandro, Carlos Bordons, and Daniel R Ramirez. Real-time implementation of a constrained mpc for efficient airflow control in a PEM fuel cell. *IEEE Transactions on Industrial Electronics*, 57(6):1892–1905, 2010.

[39] A Arce, DR Ramirez, AJ Del Real, and C Bordons. Constrained explicit predictive control strategies for PEM fuel cell systems. In *Decision and Control, 2007 46th IEEE Conference on*, pages 6088–6093. IEEE, 2007.

[40] Alireza Ebadighajari, Hooman Homayouni, Jake DeVaal, and Farid Golnaraghi. Model predictive control of polymer electrolyte membrane fuel cell with dead-end anode and periodic purging. In *Control Applications (CCA), 2016 IEEE Conference on*, pages 1500–1505. IEEE, 2016.

[41] Julio Luna, Carlos Ocampo-Martinez, and Maria Serra. Nonlinear predictive control for the concentrations profile regulation under unknown reaction disturbances in a fuel cell anode gas channel. *Journal of Power Sources*, 282:129–139, 2015.

[42] Alireza Ebadighajari, Jake De Vaal, and Farid Golnaraghi. Optimal control of fuel over-pressure in a polymer electrolyte membrane fuel cell system during load change. In *American Control Conference (ACC), 2015*, pages 3236–3241. IEEE, 2015.

[43] Chrysovalantou Ziogou, Simira Papadopoulou, Michael C Georgiadis, and Spyros Voutetakis. On-line nonlinear model predictive control of a PEM fuel cell system. *Journal of Process Control*, 23(4):483–492, 2013.

[44] Keith Promislow, Jean St-Pierre, and Brian Wetton. A simple, analytic model of polymer electrolyte membrane fuel cell anode recirculation at operating power including nitrogen crossover. *Journal of Power Sources*, 196(23):10050–10056, 2011.

[45] Jixin Chen, Jason B Siegel, Anna G Stefanopoulou, and James R Waldecker. Optimization of purge cycle for dead-ended anode fuel cell operation. *international journal of hydrogen energy*, 38(12):5092–5105, 2013.

[46] Agus P Sasmito and Arun S Mujumdar. Performance evaluation of a polymer electrolyte fuel cell with a dead-end anode: A computational fluid dynamic study. *international journal of hydrogen energy*, 36(17):10917–10933, 2011.

[47] RK Ahluwalia and X Wang. Buildup of nitrogen in direct hydrogen polymer-electrolyte fuel cell stacks. *Journal of Power Sources*, 171(1):63–71, 2007.

[48] Kyung Don Baik and Min Soo Kim. Characterization of nitrogen gas crossover through the membrane in proton-exchange membrane fuel cells. *international journal of hydrogen energy*, 36(1):732–739, 2011.

[49] Abid Rabbani and Masoud Rokni. Effect of nitrogen crossover on purging strategy in PEM fuel cell systems. *Applied energy*, 111:1061–1070, 2013.

[50] Yong-Song Chen, Chih-Wei Yang, and Jiunn-Yih Lee. Implementation and evaluation for anode purging of a fuel cell based on nitrogen concentration. *Applied Energy*, 113:1519–1524, 2014.

[51] David Q Mayne, James B Rawlings, Christopher V Rao, and Pierre OM Scokaert. Constrained model predictive control: Stability and optimality. *Automatica*, 36(6):789–814, 2000.

[52] James B Rawlings and Kenneth R Muske. The stability of constrained receding horizon control. *Automatic Control, IEEE Transactions on*, 38(10):1512–1516, 1993.

[53] Brian J Kirby. *Micro-and nanoscale fluid mechanics: transport in microfluidic devices*. Cambridge University Press, 2010.

[54] R.A. Granger. *Fluid Mechanics*. Dover Books on Physics. Dover Publications, 2012.

[55] A.J. Smits and J.P. Dussauge. *Turbulent Shear Layers in Supersonic Flow*. Turbulent Shear Layers in Supersonic Flow. Springer, 2006.

[56] CR Wilke. A viscosity equation for gas mixtures. *The journal of chemical physics*, 18(4):517–519, 1950.

Appendix A

Reduction of Hydrogen Transfer by Constrained Control of Anode Hydrogen Recirculation in a Polymer Electrolyte Membrane Fuel Cell

Leakage of hydrogen due to the formation of pinholes endangers the membrane longevity in a polymer electrolyte membrane fuel cell (PEMFC). In this work, based upon a novel approach, mitigation of the hydrogen transfer leak rate is achieved via controlling the speed of the hydrogen recirculation blower (HRB) as well as fuel overpressure control. The problem is formulated as a constrained control problem. Considering the multivariable nature of the system, a model predictive controller is employed to meet with the objectives. Moreover, the control limitation in presence of large transfer leaks is discussed. In order to evaluate the controller performance, an experimental model of a Ballard 3kW test station equipped with an HRB is utilized, where the model is derived on the basis of pneumatic modeling technique with inclusion of the hydrogen transfer leak model. Simulation results demonstrate the controller ability for reducing the leak rate while handling the constraints, which leads to an improved durability for the membrane. Furthermore, it confirms the controller limitation.

The schematic of a PEMFC system in the AWR configuration is depicted in Figure A.1, using the piping and instrumentation (P&ID) diagram. According to this figure, the system is composed of three actuators on the anode side, namely, the pressure control valve, the purge valve, and the HRB. The pressure control valve regulates the fuel overpressure while the purge valve is responsible for the anode H_2 concentration control to prevent performance deterioration. The purge valve can either be controlled dynamically [34], or periodically [40]. The reason behind purging is to reestablish pure hydrogen flow in the anode. Due to nitrogen and water crossovers, the anode H_2 concentration drops and consequently, the PEMFC performance is impaired. Therefore, fuel purging temporarily replenishes the anode with pure hydrogen flow.

In this work, fuel overpressure is dynamically controlled. However, purging is carried out periodically where a load-based purging strategy is used. This stems from the fact that N_2 and water crossovers vary depending on the current, and this directly affects the rate of performance drop which has to be compensated by purging.

Furthermore, the HRB speed is controlled to reduce the hydrogen leakage due to pinholes, which are typical sources of membrane degradation. Controlling the fuel overpressure in the presence of membrane pinholes impedes oxygen leakage to the anode. This leakage accelerates the cell degradation due to fuel starvation. Therefore, fuel overpressure deals with the effects of transfer leaks indirectly. The aim here is to directly impact transfer leaks via constrained control of the HRB.

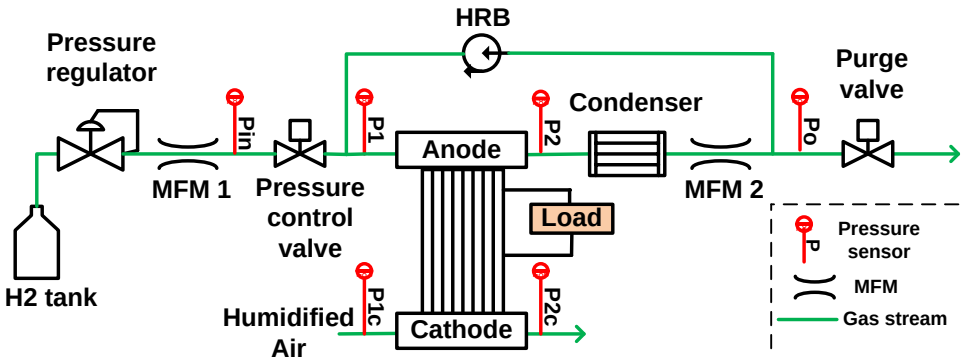

Figure A.1: The schematic of the 3kW PEMFC test station with anode recirculation

A.1 Modeling of the PEMFC with anode recirculation

The AWR configuration in Figure A.1 consists of different components including, a pressure regulator, a pressure control valve, a PEMFC anode, a condenser, a purge valve, and an HRB. Moreover, the system is comprised of pressure sensors and mass flow meters (MFM). The air side dynamics is not included in this work, except for monitoring the cathode inlet and outlet pressures of the PEMFC stack.

Employing the pneumatic modeling approach in [14], the AWR structure is described by pneumatic variables such as pneumatic resistors and capacitors. These resistors reflect friction forces in the gas flow channels while capacitors indicate the storage potential of the components. Considering a laminar flow regime [34], all pneumatic variables are also laminar where the pressure drop (ΔP) across each pneumatic resistor (R_L) is proportional to its flow rate (Q):

$$\Delta P = R_L Q \tag{A.1}$$

In analogy to electrical systems, Figure A.2 illustrates the equivalent circuit of the AWR configuration with the use of pneumatic variables. The inlet pressure regulator is described via a voltage source as it provides a fixed pressure. Pressure variables in Figure A.2 are pointing to the same nodes as in Figure A.1. Both the pressure control valve and the purge

valve are modeled as variable resistors since they are actuators. However, only the pressure control valve is among the control inputs, and the purge valve only operates in the ON-OFF mode periodically according to the load demand. H_2 consumption and N_2 crossover are represented via current sources and placed at the inlet and outlet of the PEMFC stack, respectively [40]. Furthermore, the H_2 transfer leak is also described by a current source and is placed at the outlet side of the stack to reflect the total leakage. Finally, the dynamic behavior of the HRB is captured by a controllable current source as changes in the HRB speed affect the pumped flow.

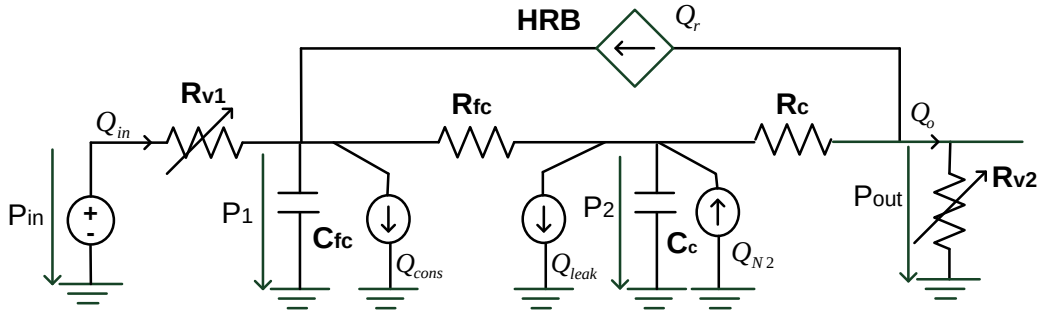

Figure A.2: The equivalent electrical circuit of the PEMFC test station with anode recirculation using the pneumatic variables

A.1.1 State-Space Model

According to Figure A.2, the following differential equations are valid:

$$C_{fc}\dot{P}_1 = Q_{in} - Q_c + Q_r - \frac{P_1 - P_2}{R_{fc}} \tag{A.2}$$

$$C_c\dot{P}_2 = \frac{P_1 - P_2}{R_{fc}} - \frac{P_2 - P_{out}}{R_c} + Q_{N_2} - Q_{leak} \tag{A.3}$$

$$\frac{P_{in} - P_1}{R_{v_1}} = Q_{in} \tag{A.4}$$

$$\frac{P_2 - P_{out}}{R_c} = Q_r + Q_o \tag{A.5}$$

To select the control input variables, a nonlinear transformation is used such that a linear state-space model is obtained. As described by (A.4), R_{v_1} at the denominator introduces a nonlinear term. Therefore, Q_{in} is chosen as the control input. The recirculation flow, Q_r, is also a control input:

$$Q_{in} = \frac{P_{in} - P_1}{R_{v_1}} = u_1 \tag{A.6}$$

$$Q_r = u_2 \tag{A.7}$$

The actual control inputs are the valve input voltage (V_i), and the HRB control voltage (V_{hrb}). The purge valve operates in the ON-OFF mode which causes the output flow (Q_o) to vary significantly. This is considered as a disturbance in controller design.

Based on the work in [27], hydrogen transfer leak rate is a function of leak size and fuel overpressure. Assuming a fixed leak size, the following model represents H_2 transfer leak rate:

$$Q_{leak} = k(l)(P_2 - P_{2c}) \tag{A.8}$$

where P_2 is the stack anode outlet pressure and P_{2c} is the stack cathode outlet pressure. k is a coefficient determined by the leak size l. This will be clarified in section A.1.3. Replacing equations (A.4-A.8) into (A.1) and (A.2), the state-space model of the system is given as follows:

$$\begin{cases} C_{fc}\dfrac{dx_1}{dt} = \dfrac{-1}{R_{fc}}x_1 + \dfrac{1}{R_{fc}}x_2 + u_1 + u_2 - w_1 \\ C_c\dfrac{dx_2}{dt} = \dfrac{1}{R_{fc}}x_1 - (\dfrac{1}{R_{fc}} + k)x_2 - u_2 + kw_2 + w_3 - w_4 \end{cases} \tag{A.9}$$

where the state vector $x(t)$, the control input vector $u(t)$, and the disturbance vector are expressed in (A.10).

The anode pressure at the inlet and outlet sides of the stack are chosen as state variables. As already mentioned, the anode input flow rate as well as the recirculation flow rate are selected as control inputs. The hydrogen consumption flow rate, the stack cathode inlet pressure, the nitrogen crossover flow rate, and the output flow are included in the disturbance vector.

$$\begin{cases} x(t) = \begin{bmatrix} x_1(t) \\ x_2(t) \end{bmatrix} = \begin{bmatrix} P_1(t) \\ P_2(t) \end{bmatrix} \\ u(t) = \begin{bmatrix} u_1(t) \\ u_2(t) \end{bmatrix} = \begin{bmatrix} Q_{in}(t) \\ Q_r(t) \end{bmatrix} \\ w(t) = \begin{bmatrix} w_1(t) \\ w_2(t) \\ w_3(t) \\ w_4(t) \end{bmatrix} = \begin{bmatrix} Q_c(t) \\ P_{2c}(t) \\ Q_{N_2}(t) \\ Q_o(t) \end{bmatrix} \end{cases} \tag{A.10}$$

The output variables are decided according to the control objectives as explained in section A.2.1:

$$\begin{cases} y_1(t) = x_1(t) \\ y_2(t) = kx_2(t) \end{cases} \tag{A.11}$$

Using the matrix notation, the state-space model is expressed in the following:

$$\begin{cases} \dot{x} = Ax + \overbrace{\left[\begin{array}{c:c} B_1 & B_2 \end{array}\right]}^{B} \left[\begin{array}{c} u \\ \hdashline w \end{array}\right] \\ y = Cx \end{cases} \tag{A.12}$$

$$\begin{cases} A = \begin{bmatrix} \dfrac{-1}{R_{fc}C_{fc}} & \dfrac{1}{R_{fc}C_{fc}} \\ \dfrac{1}{R_{fc}C_c} & \dfrac{-1-kR_{fc}}{R_{fc}C_c} \end{bmatrix} \\ B = \left[\begin{array}{cc:c:ccc} \dfrac{1}{C_{fc}} & \dfrac{1}{C_{fc}} & \dfrac{-1}{C_{fc}} & 0 & 0 & 0 \\ 0 & \dfrac{-1}{C_c} & 0 & \dfrac{k}{C_c} & \dfrac{1}{C_c} & \dfrac{-1}{C_c} \end{array}\right] \\ C = \begin{bmatrix} 1 & 0 \\ 0 & k \end{bmatrix} \end{cases} \tag{A.13}$$

The state-space model in (A.12-A.13) comprises of system parameters that should be identified. The parameter identification was discussed in [33] and is summarized in Table A.1.

Table A.1: The model parameters on the anode side

Parameter	Value	Unit
C_{fc}	6.8×10^{-9}	ms^2
C_c	9.8×10^{-9}	ms^2
R_{fc}	2.3×10^{8}	$(ms)^{-1}$
R_c	0.5×10^{8}	$(ms)^{-1}$

A.1.2 Actuator modeling

The control input vector in (A.10) consists of the anode input flow rate (Q_{in}) and the recirculation flow rate (Q_r). However, the actual actuator commands include the valve input voltage and the HRB input voltage.

The dynamic behavior of the pressure control valve is described via the nonlinear function f, which relates the flow rate through the valve (Q_v) to the pressure drop across the valve (ΔP_v), and the input voltage (V_i):

$$Q_v = f(\Delta P_v, V_i) \tag{A.14}$$

where according to Figure A.2, Q_v and ΔP_v are as follows:

$$Q_v = Q_{in} \tag{A.15}$$

$$\Delta P_v = P_{in} - P_1 \tag{A.16}$$

Once the controller determines $u_1(Q_{in})$, using ΔP_v and f, the input voltage can be derived. Details of the valve model are provided in [33].

The hydrogen recirculation blower is controlled by an input voltage that is applied to a Brushless Direct Current (BLDC) motor. To accurately model the HRB, knowledge about the BLDC motor is required. A more practical approach is to obtain a model reflecting the HRB's role in the system in a real scenario. This results in determining the recirculated flow by the HRB for various stack anode inlet pressures and input voltages as stated by the function g:

$$Q_{hrb} = g(P_{hrb}, V_{hrb}) \tag{A.17}$$

where based on Figure A.2, this can be written as follows:

$$Q_r = g(P_1, V_{hrb}) \tag{A.18}$$

As previously mentioned, N_2 crossover decreases the H_2 concentration on the anode side. Depending on the hydrogen gas concentration (x_h), Q_r can be different for a same inlet pressure and input voltage. Therefore, (A.18) can be extended to include various H_2 concentrations:

$$Q_r = g(P_1, V_{hrb}, x_h) \tag{A.19}$$

Therefore, the model in (A.19) is used as the HRB model without having to include the BLDC motor characterization. The HRB dynamic behavior is shown in Figure A.3 for various stack inlet pressures and input voltages. Since in this work, the purge valve operates periodically, the H_2 concentration remains close to 100%. Therefore, in Figure A.3 only the pure hydrogen case ($x_h = 1$) is illustrated.

A.1.3 Hydrogen transfer leak characterization

The model in (A.8) states that the H_2 leak rate is proportional to the outlet pressure difference between the stack anode and cathode, via the parameter k. Depending on the leak size, k can be different. Figure A.4 illustrates the leak rate as a function of ovepressure for various leak sizes using the ex-situ measurement setup for the Ballard bus-type membrane [27]. This leak characterization is used in the control design. A more accurate way of placing Q_{leak} in the model is to include it on both the inlet and outlet sides of the stack, but it has been included in the outlet in this work, because this is where transfer of hydrogen can have the most significant impact on the downstream cathode hydrogen emission concentrations.

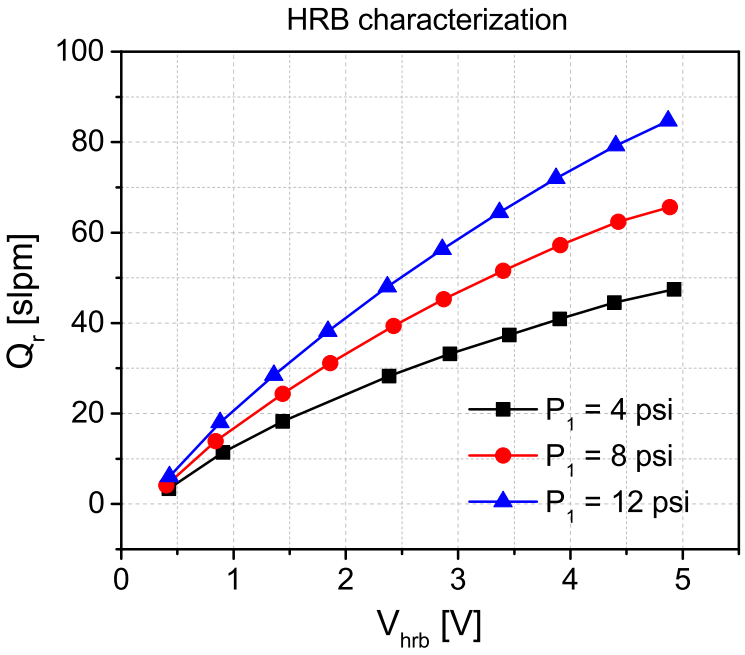

Figure A.3: The HRB characterization for various anode stack inlet pressures

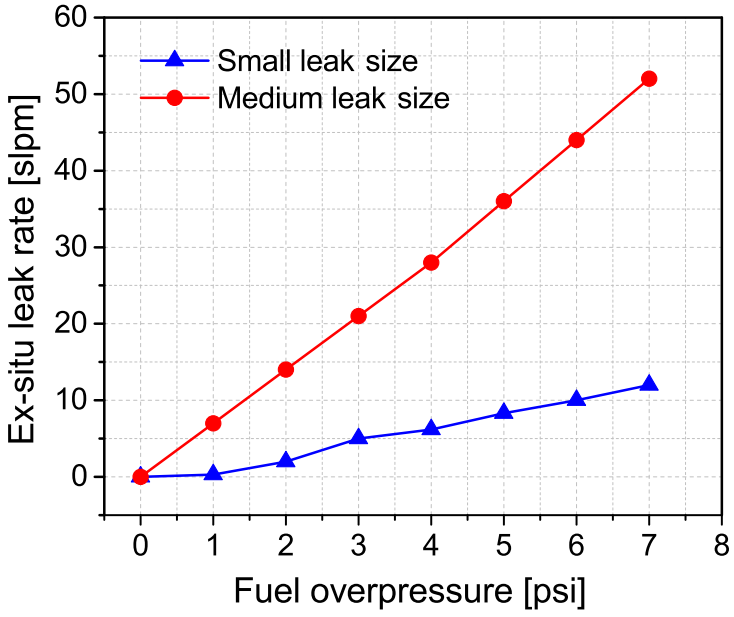

Figure A.4: The ex-situ leak measurement as a function of fuel overpressure

A.2 Controller design

Reducing the hydrogen transfer leak rate and controlling the fuel overpressure are the objectives of control design. Various disturbances are affecting the system as are introduced in (A.10). There exist constraints on both the actuator commands and the output variables. Therefore, constrained formulation of the control problem is used and the objectives are tackled by the MPC approach. The MPC ability to handle multivariable constrained control problem as well as providing an optimal control input, make MPC a suitable choice for this work. Application of the MPC method for industrial control tasks has largely increased during the recent years [37]. Based on an internal model of the system, MPC is able to predict the system output, $\hat{y}$, over the prediction horizon H_p. Moreover, it determines a control input, $\hat{u}$, over the control horizon, H_u, that minimizes the output error as well as the changes in control effort. This is acheived by minimzing the cost function J in (A.20) [37].

$$J(k) = \|\hat{\mathcal{Y}}(k) - \mathcal{T}(k)\|_Q^2 + \|\Delta\hat{\mathcal{U}}(k)\|_R^2 \tag{A.20}$$

where Q and R are weighting matrices for the output error and the control effort, respectively. $\mathcal{Y}(k)$, $\mathcal{T}(k)$, and $\Delta\mathcal{U}(k)$ are the vectors of appropriate sizes. In the case of having a precise model, the actual and predicted values are equivalent, i.e., $\hat{y} = y$ and $\hat{u} = u$.

Figure A.5 depicts the control problem architecture. Considering this, the control input u_1 together with ΔP are used to calculate the actuator signal (V_i) to the valve via f^{-1}. Similarly, the control input u_2 and P_1 are utilized to derive the HRB voltage (V_{hrb}) via g^{-1}. Model mismatch is reflected by the error inputs e_1 and e_2. Assuming a precise actuator model is available, $f.f^{-1} = g.g^{-1} = 1$. Since Figure A.5 accounts for controller implementation, it possesses a major advantage.

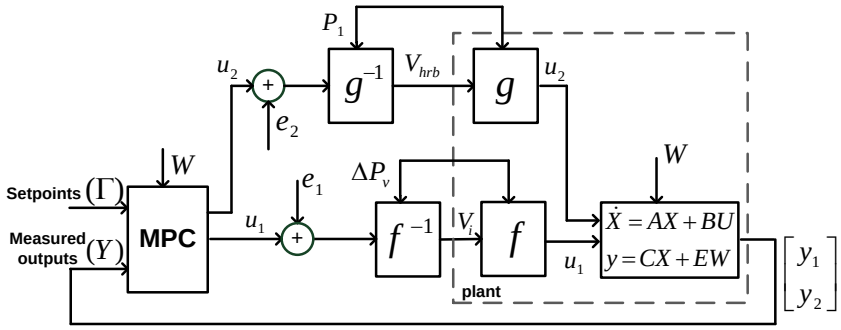

Figure A.5: The architecture of the control problem

A.2.1 Control problem formulation

To meet the objectives of the control problem, output setpoints are defined as follows:

$$y_{1d}(t) = P_{1c} + \text{OVP} \tag{A.21}$$

$$y_{2d}(t) = kP_{2c} + M = kw_2(t) + M \tag{A.22}$$

where OVP is the desired fuel overpressure. $y_{2d}(t)$ is chosen to minimize the leak rate described in (A.8), where M is a leak reduction level depending on the leak size l.

In addition, there exists a number of constraints on both the actuators and the outputs variables. Using the actuator model, actuator limitation can be described in terms of Q_{in} and Q_r. Formulation of the problem constraints are as follows:

$$x(k+i+1|k) = A_d x(k+i|k) + B_d u(k+i|k) \tag{A.23}$$

$$u_{1_{min}} \leq u_1(k+i|k) \leq u_{1_{max}} \tag{A.24}$$

$$\Delta u_{1_{min}} \leq \Delta u_1(k+i|k) \leq \Delta u_{1_{max}} \tag{A.25}$$

$$u_{2_{min}} \leq u(k+i|k) \leq u_{2_{max}} \tag{A.26}$$

$$y_{1d} - \gamma_{min} - \epsilon_1 \leq y_1(k+i|k) \leq y_{1d} + \gamma_{max} + \epsilon_1 \tag{A.27}$$

$$y_{2d} - \epsilon_2 \leq y_2(k+i|k) \leq y_{2d} + \beta + \epsilon_2 \tag{A.28}$$

where $i = H_w, \cdots, H_p$ with H_w as the starting point for penalization. A_d and B_d are the discretized form of A and B, respectively. $u_{1_{min}}$ and $u_{1_{max}}$ are the valve active range in terms of Q_{in} that is between 0 to 10^{-4}kg/s. $\Delta u_{1_{min}}$ and $\Delta u_{1_{max}}$ are the limits on the slew rate of the valve input, which in terms of ΔQ_{in} are $\pm 10^{-4}$kg/s^2. Moreover, γ_{min} and γ_{max} are the maximum allowed overpressure deviations from the desired value which are chosen at $\pm$5000Pa. Finally, $u_{2_{min}}$ and $u_{2_{max}}$ are the recirculation flow limits that are set at 0 and 5×10^{-4}kg/s, respectively. Furthermore, ϵ_1 and ϵ_2 are the slack variables to relax the output constraints [37].

Therefore, the convex cost function in (A.20), the linear equality constraint in (A.23), and the convex inequality constraints (A.24-A.28) form a convex problem where any local optimum is also a global optimum. Solving this optimization function may encounter feasibility issues which can be resolved by softening the constraints (using the slack variables). However, actuator constraints can not be violated.

A.3 Simulation results

Using the experimentally validated model of a Ballard 9-cell liquid-cooled PEMFC stack [33], the controller performance is evaluated in presence of a variable load, dynamic current-based purging, and hydrogen transfer leaks. In addition, the simulation uses an experimental data set for controller evaluation. Figure A.6(a) shows the simulation scenario where the load variation and purging signals are illustrated. As mentioned, the purging period (T_p) is a function of current where for 80A, $T_p = 30s$, while for 20A, $T_p = 60s$ with the duty cycle of the valve at 7% and 3% of the period for each case, respectively.

The load variation encompasses both rising and falling edges of load demand. During the acceleration at around 250s, both fuel overpressure and hydrogen leak rate follow the desired trajectories and stay within the output limits as shown in Figure A.6(b)&(c), respectively. y_{1d} is chosen at 5000Pa while y_{2d} is set at kP_{2c} with $M = 0$. Therefore, the aim is to reduce the leak rate to zero. Control inputs Q_{in} and Q_r are shown in Figure A.7(a).

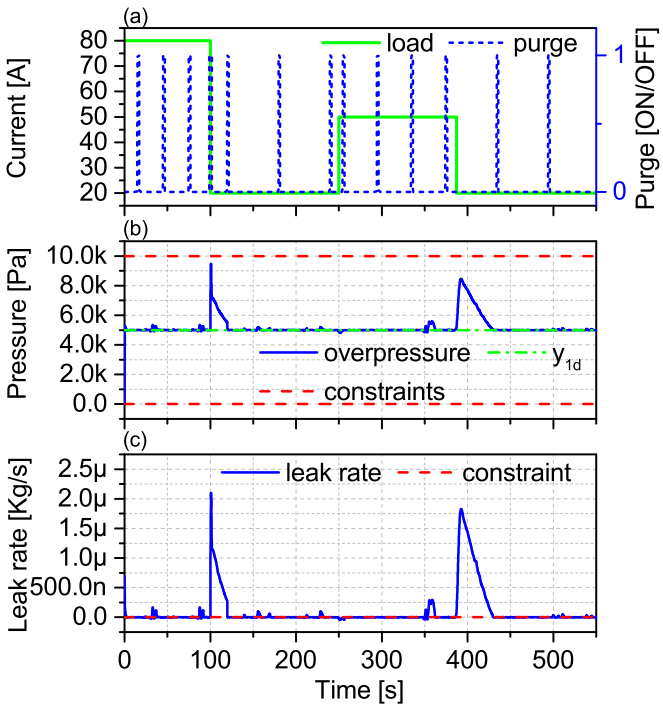

Figure A.6: (a) The simulation scenario including the load change and the purging action, (b) The fuel overpressure tracking and the output constraints, (c) The hydrogen leak rate and the lower output limit

However, during the load deceleration at 100s and 387s, a considerable output deviation from the setpoints can be observed. A more severe load decrease at 100s causes a larger deviation compared to 387s. According to Figure A.6(b), fuel overpressure remains within the constraint during the transients caused by the load decrease at 100s and 387s, and tracks y_{1d} afterwards. Furthermore, the H_2 leak rate follows y_{2d}. Respecting the lower constraint on y_2 is crucial, i.e., $y_2 < y_{2d}$ results in $Q_{leak} < 0$ which directs the air flow into the anode, causing fuel starvation. In Figure A.6(c) the leak rate stays above zero which confirms that the lower constraint on output y_2 is met.

During the load decrease at 100s and 387s, the control input Q_{in} reaches the lower limit as shown in Figure A.7(a). Despite a larger load drop at 100s, because of simultaneous purging at 100s, Q_{in} stays at the lower limit for a shorter time compared to 387s (when no purging occurs). The explanation behind this is that when the purge valve is closed, the only way to reduce the pressure is to discharge the flow via consumption or through the pinholes. The latter is among the control objectives which should be reduced. Hence, the former is the way for pressure reduction. By opening the purge valve, the pressure drops quicker since an alternative route for gas flow is opened.

Figure A.7(b) illustrates the controller limitation. In Figure A.6 and Figure A.7(a), k resembles a small/medium leak range. However, when the leak size becomes large, the leakage of hydrogen during the transient is higher. Therefore, for larger leak sizes the controller is no longer capable of preventing a higher hydrogen loss. This is also a practical

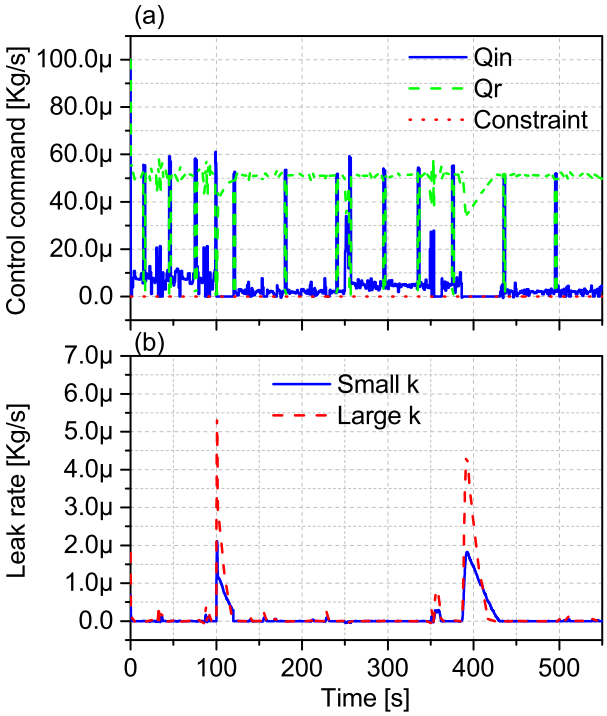

Figure A.7: (a) The controller inputs Q_{in} and Q_r, (b) The controller limitation for large H_2 transfer leaks

limitation, where the ability to minimize fuel loss is no longer effective when the leaks become large, and the defected cell should then be replaced.

The model predictive control toolbox in MATLAB is used for simulation with the sampling time of the controller at 0.1s to cope with the fastest plant dynamic.

A.4 Conclusions

Employing a model-based constrained control approach, mitigation of small to medium hydrogen transfer leakage in PEM fuel cells with AWR configuration was presented. Problem objectives are achieved by controlling the HRB speed and regulating the pressure control valve. A load-based purging strategy was utilized where nitrogen crossover was also included in the model. The system was described via an experimentally validated pneumatic model of a Ballard 9-cell PEMFC. Actuator modeling was also discussed and included in the structure of the control problem. Using experimental data, the controller performance was evaluated during the load variation where both the tracking performance and the constraint handling were demonstrated. Finally, the controller limitation was explained which revealed a higher hydrogen loss during transients for larger leak sizes. Future works, include a more precise model of the hydrogen transfer leak as well as the implementation of the proposed method in a product environment.